Ultrafast dynamics of photoinduced charge separation in cyanine- and polymer-based organic photovoltaic systems

THÈSE N° 6627 (2015)

PRÉSENTÉE LE 19 JUIN 2015
À LA FACULTÉ DES SCIENCES DE BASE
GROUPE DE DYNAMIQUE PHOTOCHIMIQUE
PROGRAMME DOCTORAL EN PHOTONIQUE

ÉCOLE POLYTECHNIQUE FÉDÉRALE DE LAUSANNE

POUR L'OBTENTION DU GRADE DE DOCTEUR ÈS SCIENCES

PAR

Jelissa RISSE (née DE JONGHE)

acceptée sur proposition du jury:

Prof. O. Martin, président du jury
Prof. J.-E. Moser, directeur de thèse
Prof. F. Nüesch, rapporteur
Prof. C. Silva, rapporteur
Prof. E. Vauthey, rapporteur

EPFL

ÉCOLE POLYTECHNIQUE
FÉDÉRALE DE LAUSANNE

Suisse
2015

Abstract

Organic photovoltaics (OPV) have the potential to provide low-cost solar-to-electricity converting devices. Improving such devices requires a deeper understanding of the ultrafast photoinduced processes occurring after light absorption. We have performed femtosecond (fs) transient absorption spectroscopy, as well as time-resolved electroabsorption (Stark effect) on model OPV systems to follow electron and hole transfer dynamics, as well as charge carrier motion in the active layer to the electrodes.

Solid-state cyanine borate (Cy3-B) films undergo intra-ion pair reductive quenching on the picosecond (ps) timescale. We have found that when intermixing Cy3-B with a fullerene acceptor (PCBM), photoexcitation leads to the appearance of oxidized Cy3 in less than 70 fs. We correlated the rate and yield of Cy3 oxidation to the PCBM loading. We then investigated a cyanine Cy3-P in a bilayer geometry with fullerene C_{60}. In this case, ultrafast electron transfer in less than 100 fs is followed by slower dissociation of interfacial charge transfer states in the presence of an electric field. A photoinduced Stark effect observed in neat C_{60} enabled to identify an initially delocalized excited state, which localizes in 360 fs. Lastly, we analyzed how microstructural changes in polymer pBTTT:PCBM blends impact free charge carrier formation and motion. We identified that the intermixed phase efficiently produces charge carriers within 100 fs, and that pure fullerene and pBTTT domains attract the charge carriers separating them further apart. This is ascribed to an energy cascade toward the neat domains.

This thesis reveals ultrafast charge transfer at donor-acceptor interfaces in such OPV systems by means of fs transient absorption spectroscopy. Results emphasize that a second step is needed for charge separation in order to successfully compete with charge pair recombination in these systems. An

electric field applied can act as a driving force to dissociate interfacial charge transfer states. Pure donor or acceptor domains attract holes or electrons, respectively, and reduce geminate charge recombination in blends. These second steps in charge separation were derived from photoinduced electroabsorption dynamics in transient absorption measurements, as well as time-resolved electroabsorption based on the Stark effect.

Résumé

Les systèmes photovoltaïques basés sur des semi-conducteurs organiques ont le potentiel de produire de l'électricité à bas coût. Afin d'améliorer cette technologie, l'étude des processus photoinduits ultrarapides après absorption de lumière est fondamentale. Nous avons entrepris des mesures d'absorption transitoire femtoseconde (fs) ainsi que d'éléctroabsorption résolue en temps (effet Stark) sur des systèmes photovoltaïques organiques modèles afin d'observer la dynamique du transfert d'électron et de trou, ainsi que le déplacement des charges au travers de la couche active jusqu'à l'électrode.

Dans les couches solides de cyanine borate (Cy3-B) nous observons un quenching réductif dans la paire d'ions en quelques picosecondes (ps). En introduisant un accepteur d'électron, le fullerene PCBM, nous avons pu observer l'oxydation de la cyanine en moins de 70 fs. Nous avons corrélé le taux et le rendement d'oxydation à la concentration de PCBM. Nous nous sommes ensuite intéressés à la bicouche de cyanine Cy3-P avec le fullerene C_{60}. Nous avons observé un transfert d'électron ultrarapide (<100 fs) suivi d'une dissociation lente des états de transferts de charge à l'interface en la présence d'un champ électrique. Un effet Stark photoinduit dans une couche de C_{60} pur a permis de déterminer un état excité initialement délocalisé qui se localise en 360 ps. Finalement, nous avons analysé comment des changements de microstructure dans des mélanges de polymère pBTTT :PCBM affectent la formation de charges libres et leur déplacement. Nous avons identifié que les domaines intimement mélangés produisent des charges en moins de 100 fs, et que des domaines purs de fullerene et de pBTTT attirent et séparent les paires de charges géminées. Nous attribuons cet effet à une cascade énergétique vers les domaines purs.

Ce travail de thèse révèle des transferts de charge ultrarapide à l'interface de donneurs et accepteurs dans de tels systèmes grâce à des mesures d'absorption

transitoire femtoseconde. Nous avons également identifié qu'une deuxième étape était nécessaire à la séparation de charges afin de rivaliser avec leur recombinaison. Une force motrice pour dissocier des états de transfert de charge à l'interface est par exemple un champ électrique appliqué. Des domaines purs de donneur ou d'accepteur d'électron dans des mélanges (blends) attirent les trous et électrons, respectivement. Ils réduisent également la recombinaison géminale de paires électron-trou. Ces différentes forces motrices nécessaires à la dissociation de charges ont été révélées en suivant l'éléctroabsorption photoinduite dans les mesures d'absorption transitoire, ainsi que par des mesures d'éléctroabsorption résolue en temps (effet Stark).

Mots-clés: Semi-conducteur organique, cyanine, fullerene, pBTTT, transfert de charge, absorption transitoire, electroabsorption, effet Stark.

Aux rires aux éclats
A l'innocence déjà
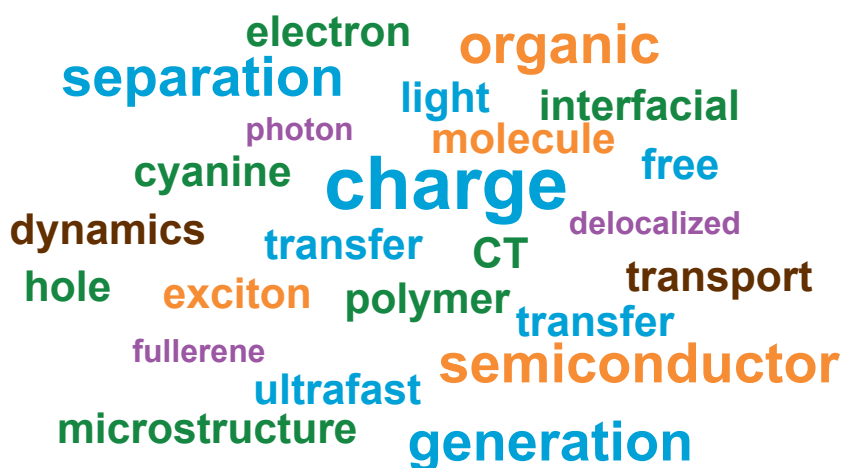A l'esprit malicieux
Au chemin précieux

Table des matières

Chapter 1
Introduction to ultrafast photoinduced dynamics in organic semiconductors

Inspired by Text is Beautiful

1.1 Introduction

In 2015, no one can ignore the dramatic impacts on the environment and more globally life on earth caused by the use of non-renewable energy sources. Depletion of fossil fuels, natural gas and coal by industrial and developing countries is another evidence of the need for alternative renewable energy sources, which have luckily grown in interest and applicability over the past years. From a more political point of view, Switzerland chose to abolish nuclear energy by 2034 after the earthquake and subsequent nuclear incident at Fukushima, Japan in 2011. In Switzerland in 2013, 40 % of the energy consumption was provided by nuclear reactors. This non-renewable energy source is complemented by hydroelectricity to provide the 60 TWh needed. The latter is, however, almost at its full capacity, therefore solutions are required toward other renewable energies. One of them is photovoltaics, and has by far the largest potential to produce electricity. As a matter of fact, production costs can be kept low and incoming energy does not require extreme geographic location.[1] Integrating photovoltaic (PV) panels in existing urban infrastructure is a major advantage of this technology over other renewable energies such as wind and hydroelectricity, which often have side effects on natural ecosystems.[2]

The intriguing label "photovoltaics" actually covers intense activity from a very broad scientific community. The variety of photovoltaic devices offers multiple applications, suitable to large areas as well as semi-transparent windows or even flexible coatings on backpacks. While the former is based on inorganic materials such as silicon, the latter are designed from dyes and organic semiconductor materials, which are conjugated dye molecules and polymers. Those photovoltaic devices can again be split into two categories: either fully organic (OPV), or hybrid in dye-sensitized solar cells (DSSC).

A large panel of organic optoelectronic materials have been designed for diverse functions: OPV, organic light emitting diodes (OLED), and organic field effect transistors (OFET). In addition to their multiple applications, they are low-cost

solutions and offer better recycling possibilities than the inorganic devices. As a comparison, very little material is needed for OPV devices, about $1g/m^2$, whereas silicon panels require in the order of $200g/m^2$. Fabrication procedures such as inkjet printing, and abundance of raw material, further makes OPV devices competitive. However, efficiency and stability issues still have room for improvement. State of the art organic photovoltaic devices have reached beyond 11 % efficiency but they still lag silicon PV pushing fast forward with 25 % efficiency.[3] Understanding the operating principles in organic photovoltaic devices is crucial for their optimization. Investigating the processes by which light is converted into electricity is challenging. Our aim is to identify and understand these steps in order to provide guidance for material engineering. Let us start from the beginning: what is an OPV device made from?

1.2 Photochemistry basics

The following section is based on several reviews and books, a PhD thesis as well as two courses: *Photochemistry* from Prof. J.-E. Moser and *Organic semiconductors* from Prof. F. Nüesch.[1,4-10]

1.2.1 What characterizes an organic semiconductor?

Organic materials are by definition metal-free. Carbon, a widely abundant material, is the basis of organic semiconductors. To understand where the electronic conducting properties come from, we need to look at the electronic scale of carbon atoms and see what makes electrons mobile.

Carbon molecular orbitals can hybridize to three sp^2 and one p_z orbital. When bringing two carbon atoms close together, sp^2 orbitals of different carbon atoms will overlap and create σ and σ* molecular orbitals. These create the structure of the C-C bond, therefore the backbone of the molecule. Now the p_z orbitals will also overlap in another plane, creating π and π* molecular orbitals. The energy

gap between π and π* orbitals is the smallest available in the system, which is relevant for photochemistry. Indeed, the π orbital has two electrons and is the highest occupied molecular orbital (HOMO). π* does not contain electrons in the "relaxed" state, thus corresponding to the lowest unoccupied molecular orbital (LUMO). π electrons are responsible for a double bond between neighboring C atoms. They are delocalized, as they are shared on both carbon atoms. The length of the double C=C bond is reduced compared to the single C-C bond. Alternation of single and double bonds when adding up several carbons leads to a delocalized system, which is at the origin of the semiconducting properties.[6] We can relate the HOMO level to the valence band of a semiconductor, and the LUMO level to the conduction band. The HOMO-LUMO energy difference is called band gap, and the conjugation length determines the band gap energy and thus the photon absorption.

Organic semiconductors have a rather narrow absorption range compared to inorganic semiconductors. This is compensated by larger extinction coefficients, enabling the use of thin films on the nanometer size.

The material can be molecular, or a repetition of the monomeric building-block: a polymer. A. Heeger, A. McDiarmid, H. Shirakawa (Nobel Prize in Chemistry, 2000) and coworkers discovered that doped polymers with a fully conjugated backbone could separate and transport electrons and holes, with relatively high carrier mobility.[11] Since then, interest has grown for the potentially cheap organic semiconductors to replace comparably more expensive silicon solar photovoltaics. We will now overview the steps from photon absorption to charge formation in an organic semiconductor.

1.2.2 Transitions in organic semiconductors

Upon light absorption in organic semiconductors, deactivation transitions occur on a range of timescales to finally recover the ground state, as summarized in the Jablonski diagram in Figure 1.1. When a photon triggers the HOMO-

LUMO transition, an electron is placed in a higher electronic state for example S_1: an excited state. This upper transition only occurs if it is allowed, and if the photon energy is larger or equal to the band gap. The Franck-Condon principle dictates the process of light absorption and states that the transition is vertical. A hot excited state can be generated if the photon energy is larger than the band gap, resulting in a high vibrational excited state. Vibrational relaxation (VR) to the lowest (relaxed) excited state occurs on a picosecond timescale (ps). Following Kasha's rule, radiative transition back to the ground state occurs mostly from the lowest excited state with same multiplicity. Fluorescence (radiative transition) occurs typically on a nanosecond timescale (ns). Non-radiative transitions such as internal conversion (IC) also lead to deactivation to the ground state. Intersystem crossing (ISC) by spin flip to the triplet state occurs on delayed time scales, and radiative decay from the triplet state, called
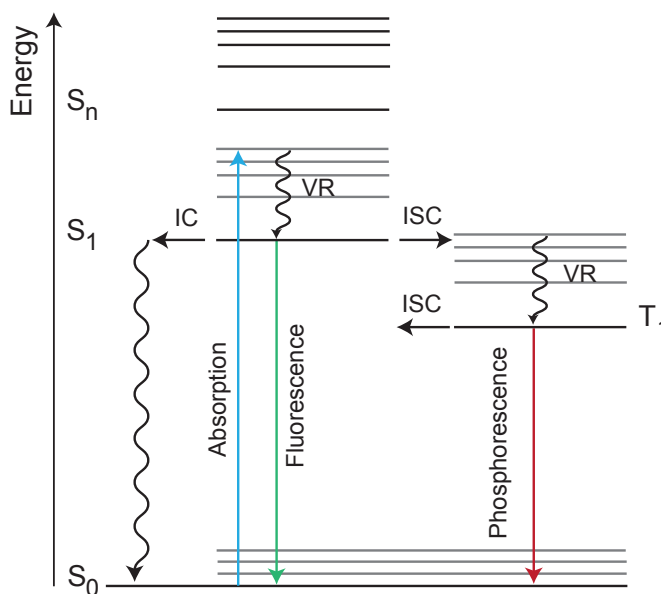
Figure 1.1 Jablonski diagram

Light absorption (within 10^{-16} s) creates an excited state. Vibrational relaxation to the lowest excited state occurs for high vibrationnally excited state by release of excess energy (VR, 10^{-12} s). Following Kasha's rule, only the lowest excited state will undergo radiative decay via fluorescence (10^{-9} s). Intersystem crossing (ISC) from singlet to triplet is a spin flip process (10^{-9} - 10^{-6} s). Radiative decay from the triplet state is called phosphorescence (10^{-4} - 10^{2} s). Internal conversion (IC) to the ground state is a non-radiative deactivation pathway. S_n depicts higher electronic states.

phosphorescence, typically spans over slower timescales.

1.2.3 Photoinduced electron transfer

Photovoltaic semiconductors must achieve two roles: light harvesting and charge transport. In opposition to free charge carrier generation resulting from light absorption in inorganic semiconductors, light absorption in organic semiconductors produces a neutral excited state. This is due to the small dielectric constant typical of organic semiconductors ($\varepsilon \approx$ 3-4), resulting in coulombic attraction between the electron and the hole (empty electronic state in the HOMO/valence band) due to the lack of charge screening. This neutral excited state, called exciton, located on one molecule will undergo radiative or non-radiative decay as discussed in the previous section. To favor a proper charge separation and counteract excited state (exciton) binding energy, a donor/acceptor (D/A) interface was first introduced by Tang in 1986.[12] The different position of HOMO and LUMO energy levels of those two materials now gives a driving force for the electron in the excited state to transfer to a lower LUMO level. Such a heterojunction is illustrated in Figure 1.2. A prerequisite for this process is that exciton diffusion to the interface takes place before it decays back to the ground state. Random exciton diffusion through the active layer is usually described by Förster energy transfer that typically lowers the excited state energy. Trap sites generated by defects or aggregates will lead to deactivation to the ground state. Too thick layers also prevent energy transfer to the D/A interface due to short excited state lifetime. Depending on the light absorption site, electron injection into the acceptor can occur from both hot and cold (relaxed) excited states. Excited state diffusion is thus tightly correlated to the microstructure, and we will see in more details how this has been improved toward more efficient charge photogeneration in section 1.3.1.

Electron transfer after donor excitation (eq. 1.1), and similarly hole transfer after acceptor excitation (eq. 1.2), form an interfacial electron-hole-pair $\left[D^+ \cdots A^- \right]$ as described by the following equations:

$$D + A \xrightarrow{h\upsilon} D^* + A \underset{k_{ET}}{\rightleftharpoons} \left[D^+ \cdots A^- \right] \underset{CS}{\rightleftharpoons} D^+ + A^- \tag{1.1}$$

$$D + A \xrightarrow{h\upsilon} D + A^* \underset{k_{HT}}{\rightleftharpoons} \left[D^+ \cdots A^- \right] \underset{CS}{\rightleftharpoons} D^+ + A^- \tag{1.2}$$
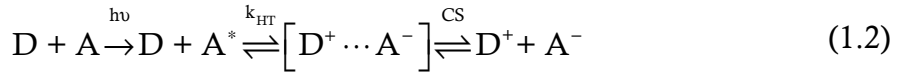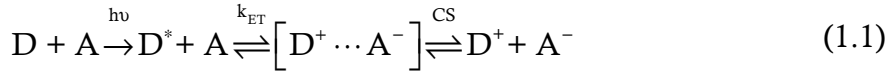
The interfacial electron-hole pair is geminate and bound, and further separates into free charges. This geminate electron-hole pair is called an interfacial charge transfer (CT) state, and can recombine (geminate recombination, gCR) back to the ground state. This recombination is represented in Figure 1.2 by the second dotted arrow. Free charge carrier recombination after charge separation (CS) can also occur.
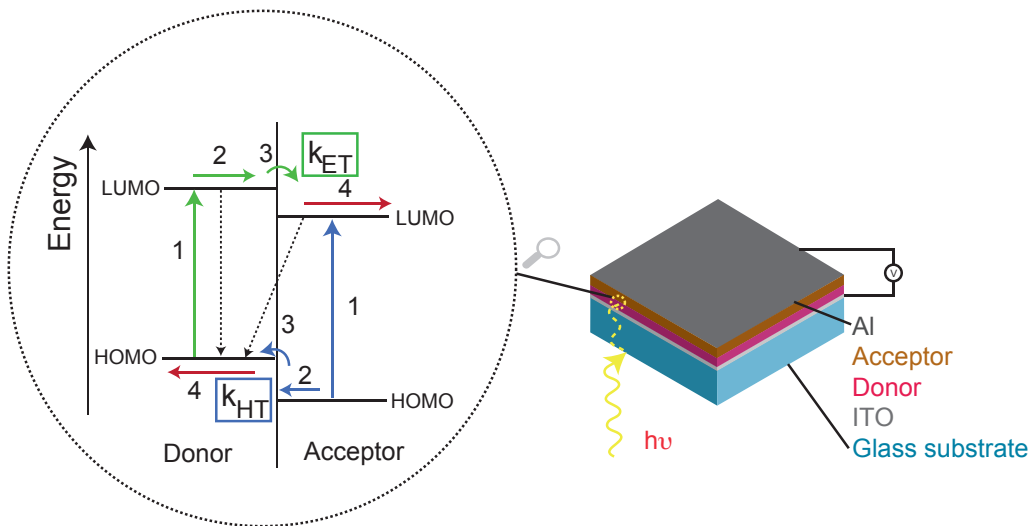
Figure 1.2 Scheme of an organic photovoltaic (OPV) device (right): electron donor D and acceptor A layers sandwiched between two electrodes. Aluminium (Al) and Indium tin oxide (ITO) electrodes collect electrons and holes, respectively. On the left, an energy level diagram for a D/A interface in open circuit conditions. Green and blue arrows stand for transitions leading to electron and hole transfer, respectively. 1) light absorption, 2) exciton diffusion, 3) electron or hole transfer, 4) charge separation and transport to the electrodes (red arrows). Dotted arrows from left to right indicate exciton and charge recombination, respectively.

From equation 1.2, we see that the acceptor can also absorb light and enhance charge generation yield by hole transfer (Figure 1.2). Having donor and acceptor materials of different band gaps increases light harvesting. Typically, conjugated polymers or molecules are used as electron donors and light absorbers, electron acceptor being commonly a fullerene derivative. The different materials and components will be further described in section 1.3.

1.2.4 Terms and definitions

Numerous terms describing photoinduced reactions in organic semiconductors flourish in the literature. To briefly restate the nomenclature, here is a concise description:

- Excited state is the result of light absorption in a pure (pristine) organic semiconductor. This is also called an exciton. Two types of excitons can occur. The first one is intramolecular, localized on one molecule and called Frenkel exciton. The second type of exciton is intermolecular, where the distance between the electron in the excited state and its ground state (where now a hole remains) is larger than the Frenkel exciton. This delocalized excited state can only exist if the neighboring (similar) molecules have degenerate excited state energy levels. This state is thus accessible only in pure materials. Delocalization implies long-range charge separation, which is also called a delocalized charge transfer state. It displays a static electrical dipole, which can be observed by Stark spectroscopy. This delocalized excited state can localize back on one molecule to the Frenkel exciton, or definitely separate into free charge carriers.

  Finally, the Wannier-Mott exciton found in band semiconductors is a completely delocalized exciton, which can be modeled as a hydrogenlike system. These excitons typically exist in inorganic semiconductors.

- The product of electron/hole transfer (equations 1.1 and 1.2) can be an interfacial bound charge transfer state, or directly free charge carriers. We call the CT state interfacial to differentiate it from the delocalized excited (or CT) state. This is similar to a geminate electron-hole pair.

- At first, the excited state (similarly the CT state) may be high in vibrational energy: hot state. Cooling down of this hot state by vibrational relaxation leads to a relaxed state, or cold state. We will further call the low lying states relaxed states. A relaxed CT state is also sometimes called charge transfer exciton.

- Free charge carriers (as opposed to bound pairs, or CT states) have successfully dissociated from Coulombic attraction and are further spatially separated. These species are called free electrons and holes in organic semiconductors. Chemically, these are reduced and oxidized states.

- A polaron is a charge carrier associated with the conformational change of the lattice, which shows vibrational signatures and can be Raman active. Although widely used in the scientific community, we will not use this term in this thesis, as the spectroscopic techniques involved in this work do not probe lattice interactions. Nevertheless, broad photoinduced signatures in transient absorption spectra are polaronic signatures.

With this review of photoinduced processes occurring in OPV devices, we will take a deeper look at the type of materials used.

1.3 On the way to high efficiency

Tremendous efforts over the last years have demonstrated a steep rise in power conversion efficiency of OPV devices. This section summarizes the history of OPV, from the first discoveries of organic photovoltaics to current state of the art.

1.3.1 A little bit of history

As we have already seen, the photoexcitation of organic semiconducting materials leads to a neutral excited state (exciton), and not directly to free charge carriers as opposed to inorganic semiconductors. The exciton binding energy is about 200-400 meV, much larger than kT (25 meV) or exciton binding energy in silicon inorganic semiconductor (14 meV).[4] The built-in field resulting from the different potential of the metallic electrodes is a driving force that pulls the electron-hole pair further apart. This force depends on the active layer thickness, and therefore usually thin films of less than 100 nm are used.[13] However, if the active layer consists of a single pure organic semiconducting material, a Schottky barrier forms at the metallic electrode which leads to low device performances.[14] A major breakthrough was introduced by Tang in 1986, where two organic semiconducting materials were deposited in a bilayer configuration between two electrodes to yield 1% power conversion efficiency.[12] One material was p-type, conducting holes (phtalocyanine) whereas the other was n-type transporting electrons (perylene). The geometrical separation of electron and hole transporting materials enabled to avoid charge recombination impeding losses. Fullerene C_{60} was used as an electron acceptor for the first time in 1992 and evidenced ultrafast photoinduced electron transfer from polymer photoexcitation.[15] For this reason and combined with its high electron mobility it is still used in state of the art devices today. Small exciton diffusion lengths on the order of 10-15 nm still hindered charge injection at the interface of bilayers.

Using bulk heterojunctions (BHJ) has solved this drawback, where both n- and p- type materials intermix on the nanometer scale, substantially increasing the D/A interface area.[16] This microstructure favors charge generation, but can affect charge carrier mobility due to poor percolation pathways to the electrodes. Today, improvements are directed toward a microstructural control in order to efficiently generate free charges, as well as transport them to the electrodes. Recent developments have shown up to 11% efficiency for polymer solar cells, and up to 9% for small molecule solar cells in 2015.[3,17]

1.3.2 Polymer-based organic photovoltaics

Polymer:fullerene blends offer the best power conversion efficiency amongst the organic photovoltaic devices, up to 11%.[3] Polymers used are for example based on polyphenylenevinylene (PPV), polythiophene or polyfluorene.[18] Besides organic photovoltaics, they are also used in OLED and OFET. Control of the molecular weight and polydispersity is a crucial factor compared to small molecules.[8] Interpenetrated networks of donor and acceptor in BHJ blends have recently revealed to be quite complex.[19] Indeed, the microstructure on the nanoscale is far from being understood and, as it governs charge photogeneration and transport, efforts are directed toward control of polymer:fullerene intercalation. Multiple studies have investigated the processing methods that influence microstructure, and enabled higher device performances.[20,21] Fatty acid methyl ester compounds and diiodooctane are used as additives during the blend layer deposition in order to yield not only pure domains but also more intimately mixed polymer:fullerene domains.[21-24] This intercalated region is responsible for ultrafast charge generation in poly(2,5-bis(3-alkyl-thiophene-2-yl)thieno[3,2-b]thiophene) (pBTTT):fullerene blends, and pure domains offer good percolation pathways for extracting charge carriers.[25] This model system is suitable for the in-depth study of the first steps following light absorption, which is presented in Chapter 5.

1.3.3 Small-molecule organic photovoltaics: cyanine-case

Molecular semiconductors such as dyes and pigments are widely used in inks and photography, to only name a few. Compared to polymers, small molecules offer a large panel of advantages like ease of synthesis, monodisperse behavior as well as high purity.[26-28] Amongst them, we can cite oligothiophenes, fullerenes, acenes, diketopyrrolopyrroles, and push-pull chromophores such as cyanines.[28] Power conversion efficiencies have reached beyond 9% for single junction solar cells based on thiophene units.[17,29,30] Although these reports are based on bulk heterojunction blends, bilayer heterojunction are rather common for small molecule PV due to processing methods. Indeed, vacuum processing of small molecules is relatively easy and allows for accurate control of the microstructure.[31] Tandem cells of vacuum deposited small molecules have reached 12% and are commercially available at Heliatek (www.heliatek.com).

Solar cells built from cyanine dye and fullerene electron acceptor are particularly interesting. Indeed, spontaneous phase de-mixing in blends of the two materials forms bulk heterojunctions characterized by a rich variety of phase morphologies.[32] On the other hand, bilayer solar cells based on the cyanine dye Cy3 (1,1'-diethyl-3,3,3',3'-tetramethylcarbocyanine) in particular, have shown competitive photovoltaic power conversion efficiency, reaching 3.7%.[26,33-37]

Cyanines are positively charged polymethine dyes and are paired with a negatively charged counter-ion. The type of counter-anion dictates the photoinduced reactions.[38] In this work, intra ion-pair reductive quenching is addressed for the specific case of a cyanine dye with borate counter-anion in Chapter 3.

Cyanine absorption spectrum can be tuned from the ultra-violet to the near-infrared, by increasing the number of double bonds. This provides not only the possibility for almost transparent devices, but also mixtures of different cyanine dyes for better solar harvesting efficiency.[38,39] Their high extinction coefficient (as an example, Cy3-C is characterized by ε (sol, 553 nm) = 140 000 L/mol·cm)

enables the use of thin active layers, minimizing the drawback related to short exciton diffusion length.[40] The solubility of cyanine dyes in various organic solvents renders them solution-processable and applicable for low-cost solar cells.[34]

Fullerene C_{60} and its derivatives are widely used in OPV devices as electron acceptors.[41] This class of materials shows high electron mobility combined with relatively easy processing methods.[42]

Cyanine/fullerene bilayers (planar heterojunction) reveal a well defined donor/acceptor interface, which is of great interest for the study of charge transfer processes.[43] The use of thin active layers is however crucial for efficient exciton diffusion toward the interface, much more than in bulk heterojunctions. Bilayers also offer the possibility for studying transport in pure materials. Optical investigations of charge transfer and transport in cyanine/fullerene bilayers are covered in Chapter 4.

1.4 Ultrafast optical probing of photoinduced charge separation

Photogeneration of charge carriers in organic photovoltaic devices is determined by four major contributors. In sequence, they are efficiencies of (i) light absorption, (ii) exciton diffusion, (iii) charge formation and separation and finally (iv) charge transport and collection.[9] The first limitation in light absorption is lifted by development of new low band gap materials. Second, the bottleneck of limited exciton diffusion has been considerably alleviated by the use of bulk heterojunction blends. Yet, the two last factors however are limiting device performances, and in particular consensus for a charge separation mechanism in OPV devices has not been attained as per today.

We will first review the charge separation mechanism suggested from various investigations reported in the literature. Dynamics of charge generation are

revealed by transient absorption spectroscopy (TAS). This technique enables following the excited state dynamics and quenching in the presence of an electron acceptor. They also relate to a certain extent the efficiency of charge generation upon microstructure and donor:acceptor ratio in blends by comparing the relative amplitudes of charge absorption (at least qualitatively). In fact, Clarke et al. established that the charge separation efficiency is the major limiting factor in polymer:fullerene blends and they also correlate the internal quantum efficiency (IQE) to the charge absorption amplitude revealed by TAS.[9,44] Typical transient absorption pump-probe setup is described in more details in Chapter 2. Other techniques revealing the ultrafast charge generation processes are briefly described in the next section.

1.4.1 Charge generation mechanism

The ultrafast dynamics of a charge transfer process in about 45 fs was first reported by Brabec et al. in 2001.[45] Since, numerous studies have investigated the charge generation and separation in polymer:fullerene blends. Grancini et al. reported generation of free charge carriers within 50 fs for PCPFTBT:PCBM blends due to hot CT states.[46] Actually, it is not yet clear whether charge transfer states or directly free charge carriers are generated upon electron transfer. An interfacial charge transfer state results from the electron-hole binding energy due to Coulombic attraction. The charge pair needs to overcome this potential barrier to successfully separate. Most likely, both CT and free charge carriers are generated on ultrafast time scales.[47] The CT dissociation in free charges is assumed to be field-dependent, in contrary to free charge carrier generation is not.[48,49] Moreover, CT states are implied when very efficient exciton quenching is observed whereas charge generation yield is low.[9] Dimitrov et al. clearly state that photoluminescence quenching should not be used as a unique tool to determine charge generation, as the yield of separated charges is not linked with

exciton quenching efficiency.[9] Rather, the competing pathway of CT relaxation at the interface counteracts charge dissociation.

Other studies reported a constant IQE across the absorbance spectra, which indicate that photon energy, hence hot excitations, are not the origin of free charge carrier generation.[48,50] Instead, relaxed (cold) CT states are argued as the major source of charge generation as demonstrated by Vandewal et al.[51]

The intricate issue of forming a relaxed CT state is that the electron-hole binding energy needs to be overcome, whereas hot CT states already contain excess energy to drive efficient charge separation. The Onsager-Braun model can be used to describe the CT state separation by considering its finite lifetime.[7,47,52,53] Several drawbacks arose from this model, especially when comparing it to Monte Carlo simulations. Disorder is not included in the Onsager-Braun model, but it has however been shown to help charge generation in 1995.[54] More recently, Vithanage et al. evidenced that charge diffusion in a disordered medium governs the charge separation process in P3HT:PCBM blends.[55]

The effect of the electric field on charge generation also indicates the existence of CT states.[56] One method to investigate this, is time-delayed collection field (TDCF), which is also a pump-probe technique. A constant bias voltage is applied to the sample when a short excitation beam arrives. After some delay, the voltage is turned into collection bias in order to extract all free charge carriers.[51] With such experimental method, Albrecht et al. demonstrated field dependence in free carrier generation.[57] The drawback of this technique is the low time resolution, about 10 ns. Ultrafast methods include the transient Stark effect spectroscopy and time-resolved electric field induced second harmonic generation (TREFISH).[42,55,58,59] These two techniques are sub-picosecond optical probes of the electric field dynamics within a sample. They are essentially employed for tracking charge transport through the active layer material, but they also give insight into the electric field dependent charge separation. We will address this in more details in Chapter 4 and 5.

High local mobility has been suggested for efficient CT separation process by Burke et al.[60] Terahertz mobility up to 11 cm^2/V·s is sufficient to drive charge

separation, even without an energy cascade. Pranculis et al. also concluded that high electron mobility in fullerene was enough to explain charge separation in polymer:fullerene blends.[61]

Charge delocalization has recently been suggested to play a crucial role in free charge photogeneration.[62-64] Pump-push photocurrent (PPP) measurements provided by Bakulin et al. demonstrated that hot states are precursors for free charge generation due to their delocalization. Vibrational dynamics of polaron photogeneration have been followed by Provencher et al. by femtosecond stimulated Raman spectroscopy (FSRS).[65] They demonstrated long-range charge separation significantly faster than 300 fs. These results indicate ultrafast polaron formation without access through a CT state.

Fullerene and derivatives are commonly used as electron acceptors mostly due to their high electron mobility, up to 1 $cm^2/V\cdot s$. Pure fullerene domains are of fundamental importance in charge generation: an energetic driving force for electrons being induced by PCBM crystallization, as demonstrated by Jamieson et al.[66] Selective PCBM excitation in blends has led to increased photocurrent values resulting from PCBM hole transfer.[67] Gélinas et al. actually demonstrated for the first time that electron delocalization due to fullerene clusters is responsible for long-range ultrafast charge separation (4 nm in 40 fs).[64]

We have seen that ultrafast techniques are needed for a clear understanding of the operating principles. But yet, photogeneration of charge pairs has not reached a consensus.[68] Most ultrafast studies have focused on polymer:fullerene blends, and little is directed toward small molecule devices, even less toward bilayers.[42,69-71] Molecular level engineering of organic semiconductors enrich the panel of chemical structures, crystallinity, microstructure and disorder to only name a few, enhancing the diversity of physical properties. This short review also emphasizes the importance of electric field dependent measurements, as bound interfacial charge transfer states and free charge carriers are likely formed upon charge transfer in organic solar cells.

A main approach to investigate ultrafast charge formation and separation is transient absorption spectroscopy. In this thesis work, we have observed oscillatory photoabsorptions in TA data on ultrashort timescales, which we assign to a Stark effect. We will shortly introduce this effect in the following lines.

1.4.2 Photoinduced Electroabsorption: Stark effect

Local electric fields induced by photogenerated charge carriers and charge transfer states strongly affect the electronic transitions in the surrounding molecules.[5,72-77] Electroabsorption corresponds to the change in absorption spectrum due to an electric field, be it applied externally or locally due to photogenerated transient species.[78] This phenomenon is also called the Stark effect.[79] An electric field will affect the change in dipole moment $\Delta\mu$ and/or the change in polarizability $\Delta\alpha$ of the ground to excited state transition. These changes can be determined from Stark measurements as electroabsorption (EA) is derived from first, second and higher order derivatives of the absorption spectrum:

$$EA = A\left(\upsilon, E\right) - A\left(\upsilon, E = 0\right) = -\frac{dA}{d\upsilon}\Delta\mu \cdot E + \frac{1}{2}\frac{d^2A}{d\upsilon^2}\cdot E^2 \cdot \Delta\mu^2 - \frac{1}{2}\frac{dA}{d\upsilon}\Delta\alpha \cdot E^2 \quad (1.3)$$

where υ is frequency and E is the applied electric field.

The first term is linear in the field and reaches zero for isotropic samples such as pure molecular systems, as the field vector orientation is averaging over all possible directions. Ordered materials, such as dyes anchored to TiO_2 particles show linear electroabsorption with an external applied electric field.[80,81]

The second term in eq. 1.3 shows that changes in dipole moment are associated with the second derivative of absorption, while the last term associates the change in polarizability to the first derivative of absorption. Both latter terms are

quadratic with the field and can therefore be observed even if the macroscopic field is zero.[64]

Oscillatory features in transient absorption spectra can thus be associated with EA caused by free charge carriers, or electron-hole pairs (dipoles). The magnitude of the electric field generated is not trivial for photoinduced electroabsorption, as it depends on the geometry of the sample (planar or bulk heterojunction) and the position of the molecule affected by the electric field. Nevertheless, dynamics of electroabsorption can give further insight into charge separation and recombination. This technique is addressed in Chapter 4 and 5 where we observe photoinduced EA of cyanine, fullerene and a polymer (pBTTT) in transient absorption spectra.

1.4.3 Charge transport on the nanoscale

Charge transport and collection is the second limiting factor for organic photovoltaics, after charge photogeneration. Indeed, low carrier mobility is an intrinsic feature of organic semiconductors, on the order of 10^{-2}cm^2/(V·s) and lower. Compared to typical inorganic semiconductors, this is several orders of magnitude smaller.[4,82] Transport is tightly linked to material processing methods, microstructure, and thus disorder.[83,84] Here we don't go into a detailed description of charge transport in organic semiconductors, but references 82 and 84 provide excellent reviews on this topic.

We have to distinguish charge transport by diffusion from charge drift mechanism occurring under applied electric fields. In operating conditions, charges experience a built-in field which directs them toward the electrode, with a drift velocity $v = \mu \cdot E$. We will only consider charge transport under electric fields.

Charge transport characterized with conventional methods such as time-of-flight (TOF) is averaged over time, without dynamical information. It was however suggested using this method that the initial transport could be fast, though

limited by time resolution of about ns.[85] Knowing that charge carriers are generated on ultrafast timescales, ns timescale is too slow. Above all, charge transport on the nanoscale would provide guidance on long-range charge transport which is thus applicable for OFET for example.

Investigating charge transport on sub-picosecond timescales in organic photovoltaics was made possible by implementation of the transient Stark effect spectroscopy in 2002, and followed by time-resolved electric field induced second harmonic generation (TREFISH) in 2009.[58,59] These pump-probe methods rely on the decrease of an externally applied electric field due to charge carrier drift toward the electrodes. The light pulse sets the time resolution, hence sub-picosecond timescales are accessible by using fs lasers. This allows to follow the dynamics of electron-hole separation with time. The actual average distance between charge pairs as well as their mobility can be extracted from the electric field dynamics, if charge carrier generation is prompt (< 100 fs). Results obtained for polymer and merocyanine blends with PCBM emphasize the time-dependent mobility, decreasing by several orders of magnitude during the first nanosecond after optical excitation.[42,55,86] Increasing the fullerene content rises electron mobility on ultrafast timescales, which suggests that fullerene domains are by their nature sufficient to enhance charge separation.[61] More technical details of the transient Stark effect spectroscopy in Chapter 2.

We shall focus on ultrafast dynamics of charge transport (< 1 ns) to investigate both cyanine- and polymer-based photovoltaic devices. In fact, this thesis introduces charge dynamics followed by transient Stark effect spectroscopy in such devices for the first time. The results are presented in Chapter 4 and 5.

With this introduction, we see that investigations and understanding of the elementary processes involved in organic semiconductors are of paramount interest. Kinetics of charge separation and transport to electrodes have to be faster than competing recombination and deactivation pathways to achieve high efficiencies. In the next chapter, we will go into more details of the optical techniques used in this thesis work for achieving our goals.

1.5 References

(1) Moser, J.-E. Photochemistry, Lecture Notes, EPFL, 2006; pp. 1–51.

(2) Puttgen, H. B. *"Les défis énergétiques de la Suisse : les bâtiments au coeur du débat," Lecture, Beaulieu, Lausanne* **2014**.

(3) Green, M. A.; Emery, K.; Hishikawa, Y.; Warta, W.; Dunlop, E. D. *Prog. Photovolt: Res. Appl.* **2015**, *23*, 1–9.

(4) Nüesch, F. Organic Semiconductors, Lecture Notes, EPFL, 2012; pp. 1–27.

(5) Lanzani, G. *The photophysics behind photovoltaics and photonics*; Wiley-VCH, 2012.

(6) Hoppe, H.; Sariciftci, N. S. *J Mater Res* **2004**, *19*, 1924–1945.

(7) Clarke, T. M.; Durrant, J. R. *Chem. Rev.* **2010**, *110*, 6736–6767.

(8) Mazzio, K. A.; Luscombe, C. K. *Chem Soc Rev* **2015**, *44*, 78–90.

(9) Dimitrov, S. D.; Durrant, J. R. *Chem. Mater.* **2014**, *26*, 616–630.

(10) Devižis, A. Charge carrier transport in conjugated polymer films revealed by ultrafast optical probing, Thesis Vilnius University, 2011, pp. 1–102.

(11) Shirakawa, H.; Louis, E. J.; MacDiarmid, A. G.; Chiang, C. K.; Heeger, A. J. *J. Chem. Soc., Chem. Commun.* **1977**, 578.

(12) Tang, C. W. *Applied Physics Letters* **1986**, *48*, 183.

(13) Kirchartz, T.; Agostinelli, T.; Campoy-Quiles, M.; Gong, W.; Nelson, J. *J. Phys. Chem. Lett.* **2012**, *3*, 3470–3475.

(14) Ghosh, A. K.; Feng, T. *Journal of Applied Physics* **1978**, *49*, 5982.

(15) Sariciftci, N. S.; Smilowitz, L.; Heeger, A. J.; Wudl, F. *Science* **1992**, *258*, 1474–1476.

(16) Yu G; J, G.; C, H. J.; F, W.; J, H. A. *Science* **1995**, *270*, 1789–1791.

(17) Zhang, Q.; Kan, B.; Liu, F.; Long, G.; Wan, X.; Chen, X.; Zuo, Y.; Ni, W.; Zhang, H.; Li, M.; Hu, Z.; Huang, F.; Cao, Y.; Liang, Z.; Zhang, M.; Russell, T. P.; Chen, Y. *Nature Photon* **2015**, *9*, 35–41.

(18) Günes, S.; Neugebauer, H.; Sariciftci, N. S. *Chem. Rev.* **2007**, *107*, 1324–1338.

(19) Huang, Y.; Kramer, E. J.; Heeger, A. J.; Bazan, G. C. *Chem. Rev.* **2014**, *114*, 7006–7043.

(20) Hoppe, H.; Sariciftci, N. S. *J. Mater. Chem.* **2006**, *16*, 45–61.

(21) Zusan, A.; Gieseking, B.; Zerson, M.; Dyakonov, V.; Magerle, R.; Deibel, C. *Sci Rep* **2015**.

(22) Buchaca-Domingo, E.; Ferguson, A. J.; Jamieson, F. C.; McCarthy-Ward, T.; Shoaee, S.; Tumbleston, J. R.; Reid, O. G.; Yu, L.; Madec, M. B.; Pfannmöller, M.; Hermerschmidt, F.; Schröder, R. R.; Watkins, S. E.; Kopidakis, N.; Portale, G.; Amassian, A.; Heeney, M.; Ade, H.; Rumbles, G.; Durrant, J. R.; Stingelin, N. *Materials Horizons* **2014**, *1*, 270–279.

(23) Westacott, P.; Tumbleston, J. R.; Shoaee, S.; Fearn, S.; Bannock, J. H.;

Gilchrist, J. B.; Heutz, S.; deMello, J.; Heeney, M.; Ade, H.; Durrant, J.; McPhail, D. S.; Stingelin, N. *Energy Environ. Sci.* **2013**, *6*, 2756–2764.

(24)   Miller, N. C.; Cho, E.; Junk, M. J. N.; Gysel, R.; Risko, C.; Kim, D.; Sweetnam, S.; Miller, C. E.; Richter, L. J.; Kline, R. J.; Heeney, M.; McCulloch, I.; Amassian, A.; Acevedo-Feliz, D.; Knox, C.; Hansen, M. R.; Dudenko, D.; Chmelka, B. F.; Toney, M. F.; Brédas, J.-L.; McGehee, M. D. *Adv. Mater.* **2012**, *24*, 6071–6079.

(25)   Scarongella, M.; Paraecattil, A. A.; Buchaca-Domingo, E.; Douglas, J. D.; Beaupré, S.; McCarthy-Ward, T.; Heeney, M.; Moser, J. E.; Leclerc, M.; Fréchet, J. M. J.; Stingelin, N.; Banerji, N. **2014**, *2*, 6218.

(26)   Lloyd, M.; Anthony, J. *Materials Today* **2007**, *10*, 34–41.

(27)   Walker, B.; Kim, C.; Nguyen, T.-Q. *Chem. Mater.* **2011**, *23*, 470–482.

(28)   Mishra, A.; Bäuerle, P. *Angew. Chem. Int. Ed. Engl.* **2012**, *51*, 2020–2067.

(29)   Meerheim, R.; Körner, C.; Leo, K. *Applied Physics Letters* **2014**, *105*, 063306.

(30)   Liu, Y.; Chen, C.-C.; Hong, Z.; Gao, J.; Yang, Y. M.; Zhou, H.; Dou, L.; Li, G.; Yang, Y. *Sci Rep* **2013**, *3*, 3356.

(31)   Riede, M.; Mueller, T.; Tress, W.; Schueppel, R.; Leo, K. *Nanotechnology* **2008**, *19*, 424001.

(32)   Heier, J.; Groenewold, J.; Huber, S.; Nüesch, F.; Hany, R. *Langmuir* **2008**, *24*, 7316–7322.

(33)   Fan, B.; Araujo De Castro, F.; Heier, J.; Hany, R.; Nüesch, F. *Organic Electronics* **2010**, *11*, 583–588.

(34)   Wicht, G.; Bücheler, S.; Dietrich, M.; Jäger, T.; Nüesch, F.; Offermans, T.; Tisserant, J.-N.; Wang, L.; Zhang, H.; Hany, R. *Solar Energy Materials and Solar Cells* **2013**, *117*, 585–591.

(35)   Jenatsch, S.; Hany, R.; Véron, A. C.; Neukom, M.; Züfle, S.; Borgschulte, A.; Ruhstaller, B.; Nüesch, F. A. *J. Phys. Chem. C* **2014**, *118*, 17036–17045.

(36)   Malinkiewicz, O.; Grancha, T.; Molina-Ontoria, A.; Soriano, A.; Brine, H.; Bolink, H. J. *Adv. Energy Mater.* **2012**, *3*, 472–477.

(37)   Mishra, A.; Behera, R. K.; Behera, P. K.; Mishra, B. K.; Behera, G. B. *Chem. Rev.* **2000**, *100*, 1973–2012.

(38)   Heier, J.; Peng, C.; Véron, A. C.; Hany, R.; Geiger, T.; Nüesch, F. A.; Vismara, M. V.; Graeff, C. F. **2014**, 918408–918408–10.

(39)   Véron, A. C.; Zhang, H.; Linden, A.; Nüesch, F.; Heier, J.; Hany, R.; Geiger, T. *Org. Lett.* **2014**, *16*, 1044–1047.

(40)   Hany, R.; Fan, B.; de Castro, F. A.; Heier, J.; Kylberg, W.; Nüesch, F. *Prog. Photovolt: Res. Appl.* **2011**, *19*, 851–857.

(41)   Guldi, D. M.; Prato, M. *Accounts of chemical research* **2000**, *33*, 695–703.

(42)   Devižis, A.; Hertel, D.; Meerholz, K.; Gulbinas, V.; Moser, J. E. *Organic Electronics* **2014**, *15*, 3729–3734.

(43)   Berner, E.; Jäger, T.; Lanz, T.; Nüesch, F.; Tisserant, J.-N.; Wicht, G.; Zhang, H.; Hany, R. *Applied Physics Letters* **2013**, *102*, 183903.

(44) Clarke, T. M.; Ballantyne, A.; Shoaee, S.; Soon, Y. W.; Duffy, W.; Heeney, M.; McCulloch, I.; Nelson, J.; Durrant, J. R. *Adv. Mater.* **2010**, *22*, 5287–5291.

(45) Brabec, C. J.; Zerza, G.; Cerullo, G.; De Silvestri, S.; Luzzati, S.; Hummelen, J. C.; Sariciftci, S. *Chemical Physics Letters* **2001**, *340*, 232–236.

(46) Grancini, G.; Maiuri, M.; Fazzi, D.; Petrozza, A.; Egelhaaf, H.-J.; Brida, D.; Cerullo, G.; Lanzani, G. *Nat Mater* **2013**, *12*, 29–33.

(47) Gao, F.; Inganäs, O. *Phys. Chem. Chem. Phys.* **2014**.

(48) Zusan, A.; Vandewal, K.; Allendorf, B.; Hansen, N. H.; Pflaum, J.; Salleo, A.; Dyakonov, V.; Deibel, C. *Adv. Energy Mater.* **2014**, *4*.

(49) Augulis, R.; Devižis, A.; Peckus, D.; Gulbinas, V.; Hertel, D.; Meerholz, K. *J. Phys. Chem. C* **2015**, 150225165209008.

(50) Lee, J.; Vandewal, K.; Yost, S. R.; Bahlke, M. E.; Goris, L.; Baldo, M. A.; Manca, J. V.; Van Voorhis, T. *Journal of the American Chemical Society* **2010**, *132*, 11878–11880.

(51) Vandewal, K.; Albrecht, S.; Hoke, E. T.; Graham, K. R.; Widmer, J.; Douglas, J. D.; Schubert, M.; Mateker, W. R.; Bloking, J. T.; Burkhard, G. F.; Sellinger, A.; Fréchet, J. M. J.; Amassian, A.; Riede, M. K.; McGehee, M. D.; Neher, D.; Salleo, A. *Nat Mater* **2014**, *13*, 63–68.

(52) Onsager, L. *Phys. Rev.* **1938**, *54*, 554–557.

(53) Braun, C. L. *The Journal of Chemical Physics* **1984**, *80*, 4157–4161.

(54) Albrecht, U.; Bässler, H. *Chemical Physics Letters* **1995**, *235*, 389–393.

(55) Amarasinghe Vithanage, D.; Devižis, A.; Abramavičius, V.; Infahsaeng, Y.; Abramavičius, D.; MacKenzie, R. C. I.; Keivanidis, P. E.; Yartsev, A.; Hertel, D.; Nelson, J.; Sundström, V.; Gulbinas, V. *Nat Comms* **2013**, *4*, 2334.

(56) Morteani, A.; Sreearunothai, P.; Herz, L.; Friend, R.; Silva, C. *Phys. Rev. Lett.* **2004**, *92*, 247402.

(57) Albrecht, S.; Schindler, W.; Kurpiers, J.; Kniepert, J.; Blakesley, J. C.; Dumsch, I.; Allard, S.; Fostiropoulos, K.; Scherf, U.; Neher, D. *J. Phys. Chem. Lett.* **2012**, *3*, 640–645.

(58) Gulbinas, V.; Kananavičius, R.; Valkunas, L.; Bässler, H. *Phys. Rev. B* **2002**, *66*, 233203.

(59) Devižis, A.; Serbenta, A.; Meerholz, K.; Hertel, D.; Gulbinas, V. *Phys. Rev. Lett.* **2009**, *103*, 027404.

(60) Burke, T. M.; McGehee, M. D. *Adv. Mater. Weinheim* **2014**, *26*, 1923–1928.

(61) Pranculis, V.; Infahsaeng, Y.; Tang, Z.; Devižis, A.; Vithanage, D. A.; Ponseca, C. S.; Inganäs, O.; Yartsev, A. P.; Gulbinas, V.; Sundström, V. *J. Am. Chem. Soc* **2014**, *136*, 11331–11338.

(62) Bakulin, A. A.; Rao, A.; Pavelyev, V. G.; van Loosdrecht, P. H. M.; Pshenichnikov, M. S.; Niedzialek, D.; Cornil, J.; Beljonne, D.; Friend, R. H. *Science* **2012**, *335*, 1340–1344.

(63) Dimitrov, S. D.; Bakulin, A. A.; Nielsen, C. B.; Schroeder, B. C.; Du, J.; Bronstein, H.; McCulloch, I.; Friend, R. H.; Durrant, J. R. *J. Am. Chem. Soc* **2012**, *134*, 18189–18192.

(64) Gélinas, S.; Rao, A.; Kumar, A.; Smith, S. L.; Chin, A. W.; Clark, J.; van der Poll, T. S.; Bazan, G. C.; Friend, R. H. *Science* **2014**, *343*, 512–516.

(65) Provencher, F.; Bérubé, N.; Parker, A. W.; Greetham, G. M.; Towrie, M.; Hellmann, C.; Côté, M.; Stingelin, N.; Silva, C.; Hayes, S. C. *Nat Comms* **2014**, *5*, 4288.

(66) Jamieson, F. C.; Domingo, E. B.; McCarthy-Ward, T.; Heeney, M.; Stingelin, N.; Durrant, J. R. *Chem. Sci.* **2012**, *3*, 485–492.

(67) Dimitrov, S. D.; Huang, Z.; Deledalle, F.; Nielsen, C. B.; Schroeder, B. C.; Ashraf, R. S.; Shoaee, S.; McCulloch, I.; Durrant, J. R. *Energy Environ. Sci.* **2014**, *7*, 1037–1043.

(68) Few, S.; Frost, J. M.; Nelson, J. *Phys. Chem. Chem. Phys.* **2015**, *17*, 2311–2325.

(69) Shoaee, S.; Mehraeen, S.; Labram, J. G.; Brédas, J.-L.; Bradley, D. D. C.; Coropceanu, V.; Anthopoulos, T. D.; Durrant, J. R. *J. Phys. Chem. Lett.* **2014**, *5*, 3669–3676.

(70) Kaake, L. G.; Zhong, C.; Love, J. A.; Nagao, I.; Bazan, G. C.; Nguyen, T.-Q.; Huang, F.; Cao, Y.; Moses, D.; Heeger, A. J. *J. Phys. Chem. Lett.* **2014**, *5*, 2000–2006.

(71) Peckus, D.; Devižis, A.; Augulis, R.; Graf, S.; Hertel, D.; Meerholz, K.; Gulbinas, V. *J. Phys. Chem. C* **2013**, *117*, 6039–6048.

(72) Sebastian, L.; Weiser, G.; Bässler, H. *Chemical Physics* **1981**, *61*, 125–135.

(73) Chekalin, S. V.; Yartsev, A. P.; Sundström, V. *J. Exp. Theor. Phys.* **2001**, *93*, 706–716.

(74) Chekalin, S. V.; Yartsev, A. P.; Sundström, V. *Quantum Electron.* **2007**, *31*, 395–397.

(75) Cabanillas-Gonzalez, J.; Grancini, G.; Lanzani, G. *Adv. Mater.* **2011**, *23*, 5468–5485.

(76) Drori, T.; Sheng, C.-X.; Ndobe, A.; Singh, S.; Holt, J.; Vardeny, Z. V. *Phys. Rev. Lett.* **2008**, *101*, 037401.

(77) Dick, D.; Wei, X.; Jeglinski, S.; Benner, R.; Vardeny, Z.; Moses, D.; Srdanov, V.; Wudl, F. *Phys. Rev. Lett.* **1994**, *73*, 2760–2763.

(78) Bublitz, G. U.; Boxer, S. G. *Annu Rev Phys Chem* **1997**, *48*, 213–242.

(79) Stark, J. *Nature* **1913**, 1–1.

(80) Cappel, U. B.; Feldt, S. M.; Schöneboom, J.; Hagfeldt, A.; Boschloo, G. *J. Am. Chem. Soc* **2010**, *132*, 9096–9101.

(81) Ardo, S.; Sun, Y.; Castellano, F. N.; Meyer, G. J. *J Phys Chem B* **2010**, *114*, 14596–14604.

(82) Bässler, H.; Köhler, A. In *Unimolecular and Supramolecular Electronics I*; Topics in Current Chemistry; Springer Berlin Heidelberg: Berlin, Heidelberg, 2011; Vol. 312, pp. 1–65.

(83)   Pivrikas, A.; Sariciftci, N. S.; Juška, G.; Österbacka, R. *Prog. Photovolt: Res. Appl.* **2007**, *15*, 677–696.

(84)   Lanzani, G. *Photophysics of molecular materials: from single molecules to single crystals*; John Wiley and Sons, 2006.

(85)   Juška, G.; Genevičius, K.; Österbacka, R.; Arlauskas, K.; Kreouzis, T.; Bradley, D. D. C.; Stubb, H. *Phys. Rev. B* **2003**, *67*, 081201.

(86)   Melianas, A.; Pranculis, V.; Devižis, A.; Gulbinas, V.; Inganäs, O.; Kemerink, M. *Adv. Funct. Mater.* **2014**, *24*, 4507–4514.

Chapter 2

Experimental methods

« An experiment is a question which science poses to Nature, and a measurement is the recording of Nature's answer.»

Max Planck

It is now necessary to understand how photoinduced processes such as those shown in Chapter 1 can be monitored. The fundamentals of the techniques used in this thesis are explained, as well as the experimental details and all those little things papers do not tell.

Both the femtosecond transient absorption and electromodulated differential absorption measurements were based on the same laser source, which is described in the first section of this chapter. Data analysis is usually fitted globally, and the procedure for this is demonstrated here. Nanosecond flash photolysis is also briefly overviewed.

2.1 Fundamentals of ultrafast spectroscopy

2.1.1 Laser source

The first pulsed light amplification by stimulated emission of radiation, or laser, was completed by Maiman in 1960 at Hughes Research Laboratories, Malibu, California.[1] The flashlamp pumped solid-state Ruby laser could emit pulses at 694 nm. Since then, a lot of progress allowed to shorten the time window of the optical pulses up to femtoseconds.[2] Lasers have proven their applicability in various domains including industry (cutting, welding, etc.), military, medicine (e.g. eye treatment), research and more related to this thesis, spectroscopy. The coherent light source of a laser enabled to dig more into the interaction between light and matter (spectroscopy) by looking at a defined time resolution, set by the light source.

Lasers, as their name suggest, work due to stimulated emission. When a laser medium (gas, liquid or solid) is excited (pumped), a population inversion occurs where the upper state has a long excited state lifetime. As an electromagnetic radiation passes through the pumped medium, it will be amplified by stimulated emission, i.e. for one photon coming in, two photons will get out. This is called a gain. Optical pumping is achieved with a flashlamp or another laser.

Amplification becomes even more effective when the electromagnetic radiations can travel back and forth through the medium. Two reflective mirrors will ensure a suitable amplification, and they constitute what is called the laser cavity oscillator. Beyond the fact that lasers amplify light, they also do it in a coherent way. Only coherent modes will interfere constructively in the cavity, and acquire enough gain to become part of the laser output.

In order to have some laser output, the cavity has to be opened with a semi-reflective output coupler. Q-switching allows to create short pulses up to nanoseconds. The gain medium is pumped high enough, and the cavity is opened through a switch only when a sufficient population inversion is obtained. A strong stimulated emission comes out of this laser medium. Mode-locking is capable of producing very intense pulses up to several femtoseconds. Here, the phase of the modes is fixed by the cavity, causing them to interfere constructively.

Due to the Heisenberg uncertainty principle, in order to allow ultrashort pulses to exist, the gain spectra must contain a broad range of frequencies. One example of lasing media is Ti:Sapphire, which is widely used in scientific research due to its tunability and ultrashort pulses. The Al_2O_3 doped with Ti^{3+} ions absorbs around 500 nm and emits in the near-infrared (nIR). The output wavelength is tunable from 650 to 1100 nm and the average pulse duration is 100 fs.

The laser source used in this thesis is a Ti:Sapphire femtosecond laser CPA-2001 from Clark-MXR. An Er-doped fiber pumped by a diode laser constitutes the oscillator of the system, with a gain at 1550 nm. The output passes through a frequency doubler, converting it into a 775 nm beam. The pulse is stretched in time (first part of the Chirped Pulse Amplification, CPA) in order to avoid energy damages, and constitutes the seed for the Ti :Sapphire. The Ti :Sapphire rod is meanwhile pumped by the frequency-doubled output of a Nd :YAG laser (532 nm, 7.2 W) pumped by a flashlamp. The regenerative amplifier picks high intensity (amplified) pulses out of the Ti:Sapphire cavity, and sends them into a

pair of diffraction gratings to compress it back in time (second step of the CPA) to about 120 fs for an average peak power of 930 µJ at 1 kHz repetition rate.

2.1.2 Wavelength tuning

For pump-probe experiments, the laser output needs to be tuned to other wavelengths. This is commonly realized by taking advantage of nonlinear effects. Ultrashort laser pulses display high peak powers, which then affect the optical properties of a material in a nonlinear way. As a matter of fact, the dielectric polarization of the material is directly proportional to the electric field of the incoming light. At high intensities, the polarization is no longer linearly proportional to the electric field, as higher order effects appear. A short overview of the various processes is described here, but for more information other references can be consulted.[2,3]

Second order effects include second harmonic generation (SHG) and optical parametric generation (OPG) and are based on three-wave mixing and energy conservation. Optical parametric amplifier (OPA) and optical parametric oscillator (OPO) are both based on OPG. Phase-matching conditions have to be fulfilled for high intensity output, i.e. the crystal orientation and the incoming polarization need to be properly adjusted so that the different waves in the crystal interact in a constructive manner.

For SHG, a nonlinear crystal such as a BBO (β-BaB_2O_4) or BIBO (BiB_3O_6) showing high second order susceptibility is employed. Two collinear incoming photons of same energy E_1 (usually nIR range) mix in the material and a photon of twice the energy E_1 is emitted. SHG is typically used to excite the investigated sample at 390 nm, the doubled energy of the Ti:Sapphire output at about 775 nm.

OPG also makes use of a nonlinear crystal such that out of one incoming photon of energy E_2 (typically 390 nm) two photons are emitted, for which the sum of the energies equals E_2. They are called signal and idler (typically visible and nIR

range, respectively). Two-stages non-collinear OPA makes use of OPG and a second stage amplifying the desired beam. The process will be explained in more details in section 2.1.4. When the incoming beam passes many times through the crystal due to mirrors creating an optical cavity, we get an optical parametric oscillator (OPO). Rotation of the crystal enables to tune the output wavelength easily.

2.1.3 Broad band white light generation

Pump-probe experiments unravel transient species on ultrashort time scales. In these experiments, two pulsed beams are directed toward the investigated sample. The first one, pump pulse, will initiate a photoreaction such as excitation. The second pulse is a probe of the photoreaction change. Thanks to optical delays, the transient effect of a photoexcitation triggered by a pump pulse can be monitored with time. The probe can be monochromatic, and polychromatic probes are more and more used. Provided the detectors are arranged accordingly, the broad spectral range of a so-called white light continuum (or supercontinuum) probe enables to view a wide transient spectrum at a glance. Before going into the experimental details of the setup built during this work, let us understand the process of white light generation.

White light generation is done thanks to third order nonlinear effects involving four-wave mixing. When an ultrashort pulse enters a material, the refractive index is not longer linear and has a second order term (Kerr effect). This latter depends on light intensity, and thus, time. As a consequence, the phase of the incoming optical pulse shows time dependence too, which directly affects the frequency inside the incident pulse. This frequency broadening due to self-phase modulation is increased further due to the group velocity dispersion in the material, which is also called optical Kerr effect. Dispersive media such as a sapphire plate or a CaF_2 window are used to get broad spectra. The sapphire plate offers a narrower spectrum than CaF_2, but has a higher damage energy
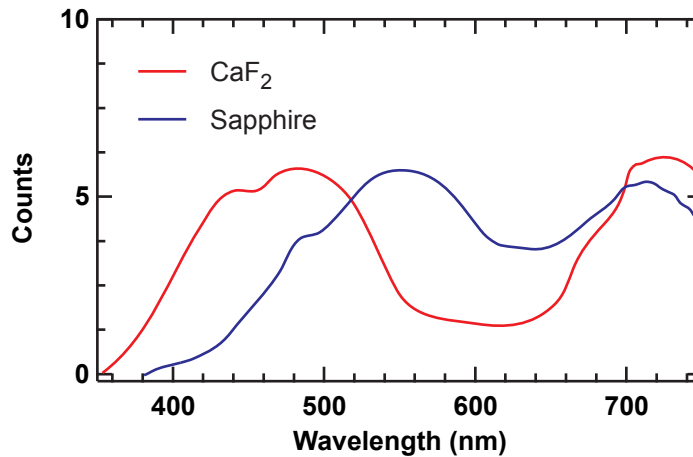
Figure 2.1 White-light continuum spectra obtained from focusing the laser fundamental (775 nm) on a CaF_2 and sapphire plate. The main difference is the onset in the UV part, increased by using a CaF_2 plate.

threshold. Both have been used during this thesis, see section 2.3 and 2.2, respectively.

2.1.4 Pump pulses

The pump excitation wavelength is tunable using a NOPA (Non-collinear Optical Parametric Amplifier), as mentioned in section 2.1.2. In this thesis, a two-stage NOPA designed by Prof. Riedle was used.[3] With about 150 µJ/pulse of the Ti:Sapphire output, the NOPA can run up to 10 µJ/pulse at the desired wavelength between 450 nm and 1250 nm, with the maximum around 530 nm. Generation between 700 and 900 nm requires an additional white-light continuum generation unit. It is however chirped (about 200 fs) due to several optics and the white-light seed itself. The beam can be compressed by a pair of prisms leading to sub-50 fs pulses, as detailed further in the text.

In the first stage, part of the incoming beam is converted into white-light in a sapphire plate, which we will call the seed. The rest of the beam is frequency-doubled (SHG) to 390 nm in a BBO crystal and split into two parts, which constitute pump beams for the first and second stage. Part of the 390 nm beam
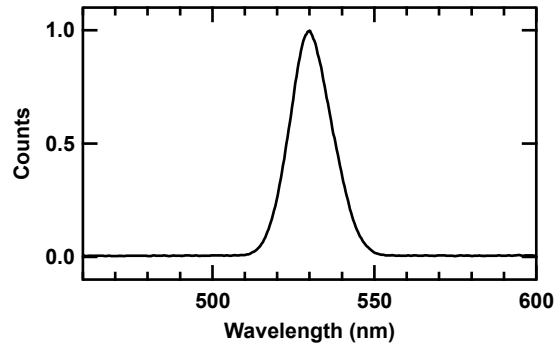
Figure 2.2 530 nm excitation pump pulse obtained after the 1st stage NOPA.

and the seed are focused and mixed in a second BBO crystal for parametric amplification as explained in 2.1.2. The output wavelength is adjusted by the angle between pump and seed, the angle of the crystal itself and the delay time of the pump. A typical output wavelength located at 530 nm obtained after the first stage is shown in Figure 2.2.

In the second stage, the seed - i.e. the output of the first stage - is focused on a third BBO with the remaining 390 nm pump beam. This amplification (up to 10 times) is exactly as the one described in the first stage.

The intensity and beam profile of the first and second stages are continuously monitored by a dual-channel spectrometer (Ocean Optics, S2000) and a powermeter (Lasermate-1, Coherent).

Pulse compression is achieved by a pair of SF10 prisms to correct for GVD. The Brewster angle is set for both prisms in order to avoid reflective losses. Passing through the first prism, the different wavelengths constituting the pulse are dispersed and sent to the second prism. There, the red part of the pulse travels more SF10 media than the blue part, that is, it is slowed down. Now that all wavelengths travel at the same time, they need to be spatially collimated. This is done by reflecting the beam back onto the pair of prisms, slightly higher than the incoming beam. The distance between the prisms varies for the desired wavelength used, and the compression is checked with a portable autocorrelator (pulseCheck, APE) placed as near as possible to the sample position (in terms of optics, not distance). The pump size and intensity at the sample are measured by

a beamprofiler (BC 106-Vis, Thorlabs) and an energy meter (Vega, Ophir), respectively.

2.2 Transient absorption

2.2.1 Fundamentals of TA

Transient absorption (TA) is a pump-probe technique that allows to get spectral and time-resolved information of electronic states after pump excitation. Ultrafast TA is based on ultrashort laser pulses. The pump triggers a perturbation of the sample at time zero. This perturbation is monitored by the probe, and both pulses are delayed by varying the optical pathlength of the pump beam with a delay stage. This time delay allows to investigate changes in absorbance from the instrument response function (IRF) of about 70 fs to 2 ns. The broadband probe enables to monitor various wavelengths at the same time, which is explained in more detail below.

The probe beam intensity transmitted through the sample depends on whether the sample has been "pumped" or not. Let's call the intensity transmitted through the sample in the presence of the pump I_p and without pump I_{np}. The absorbance of the sample in the absence (A) and presence (A + ΔA) of the pump are shown in eq. 2.1 and 2.2, respectively. The resulting change in absorbance is then obtained as shown in eq. 2.3.

$$A = -\log\left(\frac{I_{np}}{I_0}\right) \tag{2.1}$$

$$A + \Delta A = -\log\left(\frac{I_p}{I_0}\right) \tag{2.2}$$

$$\Delta A = -\log\left(\frac{I_p}{I_{np}}\right) \tag{2.3}$$

The ΔA signal holds a large amount of information. The intensity is mostly proportional to the number of excited molecules and the absorption coefficient of the transient species. The sign of the ΔA signal defines which particular species contributes to the signal:

- The sign is negative. This is the case for ground state bleaching (GSB), i.e. within the absorption range of the ground state, where the pump is absorbed by the sample. Therefore I_p is larger than I_{np} resulting in a negative ΔA (see eq. 2.3). The second reason for negative ΔA is stimulated emission (SE), where the probe triggers the radiative decay of the excited state and thus increases I_p. Stimulated emission spectra are proportionnal to the fluorescence spectra with a factor of λ^4. SE can occur from a hot state, which should be observed at very short timescales (a few fs) and possibly shifting to the red as the excited state cools down to the lowest excited state level.

- The sign is positive, indicative for a new transient species originating from the sample excitation. This can be an excited state absorption (ESA) during its lifetime, typically a few picoseconds up to nanoseconds, or other states resulting from energy or electron transfer such as oxidized and reduced species.

2.2.2 Experimental setup

The transient absorption setup used in this thesis has been built originally by S. Pelet during his thesis.[4] Further modifications have been introduced by B. Wenger.[5] A two-stage (generation and amplification) white light continuum (WLC) probe built by J. Teuscher and A. Punzi was used for initial transient absorption experiments in this thesis.[6]

A one-stage WLC setup has been implemented during this present work in collaboration with A. Marchioro and N. Banerji in order to obtain a more stable WL, even though less intense probe.[7] The scheme of the transient absorption

setup used in this thesis is shown in Figure 2.3. The generation of the WLC was improved by changing the sapphire plate by a CaF_2 crystal that gives a broader spectral range, with extended UV and IR part (about 350-1500 nm), as well as an increase in stability.[8] About 20 μJ of the output of the Clark CPA laser beam passes through an iris and a variable neutral density filter and is directed onto a 5 mm CaF_2 crystal with a 5 cm focal length lens. The focal point position can be finely adjusted on the crystal with a translation stage parallel to the beam (and a burned crystal spot can be avoided by displacing it perpendicular to the beam via a second translation stage). The CaF_2 is continuously moved by a vibration generator controlled by a function generator (djb microtech ltd, Scotland) as its damage threshold is lower than for the sapphire plate. The energy control of the incident beam enables a stable and broad WLC spectrum which is collimated by a second 5 cm focal length lens. The beam passes through a wire grid polarizer to discard any unwanted polarization residuals and bandpass filters are used to remove the remaining 775 nm from the white light. It is then directed toward a parabolic mirror and a beamsplitter (1 mm, OD 0.5). Half of the WLC is sent to the reference camera path while the rest is focused on the sample. Both beams are attenuated and directed towards their respective camera, reference and signal, with a three-axis 5 cm focal length achromatic lens.

The signal and reference beams are detected with two spectrographs (Princeton instruments, SpectraPro 2500i) equipped with a 512×58 pixels back-thinned CCD (Hamamatsu S7030-0906) and assembled by Entwicklungsbüro Stresing, Berlin. The spectrographs have two gratings: 500 nm blaze and 800 nm blaze. The first one enables the analysis of 350-800 nm WLC (visible) and requires the implementation of 350-710 nm bandpass filters to discard the excess fundamental at 775 nm. The second grating ensures the analysis of 800-1050 nm (infrared) with the implementation of 750 nm and/or 850 nm long pass filters. The wire-grid polarizer is optimized routinely for visible and infrared WLC. Careful calibration of the spectrographs is done by placing an interferential filter in the common WLC beam and controlling the grating by the computer software Mono.
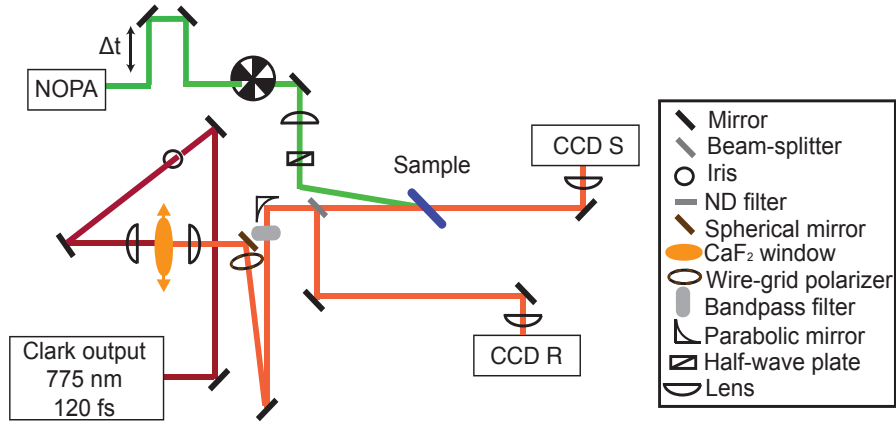
Figure 2.3 Schematic of the transient absorption setup (not to scale). The green beam is the pump, while the red beam is the fundamental of the laser (775 nm) converted into white light continuum probe beam (orange).

A shot-to-shot acquisition of the transmitted probe intensity triggers every event and the reference beam accounts for white-light fluctuations. Typically, 3000 shots are averaged in order to obtain a good signal-to-noise ratio. A chopper on the pump beam at 500 Hz enables to distinguish a transient signal (with pump) from a signal without pump, as the WLC is running at 1 kHz. Therefore we distinguish I_p^s, the intensity transmitted in the signal camera with the pump; I_{np}^s, the intensity transmitted in the signal camera without the pump; I_p^r, the intensity transmitted in the reference camera with the pump and I_{np}^r, the intensity transmitted in the reference camera without the pump. The absorbance change is then calculated via the following equation:

$$\Delta A = -\log\left(\frac{I_p^s}{I_{np}^s} \cdot \frac{I_{np}^r}{I_p^r} \right) \tag{2.4}$$

Polarizations of both pump and probe beams are set at magic angle (54.7°) with respect to each other, ensuring isotropic excitation. The dark counts on the cameras are acquired before each measurement and subtracted from the transmitted light intensity for each camera. The sensitivity is about 5.10^{-5} OD.

A Labview software (National Instruments) is used for the data acquisition. A home-built chopper has been designed where the wheel sensor detects the on and off positions (by a transmitive photomicrosensor). The slight shift between the aperture for the sensor and the aperture for the laser beam is able to account for the jitter. The chopper wheel position is routinely checked. At first, the Labview software starts a measurement ("trig enable") and enables the camera to synchronize with the laser trigger. As soon as this is done, two on/off events (4 ms) are taken. The last event determines the "FLAG", meaning the order on or off of the events. Each event is constituted of 512 pixels, which are then averaged at the end of the acquisition time.

The Labview software shows the raw WLC spectrum in real time in both signal and reference cameras, as well as the calculated transient spectra averaged over a defined number of shots. The linear dependence between pixel and wavelength on the grating is calibrated. A background spectrum is acquired before each measurement in order to account for the dark counts.

2.3 Time-resolved electroabsorption based on the Stark effect

Transient absorption spectroscopy is very useful to optically monitor transient species on ultrafast timescales. Research in the OPV field relies on the understanding of charge carrier formation, as well as their subsequent separation and drift toward the electrodes. Without any applied external field though, diffusive transport of charge carriers is observed, i.e. there is no macroscopic direction of charge diffusion. It is only under an external applied field that charge carriers drift toward their corresponding electrode. The drift velocity is proportional to both the charge carrier mobility and the external applied electric field. In order to apply electric fields on real devices, the active layer is sandwiched between two electrodes. The first one is quite transparent such as

indium tin oxide (ITO), whereas the electron accepting electrode is opaque (Al, Ag,…) and therefore requires optical measurements to be carried out in reflectance mode. There are several time-resolved experiments capable of unraveling the mechanism of charge carrier separation and transport in OPV devices on ultrafast time scales. One of them is time-resolved electroabsorption based on the Stark effect. This technique also offers the possibility to investigate steady-state electroabsorption, which is sometimes observed in transient absorption spectra such as in this work (see Chapter 4).

2.3.1 Fundamentals of electroabsorption based on the Stark effect

Let us first understand the basics of electroabsorption. Electroabsorption of a molecular material is based on the effect of an electric field on the electronic transition from the ground to the excited state. This electric field shifts the absorption spectrum of the molecular material. This is called the Stark effect and is depicted in Figure 2.4. This change in transition frequency is classically written as shown in eq. 2.5.

$$\Delta\upsilon = -\Delta\mu \cdot E - \frac{1}{2}\Delta\alpha \cdot E^2 \qquad (2.5)$$

where $\Delta\mu$ is the change in permanent dipole moment and $\Delta\alpha$ is the change in polarizability for the electronic transition. E is the applied electric field.
The applied electric field E is obtained by applying a voltage V across the sample thickness. The latter being proportional to the former, they are considered the same throughout the text (eq 2.6).
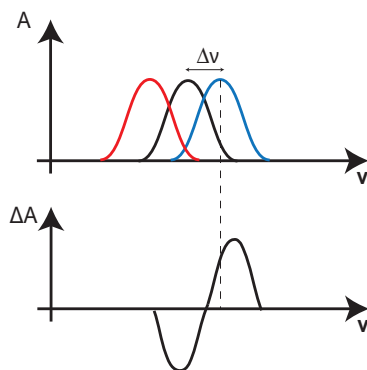
$$E = \frac{V}{D} \qquad (2.6)$$

Figure 2.4 Schematics of the effect of an applied voltage (electric field) on the absorption spectrum of a dye. The black Gaussian function represents the zero field absorption spectrum, while red and blue Gaussian functions are the field-affected spectra. The resulting change in absorbance is shown in the lower part and in this case resembles the first order derivative of the original absorption spectrum.

where V is the applied voltage (V), and D the thickness of the sample layer.

The change in absorbance due to an external applied electric field is of interest here, and the mathematical derivation is given in the following lines.[9,10] A Taylor expansion of the absorbance as a function of the transition frequency (eq. 2.7) immediately gives the change in absorbance in eq. 2.8 after rearranging and substituting eq. 2.5 in eq. 2.7. The change in absorbance with and without field is also called electroabsorption, or EA.

$$A(\upsilon,E) = A(\upsilon,E=0) + \frac{dA}{d\upsilon}d\upsilon + \frac{1}{2}\frac{d^2A}{d\upsilon^2}d\upsilon^2 + ... \qquad (2.7)$$

$$EA = A(\upsilon,E) - A(\upsilon,E=0) = -\frac{dA}{d\upsilon}\Delta\mu \cdot E + \frac{1}{2}\frac{d^2A}{d\upsilon^2} \cdot E^2 \cdot \Delta\mu^2 - \frac{1}{2}\frac{dA}{d\upsilon}\Delta\alpha \cdot E^2 \qquad (2.8)$$

The first term is linear in the field and reaches zero for isotropic samples such as pure molecular systems, as the field vector orientation is averaging over all possible orientations. Ordered materials, such as dyes anchored to TiO_2 particles show linear electroabsorption with applied field.[9,11]

The second term in eq. 2.8 shows that changes in dipole moment are associated with the second derivative of absorption, while the last term associates the
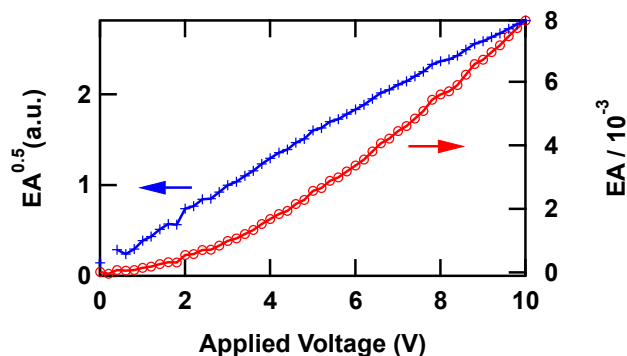
Figure 2.5 Electroabsorption as a function of applied voltage on the metal electrode for solid-state C_{60}, 80 nm. EA is quadratic versus V (red dots, right axis), which is emphasized here: √EA is linear with applied voltage (blue crosses, left axis).

change in polarizability to the first derivative of absorption. Both latter terms are quadratic with the field and can therefore be observed even if the macroscopic field is zero.[12]

The linear and quadratic in the field terms can be distinguished by measuring the electroabsorption as a function of applied voltage, as shown in Figure 2.5. Here, the EA is quadratic with the applied voltage, which is emphasized as $\sqrt{EA}$ is proportional to the applied voltage. Moreover, by calculating the first and second order derivative of the steady-state absorbance spectra, one can assign the Stark effect to a change in dipole moment or polarizability of the ground to excited state transition according to equation 2.8. However a combination of both effects can take place and is solved by a linear combination of the first and second order derivatives.[13]

2.3.2 Time-resolved electroabsorption

When an organic semiconductor is sandwiched between two electrodes, it behaves like a capacitor. An external electric field loads the capacitor. Charge carriers generated by pump excitation will separate and eventually discharge the capacitor. The decrease of the electric field sensed by the material becomes a measure of charge transport and extraction in the dielectric medium that

constitutes the polymer or small molecule layer. Measuring the charge extraction electrically is limited by the resistance times capacitance RC constant circuit, which corresponds to a few nanoseconds. That is why ultrafast optical techniques such as time-resolved electroabsorption due to the Stark effect are necessary.

In order to obtain the electric field dynamics in organic semiconductor devices, the photogenerated charges can be created by an ultrashort pump pulse and subsequently monitored by a probe pulse. The change in absorbance with and without external electric field applied can thus be investigated optically in a pump-probe way (eq. 2.9). For clarity of the discussion, the change in absorbance with a modulated external field is denoted as EDA(t), which stands for electromodulated differential absorption:

$$\mathrm{EDA}\big(t\big) = A\big(t, E\big) - A\big(t, E = 0\big)$$ (2.9)

The EDA spectrum obtained for a time t where the probe arrives before the pump is identical to the steady-state EA spectrum for the same applied voltage. The decay of electroabsorption with time is directly proportional to the electric field in the sample. This is mathematically calculated in Igor Pro software. First, the electroabsorption versus applied voltage is measured. This tells what electric field corresponds to which electroabsorption signal. The electroabsorption is then fitted with either a power law or a polynomial function. The EDA(t) dynamics is then converted using the fit of the electroabsorption into voltage, or electric field in the sample.

The integrated photocurrent I_{photo} (that is, over the first 10 μs) is measured with an oscilloscope before and after the pump-probe experiment and corresponds to the total number of extracted charges at the applied voltage and excitation fluence. The EDA dynamics monitor charges extracted from a few picoseconds to about 1.2 ns with the optical delay stage. When the electric field dynamics saturate, i.e. a plateau is observed, all photogenerated charges have been

extracted. This drop in the capacitor electric field is exactly the number of charges extracted measured by steady-state photocurrent measurements, provided space charge screening conditions are avoided. Indeed, when the number of photogenerated charges is too high, i.e. the pump fluence is too high, they will screen the applied electric field resulting in a reduced or absent drift of the photogenerated charge carriers.

One advantage of time-resolved electroabsorption due to the Stark effect compared to time-resolved electric field induced second harmonic (TREFISH)[14] is that it is spectrally resolved, giving more insight into the dynamics of electrons and holes. This is valid for bilayers only, and such results are shown in Chapter 4.

The electric field dynamics are then normalized to the maximum number of extracted charges obtained via the following relation:

$$\Delta E_{max} = \frac{\int I_{photo}(t)\,dt}{C \cdot D} \tag{2.10}$$

where C and D are the capacitance and the thickness of the sample, respectively. $I_{photo}(t)$ is the photocurrent.

Electron-hole separation distance dynamics <l(t)> can be derived from electric field dynamics. In fact, the electric field dynamics are related to the number of charges extracted by the photocurrent:[14-16]

$$\Delta E(t) = \frac{\Delta q(t)}{C \cdot D} = \frac{1}{C \cdot D} \cdot \int I_{photo}(t)\,dt \tag{2.11}$$

where $\Delta q(t)$ is the number of charges extracted.

We can also express the electric field $\Delta E(t)$ by the average drift distance <l(t)> and the density n(t) of photogenerated charge carriers:

$$\Delta E(t) = \frac{n(t) \cdot e \cdot \langle l(t) \rangle}{\varepsilon \cdot \varepsilon_0} \tag{2.12}$$

where ε is the relative permittivity of the organic layer, and ε_0 the permittivity in vacuum.

We need to take into account charge carrier extraction, and we assume prompt charge generation, therefore:

$$n(t) = n_{max} \cdot \left(1 - \frac{\langle l(t) \rangle}{D} \right)$$ (2.13)

where n_{max} is the carrier concentration successfully extracted.

We can express the photocurrent from equation 2.11, 2.12 and 2.13:

$$I_{photo}(t) = C \cdot D \frac{\partial \Delta E(t)}{\partial t} = A \cdot e \cdot n_{max} \cdot \left(1 - \frac{\langle l(t) \rangle}{D} \right) \frac{\partial l(t)}{\partial t}$$ (2.14)

where capacitance is $C = \dfrac{A \cdot \varepsilon \cdot \varepsilon_0}{D}$

Integration of the photocurrent gives the number of charges transported by the photocurrent:

$$\Delta q(t) = \int I_{photo}(t) dt = A \cdot e \cdot n_{max} \left(\langle l(t) \rangle - \frac{\langle l(t) \rangle^2}{2 \cdot D} \right)$$ (2.15)

Solving this parabolic function for <l(t)> gives:

$$\langle l(t) \rangle = D \left(1 \pm \sqrt{1 - \frac{4}{2 \cdot D \cdot A \cdot e \cdot n_{max}} \cdot \Delta q(t)} \right) = D \left(1 \pm \sqrt{1 - \frac{\Delta q(t)}{\Delta q_{max}}} \right)$$ (2.16)

For the simplification of equation 6, the maximum photocurrent Δq_{max} was calculated as:

$$\Delta q_{max} = \frac{1}{2} \cdot C \cdot D \cdot \Delta E_{max} = \frac{1}{2} \cdot C \cdot D \cdot \frac{n_{max} \cdot e \cdot \left[\langle l(t) \rangle = D \right]}{\varepsilon \cdot \varepsilon_0} = \frac{1}{2} \cdot A \cdot n_{max} \cdot e \cdot D$$ (2.17)

The factor ½ arises from the fact that both electrons and holes contribute to the photocurrent.

As $\Delta q = C.D. \Delta E$, we finally obtain:

$$\langle l(t) \rangle = D \left(1 - \sqrt{1 - \frac{\Delta E(t)}{\Delta E_{max}}} \right)$$ (2.18)

The pre square root sign was chosen negative, as the limits are:

$\langle l(t) \rangle = D$ when $\Delta E(t)/\Delta E_{max} = 1$

$<l(t)> = 0$ when $\Delta E(t)/\Delta E_{max} = 0$

The capacitance used in equations 2.10 and implied from equation 2.18 is calculated from the charges displaced by the externally applied electric field as follows:

$$Q_{dis} = \alpha + C \cdot V_{app} \qquad (2.19)$$

where α is a constant, Q_{dis} is the displaced charges, V_{app} is the applied bias. The slope of Q_{dis} versus V_{app} is the capacitance C of the sample.

2.3.3 Experimental setup

An EDA setup has been built in our laboratory by A. Devižis in 2013. This technique is based on the pump-probe setup with the ultrafast modulation of a voltage pulse. With the help of Figure 2.6, the technique can be explained easily. The pump beam is generated by a NOPA (see section 2.1.4), and the white-light continuum is obtained by self phase modulation in a 3 mm sapphire plate (see section 2.1.3). Polarizations of both beams are set at magic angle and they are focused on the sample after part of the white light continuum is sent to the reference camera. The samples are investigated in reflectance mode as a reflective counter-electrode is used, such as aluminium or silver. The Ti:Sapphire laser running at 1 kHz, the voltage pulse from a function generator (Tektronix AFG 2021) is set at 500 Hz, meaning that only one out of two successive pump pulses is in the presence of the applied voltage (see bottom Figure 2.6). The square voltage pulse has a typical duration of about 100 μs, making sure that when the pump pulse arrives, the electric field in the sample is present and stable. The probe is delayed and scanned over 1.2 ns in order to monitor the dynamics of electroabsorption. The signal and reference are detected with a pair of 163 mm spectrographs (Andor Technology, SR163) equipped with a 512×58 pixels back-thinned CCD (Hamamatsu S07030-0906) and assembled by
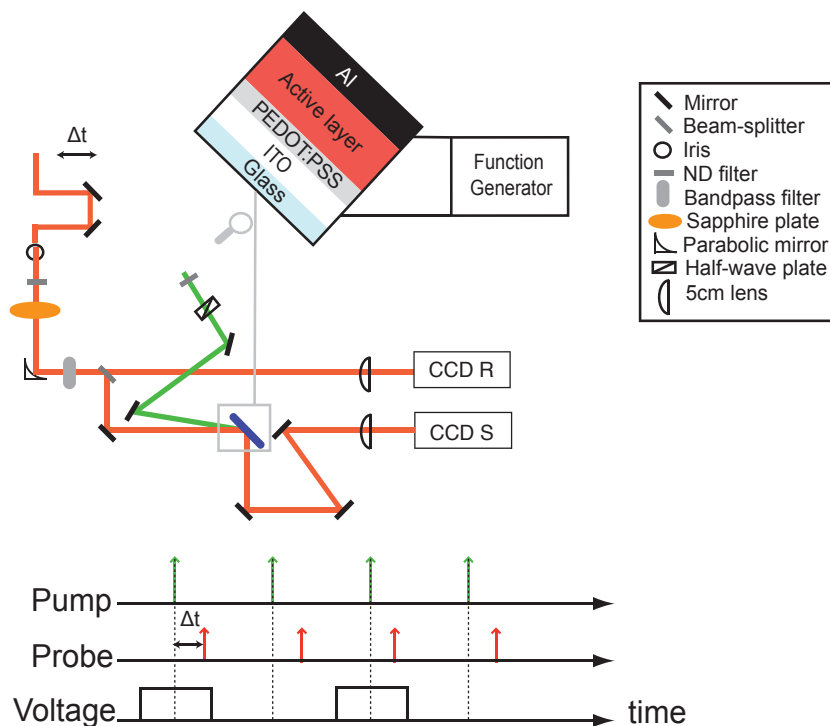
Figure 2.6 Scheme of the experimental setup for EDA measurements (not to scale). The lower part illustrates the synchronization of the pump and probe pulses, as well as the voltage pulse (modulated at 500 Hz). The green beam is the pump, while the orange beam is the white light continuum probe.

Entwicklungs-Büro Stresing, Berlin. A similar shot-by-shot detection scheme as for the TA spectroscopy was implemented. An oscilloscope (Tektronix TDS 3044 B) is used to measure the photocurrent on a 50 Ω load.

2.4 Data treatment

A Matlab procedure developed by N. Banerji has been implemented in the Photochemical Dynamics Group in order to correct for the group velocity dispersion and extract the corrected dynamics at different wavelengths, as well as the spectral profiles at different time delays.

2.4.1 Cross-correlation by Kerr gating

The time resolution of the setup is measured by estimating the cross-correlation of the pump and probe pulses at the sample position by the Kerr gating technique.[6] The probe and pulse beams have a polarization set at 45° with respect to each other in order to increase the non-linear Kerr effect. Both are focused onto a Kerr medium, which is either a SF10 window or a glass microscopic slide for measurements on solid state samples, alternatively a 1 mm cuvette filled with solvent for studies in solution. The probe then passes through a Glan-Thompson polarizer that blocks it entirely. When both pulses are temporally overlapped, the birefringence induced by the pump in the medium rotates the polarization of the probe, which is then able to pass through the polarizer and is detected by the CCD camera. The WLC has a broad spectral width and therefore presents a large group velocity dispersion. The longer wavelengths travel ahead, whereas shorter wavelengths are slower. This results in the blue being seen at time zero while the red has already travelled for a few picoseconds, as shown in Figure 2.7. This configuration of the setup has a typical cross-correlation (corresponding to its instrument response function, IRF) of the order of 130 fs for solid-state samples measured in inert controlled
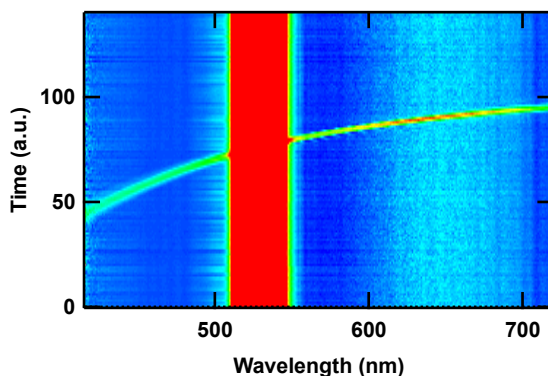

Figure 2.7 Graphical view of the wavelength dependence of the time delay in the probe continuum. Due to the chirp of the white light the temporal overlap between pump and probe – or time zero – is wavelength dependent. The temporal overlap of a certain component of the continuum with the pump pulse results in a coherent artifact.

atmosphere through a home-made chamber with quartz windows.

The chirp mathematical correction is routinely done for short time scales (typically less than 50 ps) and is performed by fitting every wavelength component by a Gaussian function, the width of each Gaussian providing the instrument response for each wavelength. The wavefront of all these Gaussian profiles can then be fitted with a monoexponential function as a function of time. Thus, the time zero for every wavelength is extracted from this function.

2.4.2 Background subtraction

A Matlab routine allows correcting the chirp but also subtracting the background spectra from the data. Typically, 20 to 30 spectra acquired before time zero are subtracted from the measurement in order to account for the spectral noise and for the pump beam up to a certain extent. Then, the corrected dynamics for different wavelengths and the spectral profiles at different time delays can be extracted from their initial matrix data file as data columns that are then treated separately in Igor Pro software.

2.4.3 Data analysis

In order to disentangle various photophysical processes occurring on the same time scale, a global analysis can be performed. For this, a multiexponential fit of the dynamics at different wavelengths is performed (eq. 2.20):

$$\Delta A = y_0 + A_1 e^{-\frac{t}{\tau_1}} + A_2 e^{-\frac{t}{\tau_2}} + A_3 e^{-\frac{t}{\tau_3}} \tag{2.20}$$

where τ_n is the time constant and A_n the amplitude associated to the process n. Typically, two or three exponentials are needed to fit correctly the dynamics

taken every 5-10 nm. In general this procedure gives enough insight to the transient signals obtained. The time constants τ_n were linked together for each analyzed sample, meaning each process could be separated via the different times τ_n obtained. The amplitudes were left free. When plotting the amplitude A_n spectra as a function of wavelength for each τ_n, we can follow the spectral regions that undergo similar dynamics. The offset y_0 was usually set to zero. The fitting was iterated until the standard deviation (2σ) for the time constants were 10 % or less, with more than 20'000 fit points.

This global fit enables to construct an associated spectra displaying the amplitudes, A_1, A_2 and A_3 of the transient signal related to each time component τ_1, τ_2, and τ_3, as a function of the wavelength. The signs of the amplitude and corresponding dynamics indicate whether the transient species is growing or decaying with time. If the signal is positive and the corresponding amplitude as well, the process probed is decaying to zero (by recombination for example). For the same signal, if the amplitude is negative, the transient species is still growing. For a negative signal, if the associated amplitude is negative, the transient species is decaying to zero. And at last, if the associated amplitude is positive, the negative signal is still growing, i.e. becoming even more negative (such as delayed SE for example). For more information about how to perform and analyze global analysis fittings, the reader is referred to van Stokkum et al.[17]

2.5 Nanosecond Flash Photolysis

2.5.1 Fundamentals of the technique

Ultrafast pump-probe measurements are restricted in time by the delay stage used to vary the optical time delay, and therefore by space and stability. Longer time scales, up to microseconds, are more adequately monitored by nanosecond flash photolysis. Actually, this technique was invented before

femtosecond lasers came up for which Eigen, Norrish and Porter won the Nobel Prize in chemistry in 1967.

A pump pulse excites the sample which is then probed by a continuous light beam, such as a xenon lamp. The transient signal is measured by a photo-multiplier tube or photodiode, and recorded by an oscilloscope. The time resolution is set by the Q-switched laser source (a few ns) and the detectors.

2.5.2 Experimental setup

Two experimental setups are available in our laboratories and have been used during this thesis. Both rely on a frequency tripled Q-switched Nd:YAG laser pumping an OPO at 355 nm (see section 2.1.4). The first one is a Continuum Powerlite 7030, while the second is from Ekspla NT-342. Both run at 20 Hz repetition rate and the output wavelength can be tuned between 450 and 650 nm for the Continuum, while the Ekspla offers excitation wavelengths going up to 2300 nm, and has a typical pulse duration of 4-7 ns FWHM. The pump beam is attenuated by grey filters depending on the fluence needed. The probe beam is constituted by the filtered output of a Xenon arc-lamp and is focused onto the sample. The signal is collected by a monochromator set at the proper probe wavelength. Depending on the probe wavelength, a photomultiplier tube (R9910 Hamamatsu) or an InGaAs photodiode (SM05PD5A, Throlabs) detects the transient signal, which is then recorded by an oscilloscope (Tektronix, DPO 7204 and DPO 7104C).

An acquisition is averaged over typically 3000 laser shots with dynamics recorded over 10'000 points. A sensitivity of 10^{-4} ΔA is typically obtained.

2.6 Sample and device preparation

The samples studied in this thesis were either made by the author or by collaborators. Sample preparation will be detailed in each chapter, as they are specific to the experimental technique used.

All solid samples were made in an argon or nitrogen glovebox. The glovebox in our laboratory was set up, improved and maintained during this work. For that, oxygen and water detectors were installed, as well as a supplementary charcoal part for capturing the solvents. A spin-coater (Laurell Technologies, Spinner Assy) was placed in the glovebox.

Evaporation of the metallic electrode was sometimes homemade with a Denton Benchtop Turbo vacuum thermal evaporator controlled by a quartz microbalance deposition controller (Inficon).

2.7 References

(1)   Maiman, T. H. *Nature* **1960**, *187*, 493–494.
(2)   Rullière, C. *Femtosecond laser pulses*; Springer, 2nd Ed., 2005.
(3)   Riedle, E.; Beutter, M.; Lochbrunner, S.; Piel, J.; Schenkl, S.; Spörlein, S.; Zinth, W. *Applied Physics B* **2000**, *71*, 457–465.
(4)   Pelet, S. Femtosecond Dynamics of Electron Transfer in the Photosensitization of Wide Band Gap Semiconductors, EPFL Thesis n°2626, 2002, pp. 1–140.
(5)   Wenger, B. Effect of electronic and nuclear factors on the dynamics of dye-to-semiconductor electron transfer, EPFL Thesis n°3447, 2006, pp. 1–184.
(6)   Teuscher, J. Dynamics of electron transfer processes at the surface of dye-sensitized mesoporous semiconductor films, EPFL Thesis n°4731, 2010, pp. 1–174.
(7)   Marchioro, A. Interfacial charge transfer dynamics in solid-state hybrid organic-inorganic solar cells, EPFL Thesis n°6221, 2014, pp. 1–176.
(8)   Huber, R.; Satzger, H.; Zinth, W.; Wachtveitl, J. *Optics communications* **2001**, *194*, 443–448.
(9)   Cappel, U. B.; Feldt, S. M.; Schöneboom, J.; Hagfeldt, A.; Boschloo, G. *J. Am. Chem. Soc* **2010**, *132*, 9096–9101.

(10) Lanzani, G. *The photophysics behind photovoltaics and photonics*; Wiley-VCH, 2012.

(11) Ardo, S.; Sun, Y.; Castellano, F. N.; Meyer, G. J. *J Phys Chem B* **2010**, *114*, 14596–14604.

(12) Gélinas, S.; Rao, A.; Kumar, A.; Smith, S. L.; Chin, A. W.; Clark, J.; van der Poll, T. S.; Bazan, G. C.; Friend, R. H. *Science* **2014**, *343*, 512–516.

(13) Bublitz, G. U.; Boxer, S. G. *Annu Rev Phys Chem* **1997**, *48*, 213–242.

(14) Amarasinghe Vithanage, D.; Devižis, A.; Abramavičius, V.; Infahsaeng, Y.; Abramavičius, D.; MacKenzie, R. C. I.; Keivanidis, P. E.; Yartsev, A.; Hertel, D.; Nelson, J.; Sundström, V.; Gulbinas, V. *Nat Comms* **2013**, *4*, 2334.

(15) Pranculis, V.; Infahsaeng, Y.; Tang, Z.; Devižis, A.; Vithanage, D. A.; Ponseca, C. S.; Inganäs, O.; Yartsev, A. P.; Gulbinas, V.; Sundström, V. *J. Am. Chem. Soc* **2014**, *136*, 11331–11338.

(16) Devižis, A.; Meerholz, K.; Hertel, D.; Gulbinas, V. *Phys. Rev. B* **2010**, *82*, 155204.

(17) van Stokkum, I. H. M.; Larsen, D. S.; van Grondelle, R. *Biochimica et Biophysica Acta (BBA) - Bioenergetics* **2004**, *1657*, 82–104.

Chapter 3

Photoinduced processes in cyanine dyes: from solution to solid-state and blends with PCBM
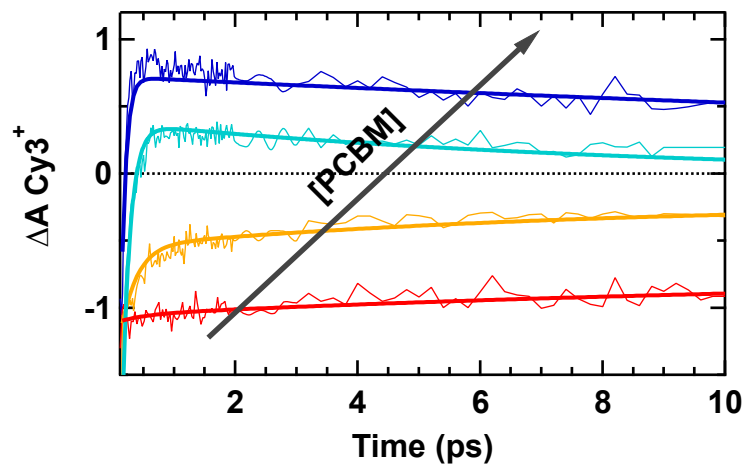
3.1 Introduction

Ultrafast optical techniques such as pump-probe spectroscopy give valuable insight into photophysical processes leading to charge generation and recombination in organic solar cells. Nevertheless, in order to understand them correctly, one needs to figure out where the transient species absorb, and how the different species overlap in time, as well in energy. In this Chapter, we will go through the spectral features observed upon Cy3 light absorption in solution, which will then be used for the studied Cy3-B, the cyanine with tetraphenylborate counter-anion in the solid state. This latter section is adapted from the following publication: "Ultrafast charge transfer in solid-state films of pristine cyanine borate films and blends with fullerene" by J. De Jonghe-Risse, J. Heier, F. Nüesch and J. -E. Moser, *Journal of Materials Chemistry A*, 3, 10935-10941, 2015.

3.2 Cyanine dye in solution

The photoinduced processes of cyanine dyes have been reported numerous times in the literature. They depend on the structure of the cyanine molecule, the aggregation (or dimerization), the environment and physical properties like temperature.[1-7] The 1,1'-diethyl-3,3,3',3'-tetramethylcarbocyanine (Cy3) molecular structure is shown in Figure 3.1. The counter-anion is abbreviated throughout the text by its first letter, such as P for hexafluorophosphate PF_6^-, C for perchlorate ClO_4^- and finally B for tetraphenylborate BPh_4^-. In order to restrict the number of parameters, the investigation is mainly focused on methanol solutions at room temperature, and at low concentrations in order to avoid aggregation.

3.2.1 Steady-state measurements

Let us first consider steady-state absorbance and fluorescence in solution. In dilute Cy3-C solutions (10^{-7} M), the vibronic structure of the first electronic transition displays absorbance peaks located at 470, 510 and 545 nm (Figure 3.1 a). The absorption spectrum is dependent on the solvent and a red-shift is observed for chlorobenzene (less polar solvent) with the absorbance peaks located at 480, 525 and 560 nm. No aggregation is observed at these low concentrations.

At equilibrium in solution, only the all-trans isomer of the cyanine dye Cy3-C monomer is present. This is inferred by the very similar shape of the excitation and absorption spectra in various solvents, as well as to the mirror image of the emission spectrum as compared to the absorption spectrum. (Figure 3.1 b). The
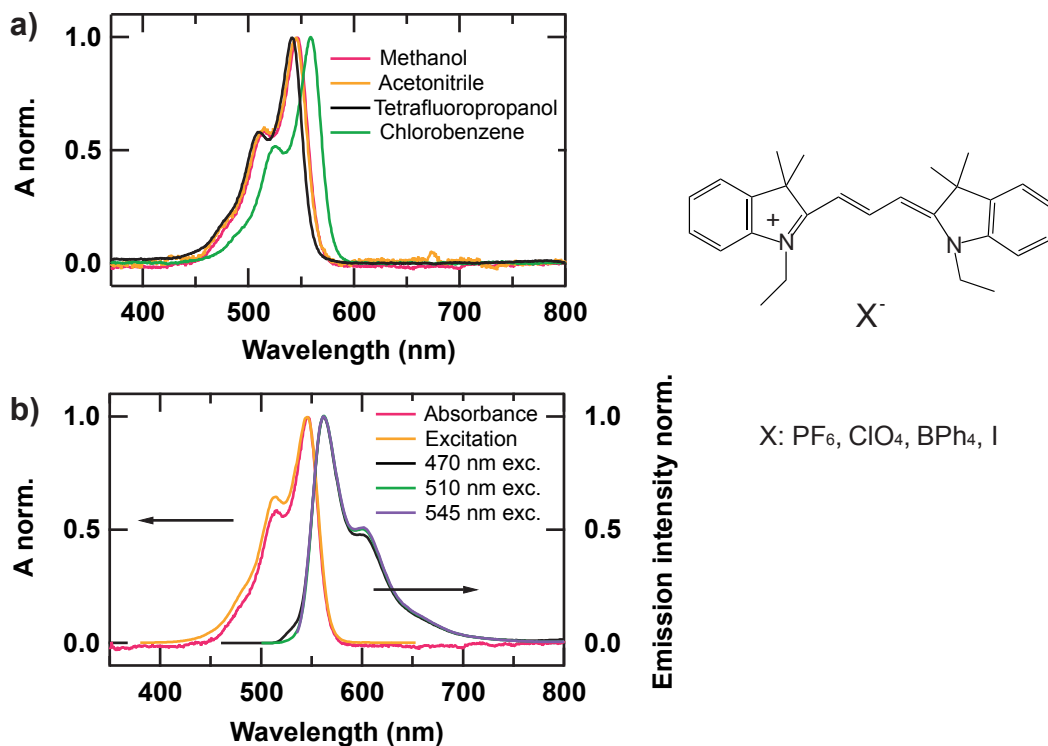

Figure 3.1 Normalized absorption spectra for 10^{-7} M Cy3-C a) in various solvents, b) in methanol, with fluorescence and excitation spectra. The fluorescence spectra do not depend on the excitation wavelength. The Cy3 molecular structure is shown on the right with various counter-anions.

emission is normalized for the absorption of the sample at the excitation wavelength. The shape of the emission spectra does not depend on the excitation wavelength, which is consistent with only one isomeric form (all- trans) existing in solution.[2] The spectral features do not change within four different solvents (acetonitrile, methanol, tetrafluoropropanol and chlorobenzene).

The counter-anion does not affect the steady-state absorbance spectra, as the absorption is due to π-π* transitions through the Cy3 polymethine chain. Increasing the length of the polymethine chain shifts the absorption spectra to the red.[8]

3.2.2 Transient absorption: from femtoseconds to microseconds

Transient absorption measurements were carried out in solution both on the femtosecond and nanosecond time scale. Figure 3.2 shows the transient absorption spectra (TAS) of the Cy3-C dye in methanol over a 200 fs to 1.2 ns timespan, together with the amplitude associated spectra resulting from a multiexponential global analysis. At first glance, the ground-state bleaching (GSB) and stimulated emission (SE) are observed between 500 and 700 nm, the same wavelengths characterizing ground-state absorption and fluorescence (see Figure 3.1 b). The maximum of the negative transient signal located at 550 nm at 200 fs is due to an overlap of both GSB and SE. The excited state absorption (ESA) is found at wavelengths below 490 nm and well in accordance with the one reported in the literature for Cy3-P.[2] The light absorbed upon laser excitation populates multiple excited states and the vibrationnally hot state likely relaxes to a lower lying excited state, as the growth of ESA and SE until 5 ps shows. This relaxation in the excited state is inferred by the amplitude spectrum associated with the 7.3 ps time constant: the negative amplitude below 490 nm and the positive amplitude for wavelengths above 540 nm with a shoulder at 610 nm both indicate a growing lowest excited state absorption. Moreover, the
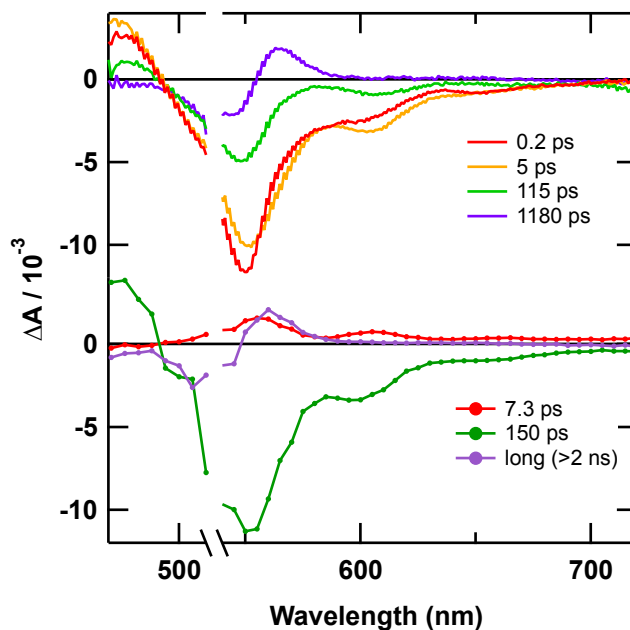
Figure 3.2 Transient absorption spectra at various time delays after 530 nm excitation for Cy3-C in methanol solution at 10^{-5} M. The lower graph is the amplitude spectra associated to the time constants resulting from the multiexponential global analysis.

absence of GSB decay on the same timescale confirms the lack of excited state deactivation.

All transient signals decay with the 150 ps time constant, which is similar to the fluorescence lifetime measured for various other cyanine dyes.[9,10] At longer time delays, a positive transient absorption signal appears at 565 nm. As reported by Chatterjee et al., this photoabsorption is due to the *cis*-isomer (excited state) resulting from the rotation around one conjugated carbon-carbon bond of the Cy3 polymethine chain (trans-cis isomerization).[2]

A deeper insight into the photoisomerization in solution is given by investigating the longer time delays with nanosecond flash photolysis. Results are shown in Figure 3.3. No signal is observed in the blue part of the spectrum below 500 nm, as the singlet excited state decays on the picosecond (ps) time scale. The positive signal due to the *cis*-isomer is still present around 550 nm. In addition, another photobsorption appears at longer wavelengths centered at 580 nm. It decays on a faster time scale than the *cis*-isomer, and is assigned to the triplet state as

reported by Jia et al.[7] The triplet quantum yield is rather poor for cyanine dyes ($\Phi < 0.05$), and the triplet-triplet absorption has a low extinction coefficient, making it difficult to observe.[11] With the addition of CH_3I in a degassed methanol solution, the triplet yield is increased due to the heavy-atom effect, and an increase in the photoabsorption at 580 nm is indeed observed (Figure 3.3). As a matter of fact, both signals at 550 and 580 nm are a mixture of *cis*-isomer and triplet state absorptions .

The signal at 580 nm is fitted with a biexponential, and the results are shown in Table 1. The amplitude of the fast component decaying with 3 μs time scale is increased in the presence of CH_3I from 88.6 % to 94.4 %, whereas the amplitude associated with the slow component (i.e. *cis*-isomer) decreases upon CH_3I addition from 11.4 % to 5.6 % (Table 1).
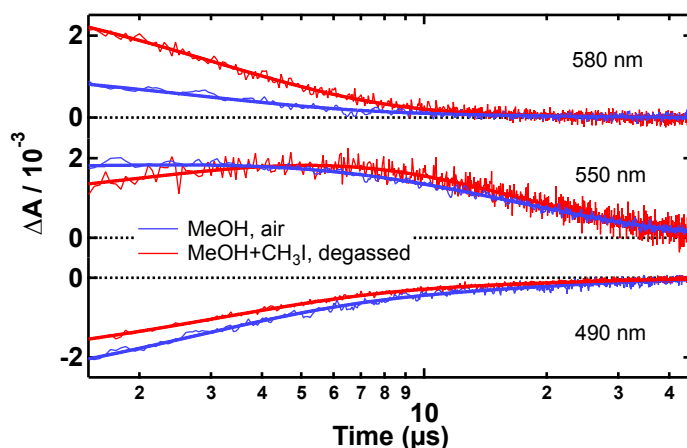

Figure 3.3 Dynamics recorded at various probe wavelengths after 530 nm excitation for two different Cy3-C solutions (10^{-5} M). The solid lines are the best fit of experimental data points.

Table 1 Amplitudes, time constants and ratio of amplitudes as from data of Figure 3.3.

		A1	τ1 (μs)	A2	τ2 (μs)	% A1	%A2
MeOH, in air		1.21	2.5	0.155	16.3	88.6	11.4
MeOH+CH₃I degassed	(1:8)	3.33	3.0	0.197	14.9	94.4	5.6

It is also known that Cy3-I, the same cyanine with iodide as a counter-anion, shows no singlet excited state at 35 ps after excitation but rather a triplet excited state with nanosecond lifetime absorbing around 620 nm, again due to the heavy-atom effect and subsequent intersystem crossing.[3] In the case of borate counter-anions, it has been shown that electron transfer from the borate to the excited state of the cyanine (reductive quenching) leads to a reduced cyanine species, which absorption is centered at a wavelength of 430 nm.[1,2] Alkyl-substituted borates undergo a carbon-boron bond cleavage upon oxidation, generally resulting in unstable product radicals. However, in the case of tetraphenylborate, which is a good electron donor,[12,13] back-electron transfer from the reduced cyanine species is apparently sufficiently fast to regenerate the dye borate and prevent its decomposition.

All photophysical processes described here depend on the solvent: timescales as well as spectral positions in energy (wavelength) are affected by the polarity and viscosity of the solvents.[7,14] Nevertheless with these results, we now have a clear picture of the photophysical processes occurring in Cy3 solutions, and have reviewed the importance of their counter-anions with respect to the isomerization, intersystem crossing and intra ion-pair electron transfer. As our aim is to understand how charges are generated in cyanine based solar cells, solid-state samples were investigated. Let us now get through the photochemistry of cyanine borates Cy3-B. Cy3-P will be considered in Chapter 4.

3.3 Cyanine Borates in the solid-state: intra ion-pair reductive quenching and oxidative quenching by PCBM

Counter-anion migration under applied electric fields in solid-state cyanine layers has been observed and could be detrimental for small molecule solar cell applications, as the charges building up at the electrode interface would hinder charge extraction.[6,15] In order to restrict ion migration, larger counter-anions can be used such as borate and trisphat.[16] As mentioned in the previous section, the Cy3 with tetraphenylborate counter-anion (Cy3-B) can undergo intra ion-pair reductive quenching. The photophysical processes for the cyanine tetraphenylborate salt that undergoes intra ion-pair electron transfer under light irradiation are shown in Figure 3.4 b (process 2). By adding an electron acceptor such as the fullerene [6,6]- phenyl C_{61}-butyric acid methyl ester (PCBM), kinetic competition between electron transfer to PCBM (process 1) and reductive quenching by tetraphenylborate (process 2) is expected. Here we report transient absorption studies on solid-state pristine cyanine tetraphenylborate and various blends with PCBM. From the photoexcited Cy3, the kinetic competition between the reductive quenching by the tetraphenylborate moiety and the oxidative quenching by PCBM was monitored. Different blend ratios enabled to alter the yield of Cy3 oxidized species and indicate that intermixed phases are crucial for charge generation.

The normalized absorption spectra of the pristine Cy3-B and bulk heterojunction blends with PCBM thin films are shown in Figure 3.4 a. The pristine Cy3-B ground state absorbs from about 450-600 nm and displays the monomer absorption maximum at 570 nm. This spectrum is similar to that of the ground state of the Cy3 cyanine dye with PF_6^- as a counter-anion (Cy3-P).[17] It is red shifted and broadened compared to the absorption spectrum measured in

solution (Figure 3.1 a). Hypsochromically shifted features are attributed to dimer and H-aggregate absorption (shoulder around 500 nm). Remarkably, this small amount of aggregated dye does not seem to increase in the presence of PCBM. Absorption of PCBM is quite weak in the visible but increases in the UV region, causing a slight blue shift of the apparent Cy3-B absorption maximum when blended with PCBM.
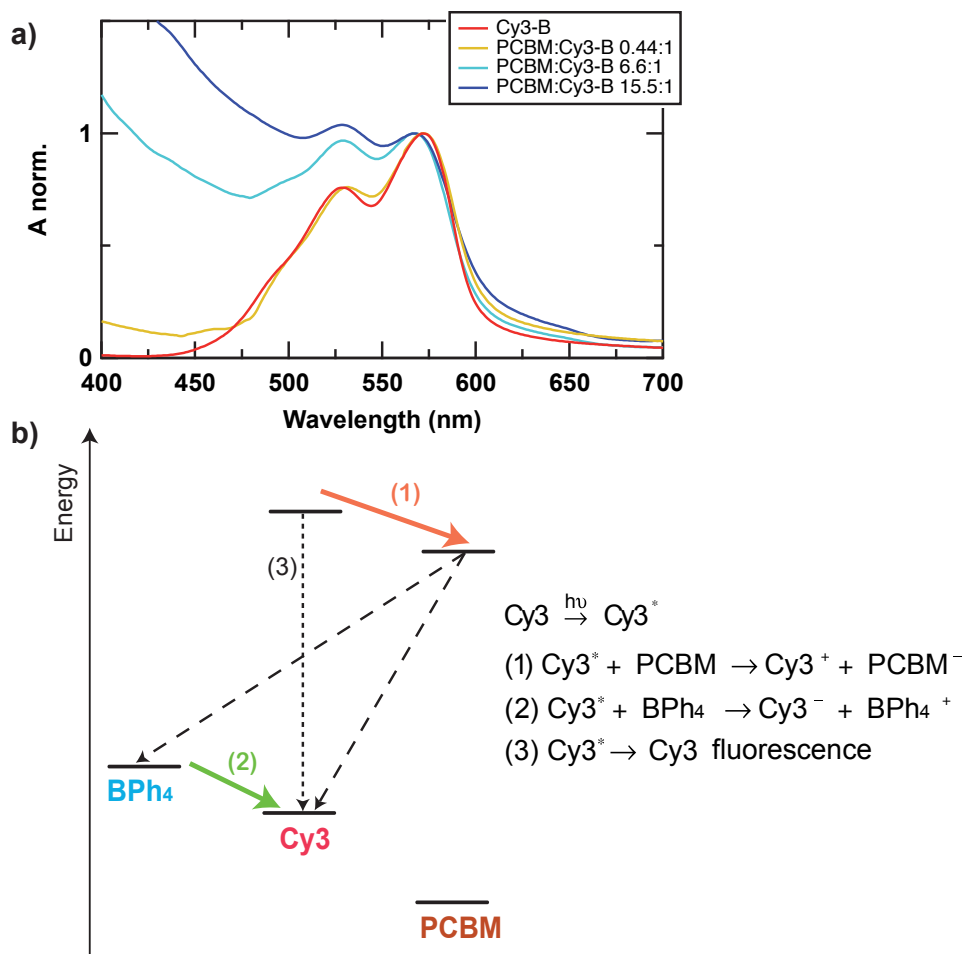

Figure 3.4 Normalized steady-state absorption spectra for solid-state Cy3-B and various blends with PCBM. The scheme on the right represents the energy levels and electron transfer processes in Cy3-B and blends with PCBM after Cy3 excitation. (1) is electron transfer to PCBM, (2) is the reductive quenching by the borate counter-anion. Back-electron transfer and recombination are shown in dotted lines.

3.3.1 Pristine Cy3-B

For clarity of the discussion, transient absorption results for the pristine Cy3-B are presented first. A large negative band located at 550-680 nm is readily observed upon pulsed excitation (Figure 3.5) and is attributed to the Cy3 ground-state bleaching (GSB) due to the similarity with steady-state absorbance (Figure 3.4 a). At early time delays, the negative maximum at 580 nm is an overlap of the GSB and a weak stimulated emission signal (SE) and is therefore blue-shifted to 570 nm as the SE vanishes. The positive transient absorption band located at 420-500 nm is assigned to the singlet excited state absorption (ESA) on the first tenths of picoseconds, as already observed by Chatterjee et al. from time-resolved flash photolysis studies on Cy3-P.[1,18] This photoabsorption compensates the GSB (negative signal) below 550 nm. The fast quenching of the cyanine ESA by the tetraphenylborate counter-anion leads to the formation of a cyanine reduced species absorbing at about 420-470 nm and oxidized tetraphenylborate. This reductive quenching has been observed in solution.[2] In thin solid films, a
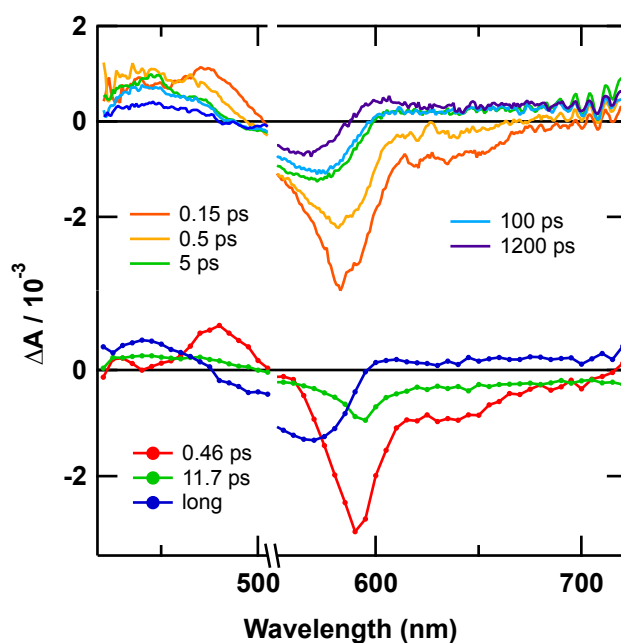

Figure 3.5 Transient absorption spectra at various time delays after 530 nm excitation for neat Cy3-B. The bottom graph shows the amplitude spectra associated to the time constants resulting from the multiexponential global analysis for neat Cy3-B.

red shift and a broadening of the absorption spectra compared to the same species in solution is commonly observed for molecules, which explains a maximum absorption peak for the cyanine reduced species located at 420-470 nm in the neat film compared to 430 nm in solution.

The associated spectra resulting from a multiexponential global fitting procedure are shown in Figure 3.5 and clearly demonstrate the mechanism of reductive quenching.

The decay of the red part of the ESA between 460-500 nm is associated with a 0.46 ps time constant and is mirrored by the decay of the SE at about 590-680 nm. As the GSB does not decay on this time scale, it is reasonable to assume that not all the singlet excited state fully returns to the ground state, and this will be confirmed below. Looking more specifically at the positive transient feature located at 420-460 nm, assigned to both the ESA and the cyanine reduced species, it is clear that the ESA is converted into the cyanine reduced species partly with 0.46 ps. The reductive quenching of the excited state by the tetraphenylborate counter-anion is more clearly evidenced by the isosbestic point located at 460 nm (Figure 3.5) between the ESA and the reduced cyanine species. The latter still grows with a 11.7 ps time constant and displays a lifetime that is longer than the 1 ns optical time delay of our femtosecond setup. Application of nanosecond flash photolysis measurements to identical samples
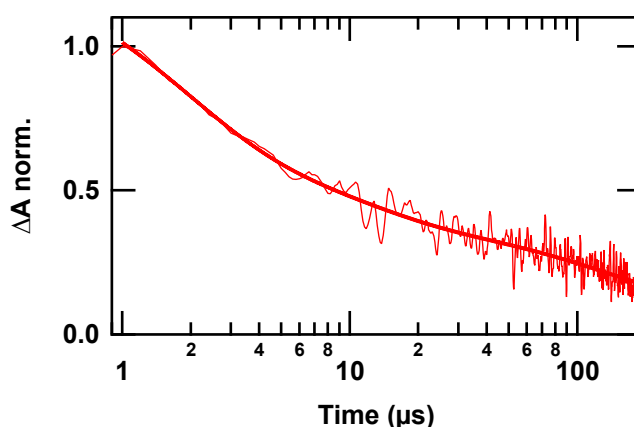

Figure 3.6 Dynamics recorded at 450 nm probe after 530 nm ns pulsed excitation for pristine Cy3-B solid-state film. The solid line is the best multiexponential fit of experimental data points.

(Figure 3.6) confirmed the formation of long-lived reduced cyanine species, whose decay by back electron transfer takes place in the microsecond time scale. Complete regeneration of the dye was achieved within 200 μs, which is then compatible with the 1000 Hz repetition rate of ultrafast transient absorption experiments.

3.3.2 Blends with PCBM

The morphology of PCBM:Cy3-B bulk heterojunction blend films depends on the PCBM loading and shows a qualitatively similar behavior as PCBM:Cy7-trisphat blend films which have been described by Heier et al.[19] With the largest PCBM loading (15.5:1), films display only one fully intermixed phase, while lower PCBM amounts lead to both intermixed and a pure cyanine phases segregating at the surface. In the latter case, phase contrast AFM images reveal a spinodal phase pattern (i.e. demixing of Cy3-B and PCBM) at the surface (Figure 3.7 a). Dipping samples into tetrafluoropropanol selectively dissolves the pure dye phase. Remaining films contain intermixed Cy3-B with PCBM, none of the materials being selectively dissolved anymore. The topography reflects the inverse structure of the dye surface domains (Figure 3.7 b). The different morphologies for different compositions can be explained with an asymmetry in the PCBM/dye/solvent ternary phase diagram and the nature of film formation during a solvent quench (Figure 3.7 c).[19] At high PCBM loadings the system remains in the one-phase region (fully intermixed) for all solvent concentrations. For lower PCBM loadings, solvent evaporation brings the system into a two-phase region. It is however unclear how molecular intercalation of PCBM in the cyanine tetraphenylborate ion-pair occurs in the intermixed phase.
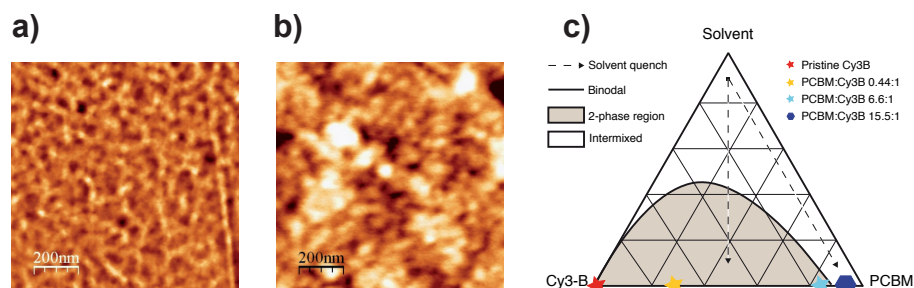
Figure 3.7 AFM images of a 1:1 PCBM:Cy3-B blend a) phase contrast upon spin coating, and b) topography after dipping the sample in TFP. The schematic phase diagram of PCBM:Cy3-B blends is shown in c). Upon solvent evaporation, the blend will either be fully intermixed (high PCBM concentrations) or segregate into two phases (low dye concentrations).

The lower the PCBM loading, the largest the pure cyanine layer. The close distance between Cy3 and PCBM in the intermixed phase leads to a direct competition between electron transfer to PCBM (Figure 3.4, process 1) and reductive quenching by the tetraphenylborate counter-anion (Figure 3.4, process 2) following light absorption by Cy3. As a pure Cy3-B phase exists in all blends except in the 15.5:1 blend, a transient photoabsorption signal corresponding to the cyanine reduced species obtained by reductive quenching is expected. Direct light absorption by PCBM can be neglected for blends with a low PCBM fraction (0.44:1) but higher PCBM fractions lead to about 20% of light absorption by PCBM alone at 530 nm excitation (Figure 3.4 a). However, the ground-, excited-, and reduced states of PCBM have rather low extinction coefficients and are, therefore, not responsible for the majority of the transient absorption signals observed in the probed spectral range.[25] Oxidation of Cy3 upon hole transfer from photoexcited PCBM molecules, however, cannot be excluded.

The effect of the addition of PCBM on the dynamics observed at a probe wavelength of 440 nm, where both the Cy3 excited state and reduced species absorb, is shown in Figure 3.8 a. For all blends, the initial amplitude of the photoabsorption is reduced compared to that of the pristine Cy3-B. This suggests that ultrafast quenching of the Cy3 excited state by PCBM is taking place,

successfully competing with the reductive quenching by tetraphenylborate and inhibiting the formation of the Cy3 reduced state.

The dynamics recorded at 550 nm shown in Figure 3.8 b are assigned to both the GSB of the cyanine and to the cyanine oxidized species formed in blends.[20] At this wavelength a local minimum is observed in the Cy3 ground state absorption spectrum (see Figure 3.4), which enables scrutinizing the formation of cyanine oxidized species. At high PCBM loadings, photoabsorption of the cyanine oxidized species is directly observed. The amplitude of the positive signal gradually increases with the PCBM content, indicating a higher amount of the oxidized species formed. The dynamics of cyanine oxidized state formation is extremely fast and could not be entirely resolved by our ultrafast setup. The time constant for Cy3 oxidized state formation yielded by the fitting procedure is, therefore, certainly overestimated. The amplitude values for the high PCBM
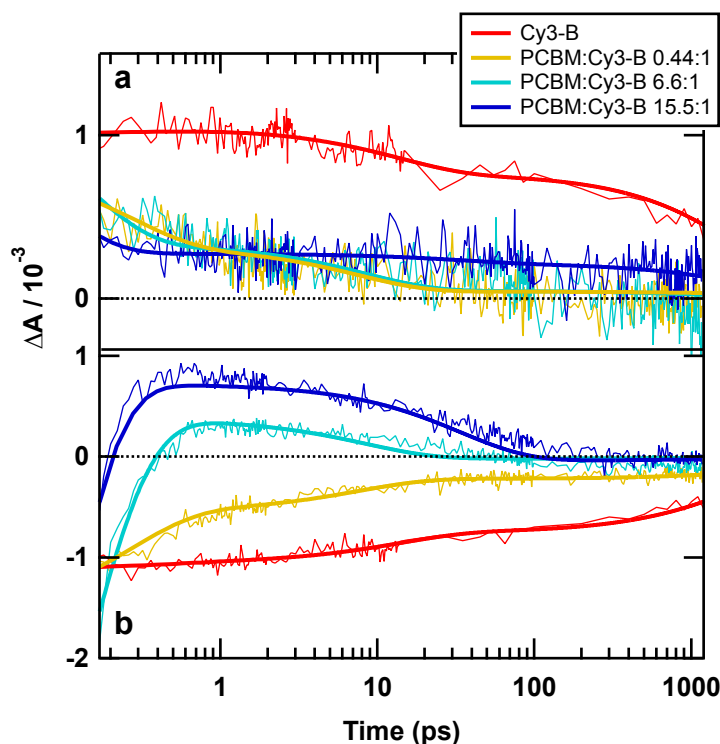

Figure 3.8 Dynamics recorded at a) 440 nm (Cy3 excited and reduced state) and b) 550 nm probe wavelengths (Cy3 GSB and oxidized state) after 530 nm excitation for pristine Cy3-B and various PCBM loadings. Fluence: 45 μJ/cm^2. The solid lines represent the result of the best multiexponential fit.

content blends (6.6:1 and 15.5:1) can not be compared quantitatively as absorption by PCBM can not be excluded. This explains the similar amplitudes measured at a wavelength of 440 nm for the 0.44:1 and 6.6:1 blends (Figure 3.8 a). Signal amplitudes can be compared only for pristine Cy3-B and the 0.44:1 blend.

The fits shown in Figure 3.8 result from a global analysis of multiwavelength kinetic data. Figure 3.9 presents the transient absorption spectra for the blends together with the associated amplitude spectra (amplitudes associated to the three time constants) for the photophysical processes observed in pristine Cy3-B and blends with PCBM as depicted in Figure 3.4. The fluence of 45 $\mu J/cm^2$ was chosen as no intensity effect was observed (not shown) and a satisfying signal-to-noise ratio was obtained.

The first two associated time constants for the blends are shown in Table 2, the longer being outside of the time window allowed by our femtosecond setup (> 1 ns). The shortest time constant (Figure 3.9 d and Table 2) is associated to the Cy3 excited state quenching and the concomitant growth of either the oxidized or the reduced cyanine species absorptions upon electron transfer (process 1) or reductive quenching (process 2), respectively. A large negative amplitude located between 500-600 nm is observed for all blends (Figure 3.9 d), which increases with increasing PCBM relative content and is directly related to the ultrafast formation of the cyanine oxidized species. When PCBM is added, the SE gradually disappears (Figure 3.9 a-c), but Cy3 ESA spanning over a wide range of wavelengths (420-500 nm) is still observed at early time delays. This indicates that ultrafast electron transfer to PCBM occurs from the cyanine emissive photoexcited state. For pure Cy3-B in either pristine Cy3-B dye films or in the segregated phase from blends, the cyanine reduced species, which absorbs around 420-470 nm, starts growing on a similar time scale. As a result, no decaying amplitude associated to the first time scale is observed at the blue side of the ESA. The intermediate timescale, shown in Figure 3.9 e, reveals the presence of reduced dye species (absorption in the region 420-460 nm) for all samples, except the one containing the highest PCBM load (15.5:1). This is an

expected result, as this is the only sample where both Cy3-B and PCBM are fully intermixed, thus resulting in a fast electron transfer to the fullerene competing successfully against the reductive quenching by tetraphenylborate. The oxidized state's lifetime is associated to the intermediate time constant (Figure 3.9 e, picoseconds) whereas the reduced species lives for several microseconds (Figure 3.6, 3.9 f and Table 2).

Film composition	Cy3* quenching time constants	Oxidized/Reduced species lifetime
Pristine Cy3-B	462.1 fs ± 17.7 (52 %),11.7 ± 1.4 ps (48%)	Red. Cy3: 10^{-4} s
PCBM:Cy3-B 0.44:1	261.1 fs ± 4.4	Ox.Cy3: 10^{-10} s
PCBM:Cy3-B 6.6:1	132.0 fs ± 1.7	Ox. Cy3: 10^{-10} s
PCBM:Cy3-B 15.5:1	77.5 fs ± 2.1	Ox. Cy3: 10^{-10} s

Table 2 Time constants for Cy3 excited state quenching and approximate lifetimes (order of magnitude) of oxidized/reduced species in films of various compositions.

In solution, reductive quenching of C_{60} triplet photoexcited state by a tetraphenylborate anion has been observed to yield the C_{60} anion.[12] The PCBM anion absorbs around 1030 nm, outside of the spectral range covered by our setup.[21] Moreover, intersystem crossing to the triplet state of PCBM is rather improbable in thin films, as other deactivation pathways become possible due to the close packing of fullerene molecules.[22]

The positive amplitude of the absorption change observed at longer wavelengths for 15.5:1 and 6.6:1 blends (Figure 3.9 b,c,e) could be due to PCBM ESA, although only 20% of the incoming light is absorbed by fullerene molecules. We are currently investigating the origin of this effect. Among various hypotheses, we could speculate that this photoabsorption originates from charge transfer states formed between cyanine and PCBM neighboring molecules.[23] Photoinduced Stark effect is excluded here, as the Stark shift observed elsewhere for Cy3-P is quite weak, and the one arising from PCBM typically displays narrow features, which do not appear here (see Chapter 4, Figure 4.13 a).[24,25] While the yield of electron transfer from Cy3 to the fullerene clearly increases with the acceptor's concentration (Figure 3.8 b), its rate also appears to depend

upon the PCBM molar ratio. Time constants measured for the cyanine excited state quenching are reported in Table 2. From the pure Cy3-B sample, we can conclude that the reductive quenching happens in a few picoseconds (0.46 and 11.7 ps time constants). In the intermixed phase of blends, the cyanine oxidized species appears on time scales decreasing with the average distance between Cy3 and PCBM molecules, reaching 77.5 fs for the 15.5:1 blend. As explained earlier in the text, the fit obtained for this sample probably overestimates the time-constant (Figure 3.8 b), whose actual value must probably be shorter than 50 fs.
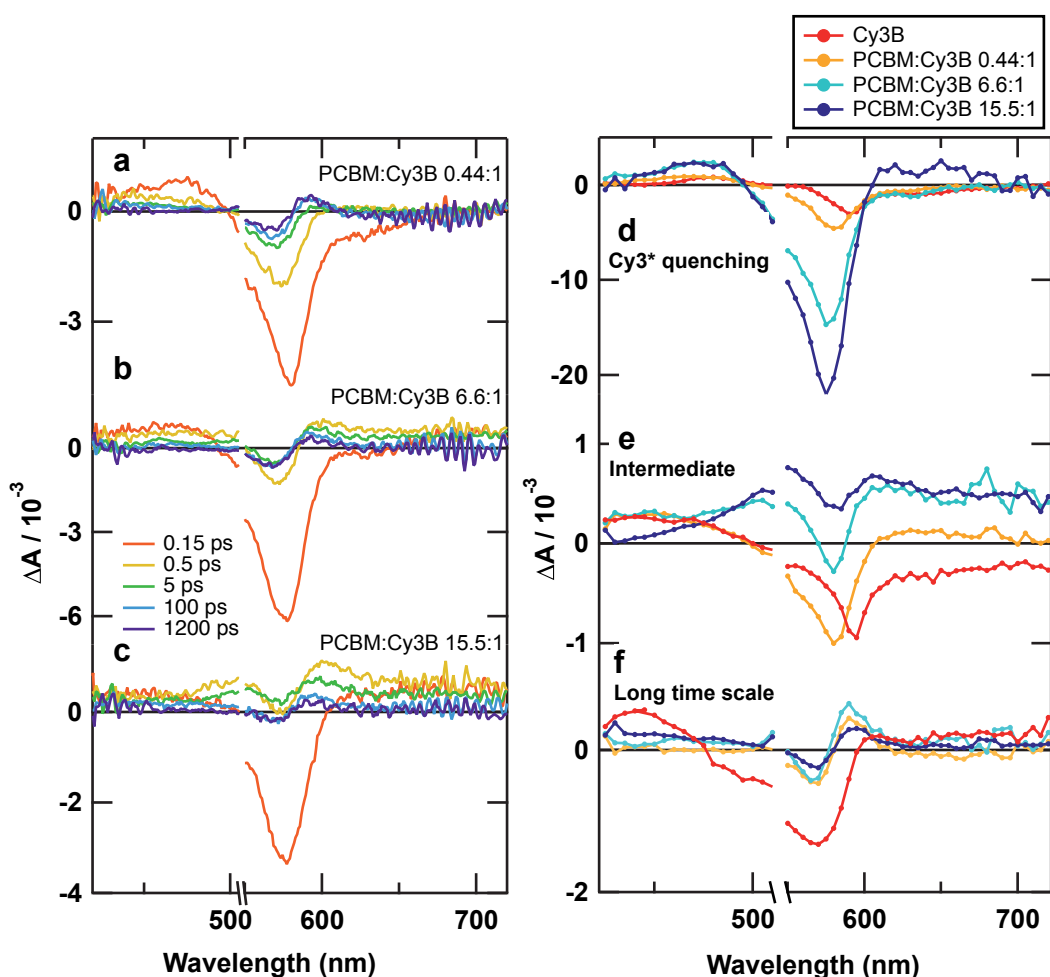

Figure 3.9 a-c) Transient absorption spectra at various time delays after 530 nm excitation for the various PCBM:Cy3B blends. d-e) Associated amplitude spectra resulting from the multiexponential global analysis for the various investigated samples. d) is the excited state quenching, e) is the intermediate time scale (order of ps) and f) is the long time scale (> 1 ns). Time scales associated to Figures d and e are reported in Table 2.

The cyanine oxidized state lifetime does not exceed a few tenths of picoseconds as evidenced in Figure 3.8 b. Figure 3.9 f showing the long time component corroborates this as no transient signal assigned to the cyanine oxidized species around 550 nm is observed. Hole transfer from photoexcited PCBM in the 6.6:1 and 15.5:1 blends is not ruled out, and could also be responsible for a faster appearance of Cy3 oxidized state. The 0.44:1 blend still shows a faster Cy3 excited state quenching than pristine Cy3-B, whereas in this sample the absorption by PCBM is negligible. It is therefore clear that electron transfer from photoexcited Cy3 to PCBM is faster than the reductive quenching by tetraphenylborate, and that hole injection from photoexcited PCBM to Cy3 could be even faster.

It is likely that the reductive quenching by tetraphenylborate counter-anion of the Cy3 oxidized species obtained after Cy3 electron transfer to PCBM is also responsible for the decay of the Cy3 oxidized species photoabsorption. We expect that applying a voltage to the blend solar cell devices would prevent the unwanted charge recombination from the PCBM anion.

3.3.3 Isomerization in the solid state

It is speculated that Cy3 isomerization is responsible for the positive transient absorption feature located at 600 nm observed at long time scales in blends only (Figure 3.9 f). It is not observed in pristine Cy3-B, which leads to the hypothesis that the isomerization, which is a rather slow process (ns), occurs in the intermixed phase. Probably the ion pair with tetraphenylborate is too closely packed, resulting in inevitable reductive quenching upon light absorption by Cy3 in pure Cy3-B layers, as this process is faster (ps). Pristine Cy3-P films and bilayers with C_{60} both also show signs of isomerization in the solid state (see Figures 4.4 and 4.6 in Chapter 4). In bilayers, the process probably occurs in excitons created in Cy3 molecules that are unable to reach the C_{60} interface. Isomerization of the Cy3 dye has been observed in this work in solution (section

3.2.1) and reported in the literature.[2] In the solid-state, although the conformational change between the all-trans and *cis* state is inhibited due to film rigidity, the process has been observed in solid-state squaraines.[26] De Miguel et al. indeed reported a sub-ns isomerization, which transient photoabsorption is located at red-shifted wavelengths compared to the trans state, with back-isomerization occurring with a time constant of about 30 ns. Moreover, it has been shown that the addition of glycerol to methanol solution of cyanine dyes slows down the isomerization, but does not inhibit it.[27]

3.4 Conclusions

Results shown in this chapter depict the photoinduced processes of the cyanine dye Cy3. Investigations in solution enabled to scrutinize the transient absorption spectra of pure Cy3-C: ground state, singlet excited state, emission, *cis*-isomer and triplet excited state. These results are consistent with those reported in the literature and give more insight into the ultrafast dynamics (<10 ps), which have not been reported before. Upon excitation, the singlet excited state is formed, and vibrational relaxation occurs in less than 10 ps to the lowest level of the singlet excited state. Stimulated emission and excited state absorption are observed instantaneously and decaying with 150 ps time constant. The photo-isomerization occurs on less than 1 ns and decays after several μs. The triplet excited state has been observed by nanosecond flash photolysis upon addition of iodomethane (CH_3I), enhancing the intersystem crossing due to the heavy-atom effect.

In the second part of this chapter, we have shown that cyanine tetraphenylborate Cy3-B undergoes intra-ion pair reductive quenching in the solid state. The picosecond time scale for electron transfer from the tetraphenylborate moiety to the excited Cy3 suggested from the global analysis is in accordance with previous findings in solution.[2] No evidence for tetraphenylborate radical due to

carbon-boron bond cleavage has been noticed as the cyanine reduced species absorbing at 420-450 nm recombines with the oxidized tetraphenylborate on the microsecond time scale. The widely used PCBM electron acceptor was blended with Cy3-B with different ratios and we found that the phase morphology drives charge injection in PCBM. High PCBM loadings consist of a fully intermixed phase where upon Cy3 excitation, oxidized Cy3 is observed on ultrashort time scales (< 160 fs). Low PCBM loadings lead to an intermixed phase and a pure Cy3-B segregated phase, therefore enabling the observation of both reduced and oxidized Cy3 species. Finally, we have shown that isomerization can occur in the solid-state, although more investigations, such as low temperature measurements, could give more insight into this process.

3.5 Methods

Materials

The cyanine dye 1,1'-diethyl-3,3,3',3'-tetramethylcarbocyanine perchlorate (Cy3-C) was synthesized in the laboratory of Functional Polymers, EMPA.[28] It was dissolved in methanol (Acros, 99.8 %, ACS reagent), tetrafluoropropanol (Synthon), acetonitrile (Acros, 99.9 %) and chlorobenzene (Acros, 99.6 %, ACS reagent). Iodomethane (Fluka, 99 %) was added to methanol solutions.

The cyanine dye 1,1'-diethyl-3,3,3',3'-tetramethylcarbocyanine tetraphenylborate (Cy3-B) was purchased from FEW chemicals, Germany. [6,6]-phenyl C_{61}-butyric acid methyl ester (PCBM) was purchased from Solenne B.V., The Netherlands. Both Cy3-B and PCBM were dissolved at various concentrations in chlorobenzene purchased from Sigma-Aldrich. The films were fabricated by spin coating the blend solutions (molecular weight ratio) from chlorobenzene onto glass substrates. The glass substrates were cleaned with a brush in Hellmanex, and then sequentially sonicated in acetone and ethanol baths. Finally, they were placed in a plasma cleaner (in air) for 15 minutes. All

the samples were made in a nitrogen glovebox, and all chemicals were used directly without further purification.

Steady-state

Absorption and excitation spectra were recorded on a Perkin-Elmer Lambda 950 spectrophotometer. Spectra were baseline-corrected and measured with a reference beam. Fluorescence spectra were recorded on a LS-50 from Perkin Elmer.

Transient absorption spectroscopy

Transient absorption spectra were recorded via femtosecond pump-probe spectroscopy based on the 778 nm output of an amplified Ti-sapphire laser (Clark-MXR, CPA-2001) with 150 fs pulses running at 1 kHz repetition rate. The pump beam was generated via a two-stage non-collinear optical parametric amplifier (NOPA), while the probe beam was a white light continuum (420-720 nm) generated by a portion of the 778 nm passing through a sapphire plate. The pump wavelength was set at 530 nm and the fluence at the sample was 45 $\mu J/cm^2$ for solid-state samples, whereas it was about 180 $\mu J/cm^2$ for Cy3 solutions. No fluence dependence on the dynamics was observed in either cases. The probe beam was split before the sample into a signal and reference beam in order to account for intensity fluctuations. Both beams were recorded shot by shot with a pair of 163 mm spectrographs (Andor Technology, SR163) equipped with a 512 x 58 pixels back-thinned CCD (Hamamatsu S07030-0906).

All spectra were corrected for the white-light chirp measured by Kerr gating and background noise. Global analysis by a multiexponential fit at different wavelengths (typically every 5 nm) enabled the dissociation of the various photophysical processes occurring. The associated spectra show the amplitude of the transient signal related to each time component.

Nanosecond flash photolysis

Microsecond timescale dynamics were recorded using a frequency-tripled Q-switched Nd:YAG laser (Ekspla NT-342) running at 20 Hz repetition rate. An optical parametric oscillator was used to generate 530 nm wavelength pump pulses (5 ns FWHM) with a fluence at the sample of 60 μJ/cm^2. The continuous-wave probe light from a xenon lamp was transmitted through the sample, various optics, and a grating monochromator before being detected by a fast photomultiplier tube. Transient signals were recorded by a digital oscilloscope Tektronix DPO 7104C. Averaging over typically 3000 shots yielded a satisfactory signal-to-noise ratio. A second-order Savitsky-Golay smoothing algorithm was applied (35 points).

Samples for time-resolved spectroscopy

Solid-state samples were analyzed in an argon water-free environment with a home-built chamber avoiding contact with ambient air (Quartz windows, UQG Optics). For femtosecond transient absorption, solutions were continuously bubbled under argon, in a 1 mm cuvette. For nanosecond flash photolysis, solutions were degassed prior to the measurement in 1 cm quartz cuvettes and maintained in argon atmosphere thanks to an argon overpressure provided by a balloon.

3.6 References

(1)   Chatterjee, S.; Gottschalk, P.; Davis, P. D.; Schuster, G. B. *J. Am. Chem. Soc* **1988**, *110*, 2326–2328.

(2)   Chatterjee, S.; Davis, P. D.; Gottschalk, P.; Kurz, M. E.; Sauerwein, B.; Yang, X.; Schuster, G. B. *J. Am. Chem. Soc* **1990**, *112*, 6329–6338.

(3)   Sauerwein, B.; Schuster, G. B. *The Journal of Physical Chemistry* **1991**, *95*, 1903–1906.

(4)   Yang, X.; Zaitsev, A.; Sauerwein, B.; Murphy, S.; Schuster, G. B. *J. Am. Chem. Soc* **1992**, *114*, 793–794.

(5)   Murphy, S.; Sauerwein, B.; Drickamer, H. G.; Schuster, G. B. *The Journal of Physical Chemistry* **1994**, *98*, 13476–13480.

(6)   Chibisov, A. K. *High Energy Chem* **2007**, *41*, 200–209.

(7)   Jia, K.; Wan, Y.; Xia, A.; Li, S.; Gong, F.; Yang, G. *J. Phys. Chem. A* **2007**, *111*, 1593–1597.

(8)   Hany, R.; Fan, B.; de Castro, F. A.; Heier, J.; Kylberg, W.; Nüesch, F. *Prog. Photovolt: Res. Appl.* **2011**, *19*, 851–857.

(9)   Levitus, M.; Ranjit, S. *Q. Rev. Biophys.* **2011**, *44*, 123–151.

(10)   Sanborn, M. E.; Connolly, B. K.; Gurunathan, K.; Levitus, M. *J Phys Chem B* **2007**, *111*, 11064–11074.

(11)   Chibisov, A. K.; Zakharova, G. V.; G rner, H. *Faraday Trans.* **1996**, *92*, 4917.

(12)   Konishi, T.; Sasaki, Y.; Fujitsuka, M.; Toba, Y.; Moriyama, H.; Ito, O. *J. Chem. Soc., Perkin Trans. 2* **1999**, 551–556.

(13)   Wilkey, J. D.; Schuster, G. B. *J. Org. Chem.* **1987**, *52*, 2117–2122.

(14)   Mishra, A.; Haram, N. S. *Dyes and Pigments* **2004**, *63*, 191–202.

(15)   Benmansour, H.; Castro, F. A.; Nagel, M.; Heier, J.; Hany, R.; Nüesch, F. *CHIMIA* **2007**, *61*, 787–791.

(16)   Véron, A. C.; Zhang, H.; Linden, A.; Nüesch, F.; Heier, J.; Hany, R.; Geiger, T. *Org. Lett.* **2014**, *16*, 1044–1047.

(17)   Wicht, G.; Bücheler, S.; Dietrich, M.; Jäger, T.; Nüesch, F.; Offermans, T.; Tisserant, J.-N.; Wang, L.; Zhang, H.; Hany, R. *Solar Energy Materials and Solar Cells* **2013**, *117*, 585–591.

(18)   Chatterjee, S.; Davis, P. D.; Gottschalk, P.; Kurz, M. E.; Sauerwein, B.; Yang, X.; Schuster, G. B. *J. Am. Chem. Soc* **1990**, *112*, 6329–6338.

(19)   Heier, J.; Peng, C.; Véron, A. C.; Hany, R.; Geiger, T.; Nüesch, F. A.; Vismara, M. V.; Graeff, C. F. **2014**, 918408–918408–10.

(20)   Fan, B.; Araujo De Castro, F.; Heier, J.; Hany, R.; Nüesch, F. *Organic Electronics* **2010**, *11*, 583–588.

(21)   Guo, J.; Guo, J.; Ohkita, H.; Ohkita, H.; Benten, H.; Benten, H.; Ito, S.; Ito, S. *J. Am. Chem. Soc* **2010**, *132*, 6154–6164.

(22)   Cook, S.; Ohkita, H.; Kim, Y.; Benson-Smith, J. *Chemical Physics Letters* **2007**, *445*, 276–280.

(23)   Peckus, D.; Devižis, A.; Augulis, R.; Graf, S.; Hertel, D.; Meerholz, K.; Gulbinas, V. *J. Phys. Chem. C* **2013**, *117*, 6039–6048.

(24)   x. *A. Devizis, unpublished work*; 2014.

(25)   Devižis, A.; Hertel, D.; Meerholz, K.; Gulbinas, V.; Moser, J. E. *Organic Electronics* **2014**, *15*, 3729–3734.

(26)   de Miguel, G.; Ziółek, M.; Zitnan, M.; Organero, J. A.; Pandey, S. S.; Hayase, S.; Douhal, A. *J. Phys. Chem. C* **2012**, *116*, 9379–9389.

(27)   Jia, K.; Wan, Y.; Xia, A.; Li, S.; Gong, F.; Yang, G. *J. Phys. Chem. A* **2007**, *111*, 1593–1597.

(28)   Heier, J.; Groenewold, J.; Huber, S.; Nüesch, F.; Hany, R. *Langmuir* **2008**, *24*, 7316–7322.

Chapter 4

Photoinduced processes in small molecule photovoltaic systems: cyanine Cy3-P/fullerene bilayers
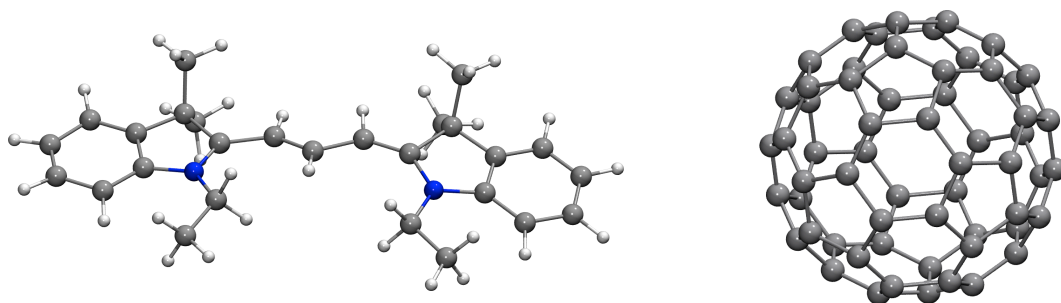
Designed by Marine Bouduban

4.1 Introduction

Organic solar cells based on small molecules have shown up to 10% efficiency in tandem solar cells, and above 8% in single junctions.[1] They are more advantageous than polymer solar cells in terms of costs, as the batch-to-batch reproducibility and purification processes are simplified.[2] Efforts are currently pursued toward improved stability and device performances as they still provide lower power conversion efficiencies than state of the art polymer:fullerene blends.[3] However, the photophysical processes in small molecule-based organic solar cells have been less studied than in polymer:fullerene blends, and only few studies involved time-resolved spectroscopical investigations of bilayers.[4,5] Cyanine/C_{60} bilayers have demonstrated competitive photovoltaic power conversion efficiency, reaching up to 3.6 %.[6-9] It is the purpose of this chapter to overview the dynamics of photophysical processes and charge carriers separation in cyanine/fullerene bilayers. In those planar heterojunctions, the interfacial area is smaller than in bulk heterojunction solar cells, the latter being specifically designed to avoid exciton loss in pure donor or acceptor domains. Bilayers however show their advantage by geometrically separating charge transport and avoiding efficiently charge recombination. Cyanine bilayers based on Cy3-P (see structure in Figure 3.1, Chapter 3) have been employed rather than blends as phase separation in blends becomes critical.[7] High extinction coefficient values in cyanine allow thin active layers, which is highly beneficial in planar heterojunction. The energy levels of the investigated bilayers are shown in Figure 4.1.[10]

Scrutinizing both materials separately is of paramount interest to understand the dynamics of charge carrier separation in the bilayer. Ultrafast pump-probe techniques have been employed in this work to explore the photophysical processes, in addition to steady-state absorbance and electroabsorption measurements. Transient absorption on ultrafast time scales enables to monitor the change in absorption due to transient species such as excited states and

charge pairs. Electromodulated differential absorption is more sensitive to charge pairs and separated charges as they reduce the electric field applied during their drift toward the corresponding electrodes of the full solar cell device.

Ultrafast transient absorption in solution for a cyanine dye is described in Chapter 3. Following excitation, the excited state decaying by stimulated emission back to the ground state is the major recombination process. Photoisomerisation of the Cy3 dye also occurs on longer time scales (ns). The cyanine with borate counter-anion (Cy3-B) undergoes intra ion-pair reductive quenching in the solid state as described in Chapter 3. Hexafluorophosphate counter-anion is not redox active. However, we will see that the cyanine hexafluorophosphate (Cy3-P) shows entangled excited state dynamics.

Fullerenes are commonly employed as electron acceptor in organic solar cells, mainly due to the high electron mobility characterizing this material.[11,12] Recent investigations have shown that access to either delocalized π-electron states or charge transfer (CT) states in crystalline fullerene regions enable efficient charge separation in polymer:fullerene blends, and that initial (40 fs) electron-hole pairs are separated by about 4 nm across the polymer:fullerene interface.[13-15] Time-resolved photophysical properties and energy levels involved upon light absorption in C_{60} thin films are described in detail in this work.

The mechanism of charge separation at the Cy3-P/C_{60} interface has been investigated with both transient absorption spectroscopy, and time-resolved electroabsorption based on the transient Stark effect. This work reports the
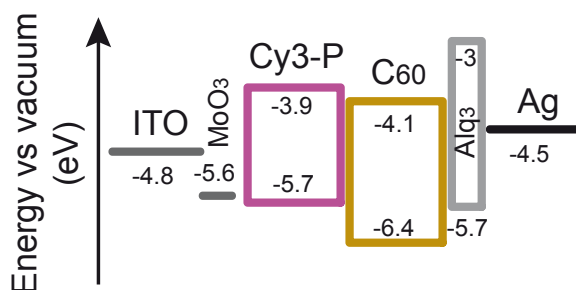

Figure 4.1 Energy levels vs vacuum for a Cy3-P/C60 bilayer, as well as the electrodes in full solar cell devices.

timescales of ultrafast electron and hole transfer, as well as interfacial charge transfer state dissociation in Cy3-P/C$_{60}$ bilayers for the first time.

This chapter is based on two publications: "Dissociation of charge transfer states and carriers separation in bilayer organic solar cells - A time-resolved electroabsorption spectroscopy study" by A. Devižis, J. De Jonghe-Risse, R. Hany, F. Nüesch, S. Jenatsch, V. Gulbinas and J.-E. Moser, submitted to *Journal of the Amercian Chemical Society*, 2015. All the transient absorption data presented here have been carried out by the author. Steady-state electroabsorption was partly measured by the author, and Marine Bouduban. Time-resolved electromodulated differential absorption were measured by Dr. A. Devižis. Samples were prepared by the author, Martina Causa', Gaëtan Wicht, Sandra Jenatsch and Hui Zhang.

4.2 Cy3-P absorbance and fluorescence in the solid state

Let's first consider the steady-state absorbance of a cyanine dye as shown in Figure 4.2. In chlorobenzene solution, the vibronic structure of the first electronic state displays absorption features located at 480, 525 and 560 nm. In the solid-state, Cy3–P absorbs in the visible range with maxima located at 575 and 530 nm. The hypsochromically shifted shoulder located at about 485 nm is attributed to the presence of a few H-aggregates.[16] The morphology of the dye layer is amorphous, due to the spin-coating technique employed, and is evidenced by the red-shift as well as the broadening of the absorbance compared to the one in solution. The absorbance in the solid-state is weakly dependent on the counter-anion.[17] For the rest of the chapter, the results shown are for solid-state Cy3-P samples.
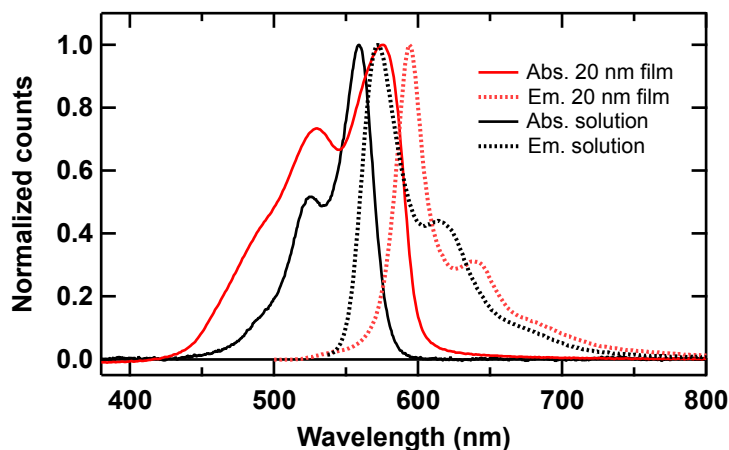
Figure 4.2 Normalized absorbance spectra of Cy3-P 20 nm film (spin-coated from chlorobenzene) and Cy3-P solution in chlorobenzene (5.10^{-7} M). The fluorescence spectra are shown in dotted lines (excitation wavelength: 500 nm for thin film, 525 nm for solution).

The fluorescence spectra displays a small Stokes shift and two maxima located at 593 and 640 nm. The fluorescence spectra does not change upon excitation wavelength (not shown), which indicates that the same species is at the origin of the whole fluorescence spectra, which is the monomeric Cy3-P due to the resemblance with fluorescence in solution.

In Figure 4.3 a, the absorption spectra of Cy3-P/C_{60} bilayers are shown. The fullerene C_{60} absorption onset is at about 530 nm and increases in the UV region. The fluorescence spectra of neat Cy3-P films and the quenching upon addition of fullerene C_{60} is shown in Figure 4.3 b. The increase in Cy3–P thickness yields a fluorescence spectra of similar amplitude but slightly red-shifted with respect to the 20 nm thick film. The latter is likely due to a reabsorption of the blue part of the fluorescence.[18] The light penetration depth is probably about 20 nm, explaining the similar amplitudes. Efficient quenching is observed for bilayers compared to the neat Cy3-P films. The quenching is as high as 95.4% for 20 nm cyanine thickness (Table 1) and lowers to 78.0% for 45 nm cyanine layers when excited at 530 nm. This indicates that exciton diffusion through the Cy3-P is not a major issue in order to reach the interface with C_{60}. However, a thinner Cy3-P layer shows a larger quenching value, indicating that part of the excited states formed further from the interface are still lost by deactivation to the ground state
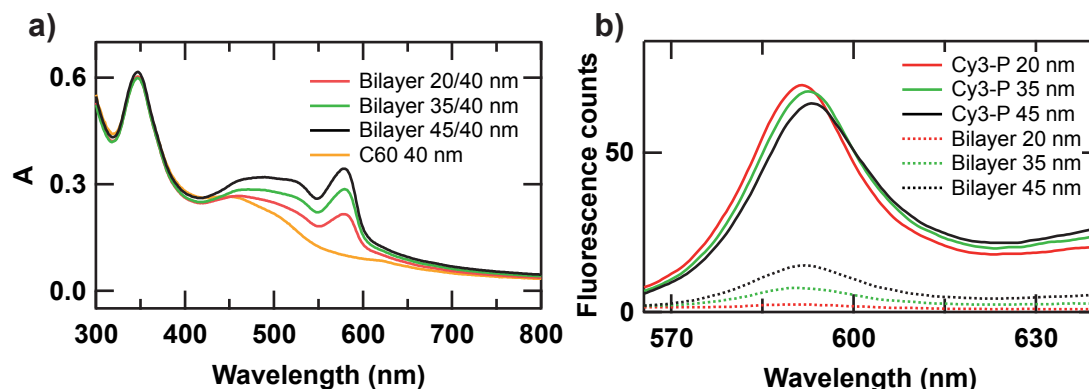
Figure 4.3 Cy3-P thin film (20, 35 and 45 nm thickness) bilayers with C_{60} thickness 40 nm. a) absorbance spectra and b) fluorescence spectra (530 nm excitation, excitation from C_{60} side). The thickness was measured by profilometry with an accuracy below 1 nm.

(radiative or non-radiative). We will discuss this also with respect to time-resolved stimulated emission data (see section 4.3.2). The quenching values are similar for 575 nm excitation wavelength (where only Cy3-P absorbs), which shows that C_{60} absorption is minimal and does not contribute to a loss of fluorescence signal in bilayers (Table 1). Moreover, energy transfer to C_{60} is not possible energetically (Figure 4.1) implying that only electron transfer from Cy3-P to C_{60} is responsible for the fluorescence quenching.

	20 nm	35 nm	45 nm
530 nm excitation	0.95	0.88	0.78
575 nm excitation	-	0.85	0.77

Table 1 Time-integrated fluorescence quenching in Cy3-P/C_{60} bilayers for various Cy3-P thicknesses and two excitation wavelengths, defined as: 1 - I(bilayer)/I(neat cyanine) where I is the time-integrated fluorescence intensity. The time-integrated fluorescence intensity value is the area under the emission band (570 – 630 nm).

4.3 Transient absorption: 540 nm excitation

4.3.1 Neat Cy3-P solid-state films

The transient absorption spectra for neat Cy3-P (45 nm) spin-coated from chlorobenzene on glass is shown in Figure 4.4 a. Although the overlap of various transient signals makes the analysis non trivial, a multiexponential fit helps for the understanding of the photoinduced processes. The result of the fit is shown in Figure 4.4 b for several wavelengths, as well as the amplitude associated spectra in the bottom of Figure 4.4 a.

Following excitation at 540 nm, excited state absorption (ESA) spanning over 350–460 nm, ground-state bleaching (GSB) over 450–520 nm, and stimulated emission (SE) over 580–730 nm are observed at the first time delay of 0.13 ps. SE is similar to steady-state fluorescence data (Figure 4.2) and the ESA resembles the ESA in solution (see Chapter 3, Figure 3.2). The excitation populates multiple levels in the electronic excited state, and the high lying states relax to a lower lying excited state, as indicated by the red-shift of stimulated emission around 640 nm on early time scales.

Exciton-exciton annihilation at $20\,\mu J/cm^2$ fluence are minimized as the Figure 4.5 shows that higher fluences than the fluence used contain a faster decaying dynamics. The mechanism of exciton-exciton annihilation is a bimolecular process occurring at high exciton concentrations, and therefore quadratic with light intensity (fluence). Charge generation can occur from exciton-exciton annihilation, as the excess energy is used for driving the electron-hole pair apart. In our case however, higher fluences only accelerate the dynamics of ground state recovery but do not affect the spectral shape of the transient absorption spectra, excluding charge generation via this secondary mechanism (not shown).

The SE at 640 nm decays mainly with 0.37 and 3.8 ps time constants (Figure 4.4 a and b). The GSB dynamics at 510 nm though, shows multiphasic

recombination with time constants of 41.4 ps and longer, but little on the early timescales. Actually, the fit is unable to follow the slight negative growing of the signal with 0.37 ps time constant, and instead a rather flat signal is observed (Figure 4.4 b). Even more surprisingly, the negative signal at 560 nm located near the maximum of Cy3-P GSB still grows more negative with 0.37 and 3.8 ps time constants (Figure 4.4 b). We can thus conclude that a transient species absorbing at 560 nm with a tail around 510 nm superimposes with the large non decaying GSB, resulting in a small negative signal growing over the first time constant of 0.37 ps. It is important to note that at 560 nm the GSB amplitude should be similar to 510 nm (see Figure 4.2). This is the case as the first time constant vanishes at about 1 ps.

The GSB at 560 nm continues to grow more negative with 3.8 ps time constant, but not the GSB at 510 nm, which shows minor recovery on this time scale. Moreover, the blue part of the excited state represented by the 400 nm band decays mainly with 3.8 ps time constant, as well as the red-shifted SE. These various observations indicate that the excited state decay does not repopulate the ground state, but rather a lower lying energy state of non-emissive character. This state is probably in a neighboring molecule, resulting from electron injection, which ground state absorbance is located around 560 nm. The exact mechanism is however unclear, and could be due to the close proximity of neighboring molecules (in dimers for example). We tentatively ascribe this low lying state to an intermolecular charge transfer state, as this has been observed for merocyanine molecules.[19]

Moreover, the red part of the ESA represented by the dynamics at 440 nm does not decay with the first time constant (0.37 ps), therefore linked to the more relaxed excited state formed by both excitation and vibrational relaxation from the upper excited states, as the shift in SE already suggested. The dynamics actually decays first within 3.8 ps, which is either by SE or formation of the
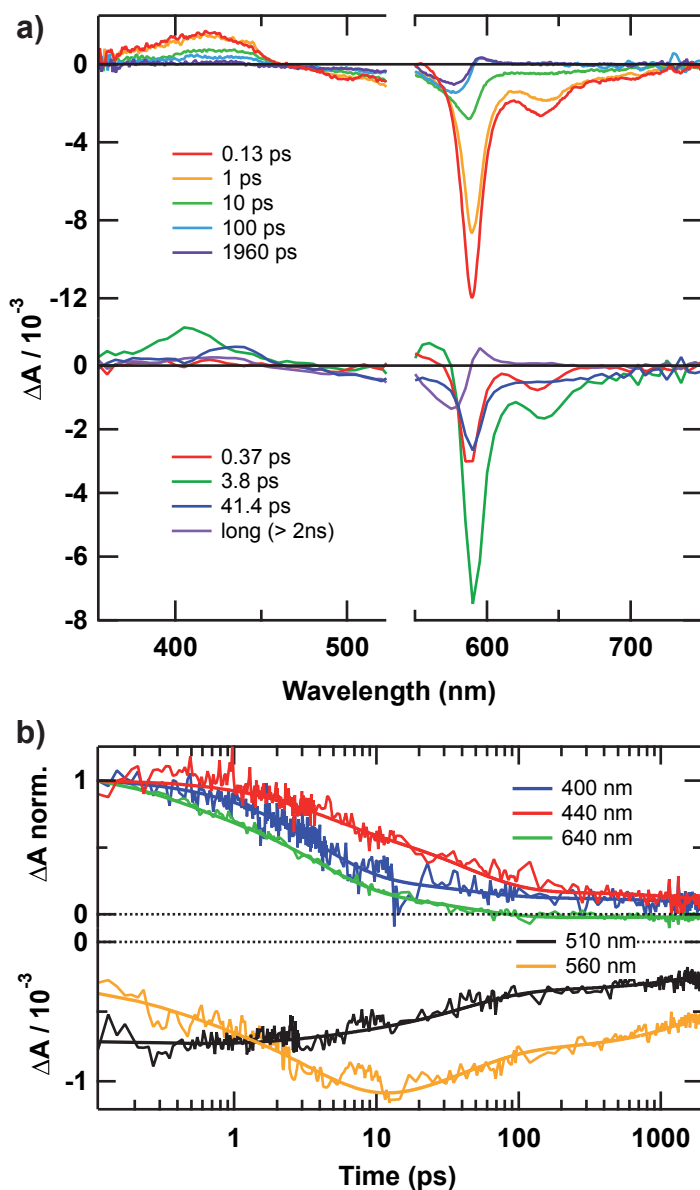

Figure 4.4 a) Transient absorption spectra of neat Cy3-P (45 nm) recorded for 540 nm excitation and various probe time delays, fluence: 20 µJ/cm². The bottom graph is the decay-associated spectra resulting from a multiexponential fit. b) Shows the dynamics extracted from a). The solid lines superimposed on experimental data are the result of the best multiexponential fit.

lower lying energy state, but also with a 41.4 ps time constant. Actually, the amplitude spectra associated to the 41.4 ps time constant (Figure 4.4 a, bottom graph) is very similar in shape to the electroabsorption due to the Stark effect (EA) of Cy3-P (see Figure 4.13 a). Although various photoabsorptions overlap, it is quite striking how the global fit has extracted this EA spectra in the transient absorption data. EA originates from local electric fields induced by charge transfer states for example, as they have a strong associated electrical dipole, and perturb the electronic transitions of the surrounding molecules.[20] This perturbation results in a shift in the ground state absorbance of neighboring molecules probed and affected by the electric field. EA in transient absorption data has been reported for different systems such as dye-sensitized solar cells, polymer:fullerene blend films and neat fullerene films.[21-25] It is however not systematically assigned in transient absorption spectra, and could explain the oscillatory features observed in TA data. This EA has a dynamic character and is assigned to a bound electron-hole pair. The EA decay is an indication that the charge pairs recombine. In transient absorption, an ensemble of molecules is probed simultaneously, probing both molecules further away from the charge pair dipole as well as molecules in between the charge pair. The electric field intensity is different for those various positions, and will also vary upon distance between the charge pair. However, as it is unlikely that the charge pairs separate further into free charges in this case, we assume that the EA decay is due to recombination of the electrons and holes. This will be confirmed in time-resolved electroabsorption measurements (see section 4.5).

Residual SE is also observed in the 41.4 ps amplitude spectra, originating from the relaxed excited state. This is in accordance with the solid state Cy3 excited state lifetime of 50-120 ps measured by fluorescence decay (not shown).[17] The charge transfer state resulting from electron injection into a neighboring Cy3-P shows EA, but no clear indication of oxidized and reduced Cy3 (thus, fully dissociated) species are observed, as their absorptions are located at 450 and 550 nm, respectively (Chapter 3).[6] We can however not fully exclude their

presence, but charge separation in neat small molecular films in the absence of external field is quite unexpected.[26]

The Cy3-P triplet excited state is not observed, as its absorption is located around 600-650 nm in the film (see Chapter 3) and the quantum yield is rather low (0.03 in argon-saturated solution).[27] At longer time delays, the *cis*-isomer absorbing at 590 nm becomes noticeable (Figure 4.4 a), and the reader is referred to Chapter 3 for more details on photo-isomerization.
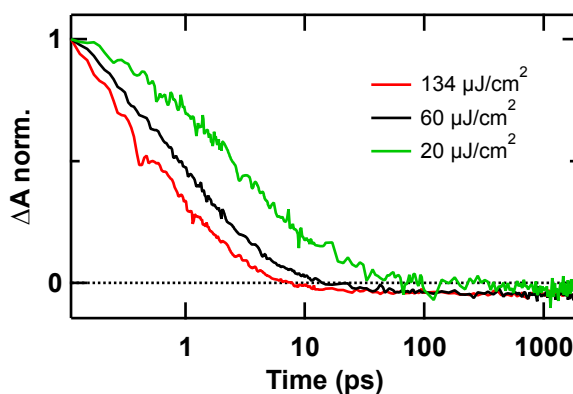

Figure 4.5 Transient absorption dynamics for Cy3-P (45 nm film) recorded at 640 nm probe wavelength after 540 nm excitation, for various excitation intensities. The intensity-dependent dynamics show minimal bimolecular annihilation at low fluences.

4.3.2 Cy3-P/C_{60} bilayers

The transient absorption spectra for the Cy3-P bilayer with the electron acceptor C_{60} is shown in Figure 4.6. Spectral and dynamical differences with respect to neat Cy3-P are observed. At first, it is very clear that the initial intensity for SE, thus at 0.13 ps, is a factor four lower than for neat Cy3-P. This indicates that electron injection from the Cy3-P excited state to the C_{60} occurs within the time resolution of the setup, with an efficiency of about 70%. Absorption by C_{60} at the excitation wavelength (530 nm) is weak, but could lower this apparent value by a few percent. Moreover, no vibrational relaxation in Cy3-P is observed as the SE does not red-shift over time (see 640 nm probe in Figure 4.6, 0.13 ps and 1 ps time delays). Residual SE decays with 0.88 and 5.46

ps, but not on longer time scales as observed for neat Cy3-P. These statements indicate multiphasic electron transfer. The first one dominates on ultrafast (< 0.13 ps) timescales from hot excited states, while relaxed excited states also inject on the tenths of ps timescale.

Secondly, a clear positive signal at 560 nm is now observed compared to neat Cy3-P. At early timescales in neat Cy3-P, only little GSB is observed, as a short lived transient species overlaps at this wavelength. The dynamics at 560 nm are shown in Figure 4.7 for several Cy3-P thicknesses and the corresponding bilayers with C_{60}. While in all neat Cy3-P samples, the signal is negative, in the bilayers the signal is clearly positive up to a few ps. One explanation is that the transient species overlapping with GSB in neat Cy3-P is actually enhanced and its deactivation delayed in the presence of C_{60}. The fluence being the same for all samples, the thickest Cy3-P layer displays a larger negative (maximizing around 10 ps) value due to an increase of photons absorbed upon excitation.
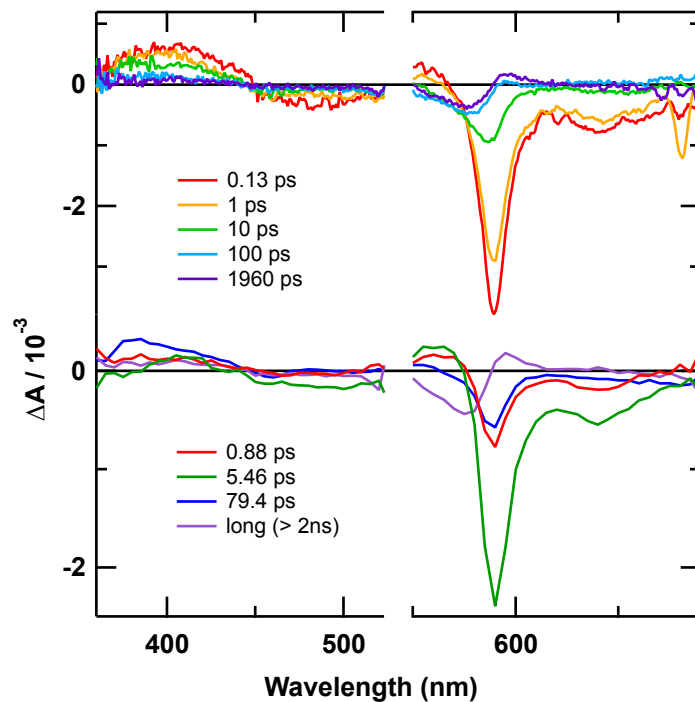

Figure 4.6 Transient absorption spectra of the bilayer Cy3-P (45 nm) / C_{60} (40 nm) recorded for 540 nm excitation and various probe time delays, fluence: 20 $\mu J/cm^2$. The bottom graph is the decay-associated spectra resulting from the multiexponential global analysis.

No intensity effect is observable in none of the four samples at the fluence used, and the dynamics at low fluence do not depend on the Cy3-P thickness. Moreover, the bilayers show the initial amplitude not being significantly different between both Cy3-P thicknesses (Figure 4.7 a). With these various statements, we can safely assume that the initial positive amplitude at 130 fs originates from the interface between Cy3-P and C_{60}. C_{60} EA displays a maximum feature around 545 nm (see Figure 4.10), as well as two minor features at 505 and 450 nm. Those features are evidenced in Figure 4.6 in the 0.13 ps spectrum. The origin of EA is either due to interfacial electron injection resulting in an interfacial CT state (bound electron-hole pair), or the CT states in Cy3-P which electric fields affect the absorbance of C_{60} ground state molecules. The overlap with GSB does not allow a clear picture of its origin and recombination. As no field is applied, it is unlikely that this CT state will split into free charge carriers but rather relax or recombine to the ground state. The C_{60} anion absorbs in the nIR around 1030 nm and 950 nm and is therefore located outside the spectral range investigated here.[28] However, its extinction coefficient is quite low and rather difficult to observe, and data recorded over the nIR range did not show any transient data (not shown).

The dynamics at 440 nm assigned to Cy3-P ESA and EA are strongly reduced (Figure 4.7 b) in the bilayers, and actually only the blue-side of ESA shows multiphasic recombination with a large amplitude associated with the 79.4 ps time constant (Figure 4.6). Probably the C_{60} GSB and EA, which are both negative, overlap with the positive Cy3-P relaxed excited state absorption at 440 nm, but also vibrational relaxation from high lying excited states to lower lying states is suppressed in the bilayer with C_{60} due to ultrafast electron injection.
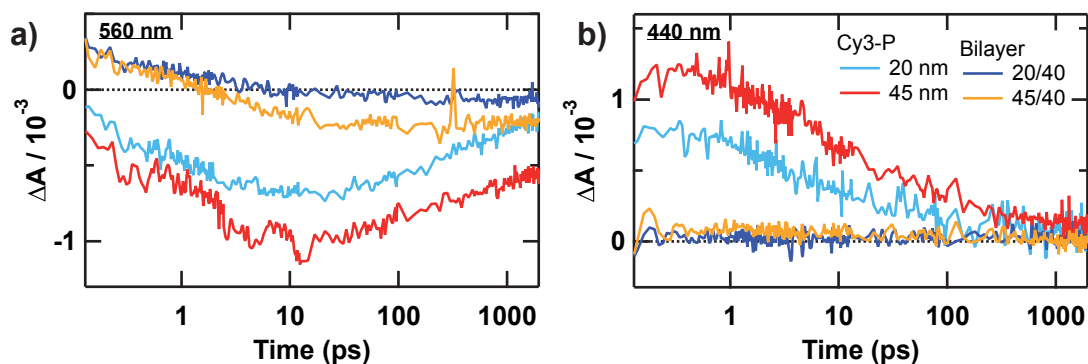
Figure 4.7 Transient absorption dynamics recorded after 540 nm excitation (20 μJ/cm^2) for neat Cy3-P layer (20 and 45 nm thick) and the corresponding bilayers with C_{60} (40 nm thick) at a) 560 nm probe, and b) 440 nm probe wavelength.

The amplitude spectra assigned to the long time scale (Figure 4.6) is similar to the one observed for neat Cy3-P (Figure 4.4) indicating that all the excited molecules have not returned to the ground state, and isomerization has likely occurred.

Electron transfer from Cy3-P to C_{60} seems to occur mostly within 0.13 ps. Delayed electron transfer is also observed. However, spectral features and dynamics are strongly intricate in neat Cy3-P, and they are even more in the bilayer with C_{60}.

4.4 Transient absorption: 390 nm excitation

The origin of charge carriers in organic solar cells is twofold: both donor and acceptor absorb light. The internal photon to current efficiency (IPCE) is often reported as a function of excitation wavelength in order to characterize in which spectral region the solar cell works best. It is quite clear that most fullerene based devices do show pretty good IPCE values in the near UV region, where most of the time the donor does not absorb anymore.[10] Therefore, selective excitation of the electron acceptor is of fundamental importance in order to understand the origin of charge generation in such OPV devices.

4.4.1 Photoinduced processes in C_{60} thin films

Transient absorption spectra of neat C_{60} and PCBM (fullerene derivative) thin films have been reported in the literature. The singlet excited state formed upon excitation absorbs in the IR range (above 700 nm), and recombination by fluorescence occurs on the ns time scale. [12,29] Intersystem crossing to the triplet state has been observed in solution with a near unity quantum yield with a significant absorbance located around 740 nm for C_{60}.[12,30] In compact pure fullerene films such as those evaporated or deposited from solution, the triplet yield is drastically reduced, as other decaying pathways become accessible.[31] Blends of P3HT:PCBM have shown ultrafast hole transfer (< 250 fs) upon 390 nm excitation, and MDMO:PPV/PCBM blend films have shown hole transfer taking place on time scales as short as 30 fs.[32,33] While hole transfer is ultrafast, exciton diffusion limits the charge transfer rate at the interface.[34]

The absorbance spectrum of C_{60} in dilute solution features a sharp peak located at 334 nm (Figure 4.8). In thin evaporated films, the amorphous structure leads to a red-shift and broadening of the spectral features.[35] Indeed, the maximum is located around 345 nm (3.6 eV) and a broad shoulder around 450 nm (2.8 eV) becomes visible. C_{60} are conjugated icosahedral molecules, which HOMO and LUMO levels are degenerate and very close in energy.[36] This leads to a mixing of Frenkel and charge transfer (CT) states, which are intramolecular and
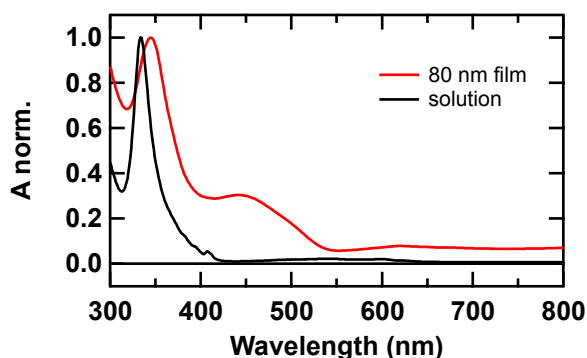

Figure 4.8 Normalized absorbance spectra of a C_{60} dilute solution ($\approx 10^{-6}$ M) and 80 nm evaporated thin film.

intermolecular excited states, respectively.

By doubling the frequency of the CPA Clark laser (775 nm) with a BIBO crystal (see Chapter 2 for more details on SHG), a 390 nm pump was used for selective C_{60} excitation. The beam was not compressed leading to a time resolution of 300 fs.

The transient absorbance spectra for a 40 nm thick C_{60} film is shown in Figure 4.9 a. The singlet excited state (Frenkel intramolecular exciton) absorbing over a broad range of wavelengths and increasing in the nIR appears at 0.3 ps.[12] Overlaid we observe the C_{60} photoinduced Stark effect featuring distinct peaks at 550, 505 and 455 nm in the 0.3 ps TA spectra as well. The steady-state electroabsorption under an applied external field was measured as a comparison,
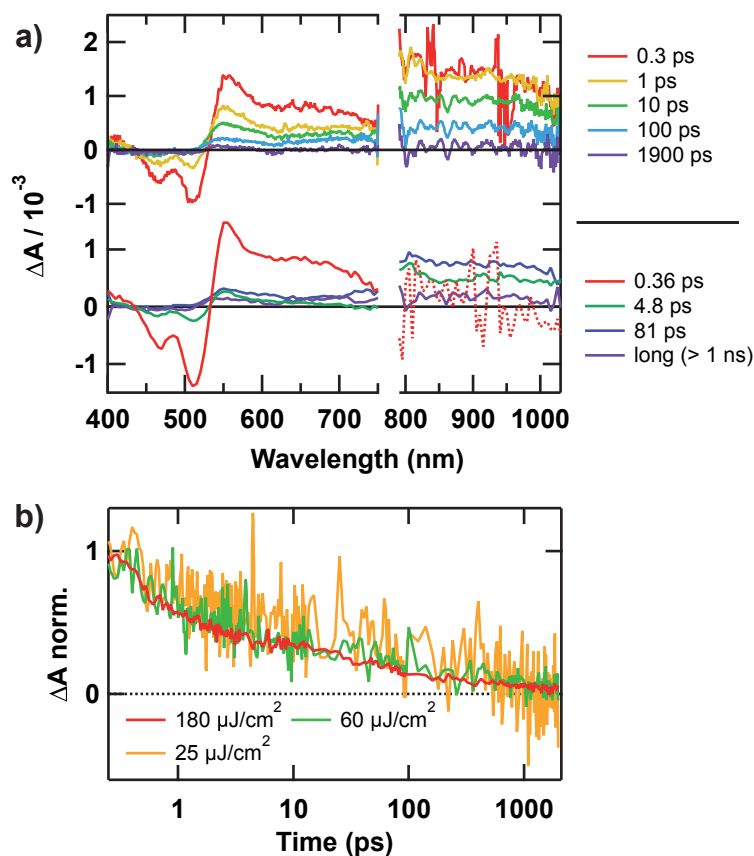
Figure 4.9 C_{60} (40 nm), recorded for 390 nm excitation: a) transient absorption spectra at various probe time delays at an excitation fluence of 180 µJ/cm². The bottom graph is the amplitude associated spectra resulting from the global analysis. b) transient absorption dynamics normalized at 0.3 ps at various excitation fluences for 550 nm probe wavelength.
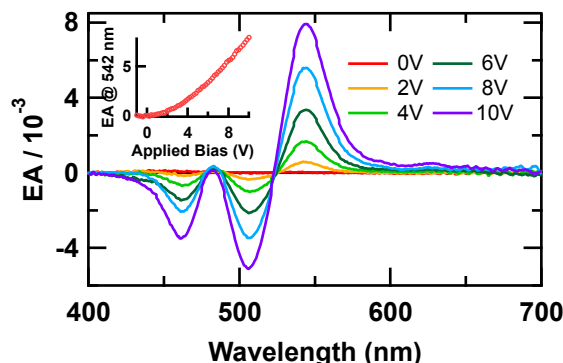
Figure 4.10 Electroabsorption spectra for 80 nm C_{60} thin film at various applied bias. The inset shows the quadratic dependence of the EA amplitude at 542 nm as a function of externally applied bias.

shown in Figure 4.10. It is quadratic with the applied voltage. Electroabsorption of C_{60} due to the Stark effect in transient absorption spectra has been reported in the literature and assigned to local electric fields induced by photogenerated charge carriers, delocalized excited states or even delocalized charge pairs.[23,37-41] Delocalization over several molecules of the excited state or charge pairs leads to a strong associated electrical dipole, which perturbs the electronic transitions of the surrounding molecules.[20]

In C_{60}, it is known that free charge carriers can be generated by exciting at wavelengths lower than 530 nm under an applied field.[42] Charge separation in neat C_{60} without external field applied is however not clear, and moreover the charge separated states show little absorption due to low extinction coefficients. We however speculate that the bands at 650 and 950 nm are due to geminate charge pairs (charge transfer states) on neighboring molecules.[41] Actually, Figure 4.9 b shows identical dynamics for various fluences corroborating the absence of bimolecular recombination that would be observed if fully charge separated species were created. The transient absorption at 650 nm is therefore an overlap of excited state and geminate electron-hole pair absorption.

In order to understand the photophysical processes in C_{60}, a multiexponential fit was performed and the resulting amplitude associated spectra is shown in the bottom of Figure 4.9 a. The dynamics at various wavelengths and result of the fit

are shown in Figure 4.11. Figure 4.12 shows the energy levels in C_{60} thin films, which are derived from the following observations.

The first two time constants (0.36 and 4.8 ps) are assigned to EA, as due to the similarity of the amplitude spectra (Figure 4.9 a, bottom graph) and EA in Figure 4.10. This EA is assigned to a delocalized (i.e. intermolecular) charge transfer state, as we observe the geminate charge pair signatures at 650 and 950 nm. At 950 nm however, the absorbance is mostly assigned to the Frenkel exciton, which also absorbs up to 545 nm. As all EA features, as well as the 650 nm band, recombine with 0.36 ps, we can conclude that the charge transfer state created upon excitation at 390 nm is delocalized over several molecules at first, and localizes back on one fullerene molecule in 0.36 ps. This localization can return to a Frenkel exciton, or a lower lying CT state. Therefore at 950 nm, the signal remains unaffected on this time scale, due to equal contribution of the growing Frenkel exciton and recombination of geminate electron/hole pair in the delocalized CT state. This conclusion is supported by the GSB signal at 475 nm also decaying with 0.36 ps, due to the delocalized CT state affecting two molecules, localizing back on one molecule. The intramolecular CT and residual delocalized CT are responsible for the second decay of EA signals at 4.8 ps.

Upon this time scale, the Frenkel exciton also starts to decay (dynamics at 950 nm, Figure 4.11), as well as with 81 ps time constant.
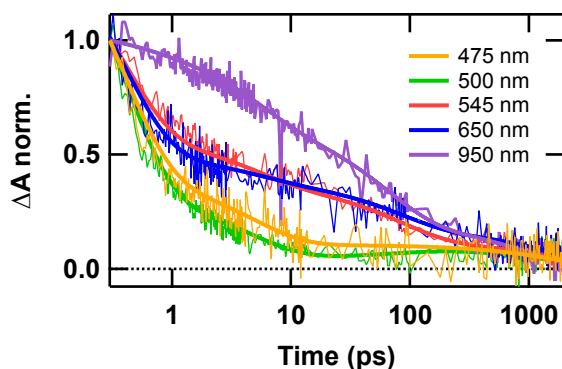

Figure 4.11 Transient absorption dynamics recorded at various probe wavelengths after 390 nm excitation for a 40 nm thick C_{60} film.
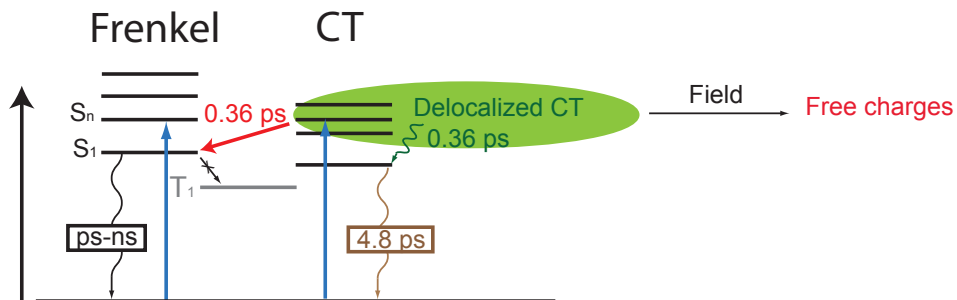
Figure 4.12 Schematic representation of the energy levels in C_{60}. The EA features are associated with delocalized charge transfer states that localize in 0.36 ps to so called intramolecular charge transfer states, or Frenkel excitons. Those localized CT states show less EA and recombine with 4.8 ps to the ground-state.[10] Finally the Frenkel exciton, or singlet excited state, is generated upon excitation but also by localization of the CT state. It recombines mostly with 81 ps but some excitons live for over a nanosecond, in accordance with fluorescence lifetimes reported in the literature of 1.2 ns.[14] Free charges can be formed at excitation wavelengths < 530 nm in the presence of a field (see section 4.5).

The Frenkel exciton, or self-trapped exciton as described by Ebbesen et al., can diffuse through the molecular thin film during its whole lifetime, but can be shortened when a recombination site is reached, such as an impurity, or any smaller band gap material, for example Cy3-P such as discussed in the next section.[30]

No evidence of the triplet state absorbing at 740 nm could be found, in accordance with other reports investigating PCBM thin films which advance that the close packing of fullerene molecules induces other excited-state relaxation pathways hindering the triplet generation, as opposed to near unity triplet quantum yield in solution.[43]

Clements et al. have studied both C_{60} colloids and solvated (single) molecules in solution.[44] The C_{60} colloids consist of 100 nm size particles containing multiple C_{60} molecules. The difference in transient spectra is striking: while the single molecule shows ESA and intersystem crossing to the triplet state absorbing at 740 nm, the colloid solution shows identical spectra to the one observed in thin films such as in Figure 4.9. Although the authors do not discuss further the details of the colloid TA spectra, the initial spectra at 0 ps decaying with 0.53 ps is obviously originating from a photoinduced Stark effect. As we have shown in

this work, the photoinduced Stark effect does show a significant signal in transient absorption data, even at low fluences. This suggests that careful identification of the EA peaks by steady-state electroabsorption should be carried out in addition to femtosecond transient absorption data.

4.4.2 Photoinduced processes in Cy3-P/C60 bilayers

In the bilayer with Cy3-P, only C_{60} absorbs at 390 nm (Figure 4.2 and 4.3 a) and neat Cy3-P does not show any transient signal upon 390 nm excitation (not shown). The steady-state electroabsorption for Cy3-P and the bilayer are shown in Figure 4.13 a. Cy3-P displays a positive peak at 450 nm, and a smaller negative peak at 590 nm. The small contribution is evidenced in Figure 4.13 b, as the EA amplitude corresponding purely to Cy3-P around 590 nm is low compared to the C_{60} EA main feature at 545 nm. To be noted, the samples used for steady-state electroabsorption were of different thickness compared to the ones measured by transient absorption. But by carefully changing the voltage and knowing that the electric field applied is inversely proportional to the thickness, the curves shown in Figure 4.13 a all correspond to about 0.4 MV/cm.

The transient absorption spectra of the bilayer is shown in Figure 4.14. C_{60} EA appears instantaneously along with the nIR band already identified as the lowest
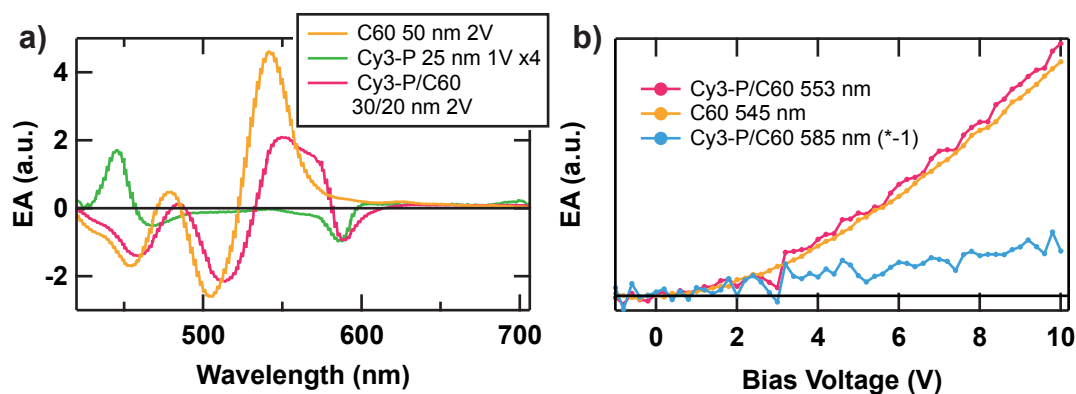

Figure 4.13 a) Electroabsorption spectra of the Cy3-P and C_{60} separately, as well as the bilayer. b) shows the quadratic dependence of the EA peaks on the applied bias.

singlet excited state in C_{60} (Frenkel exciton). However, the signal assigned to EA is more than a factor two higher in the bilayer compared to neat C_{60}. This is valid for three different fluences as shown in Figure 4.15. This strongly indicates that the presence of Cy3-P enhances EA features in C_{60}.

Additionally, the negative feature around 590 nm assigned to Cy3-P EA is observed at 0.3 ps as well. Finally, the nIR band displays a similar amplitude as neat C_{60} for the same fluence, as Figure 4.14 and 4.9 a suggest. Similar to neat C_{60}, the fluence does not impact the dynamics in the Cy3-P/C_{60} bilayer. Interestingly, they are essentially the same as those found in neat C_{60}. Bulk excitations in C_{60} lead to similar spectral features and dynamics, independent of the presence of Cy3-P. However, several conclusions can be drawn from these observations. First, as the dynamics taken from 0.3 ps do not change when Cy3-P is present, while the spectral shape indicates the Cy3-P EA, we tentatively ascribe this to ultrafast (< 0.3 ps) hole transfer to Cy3-P. As the dynamics do not change upon excitation fluence, the hole transfer results in an interfacial charge transfer state. The origin of the higher amplitude of the C_{60} EA in the bilayer is twofold: either a larger electron-hole distance in the bilayer compared to bulk C_{60} CT leads to less screening between geminate charges and generation of higher
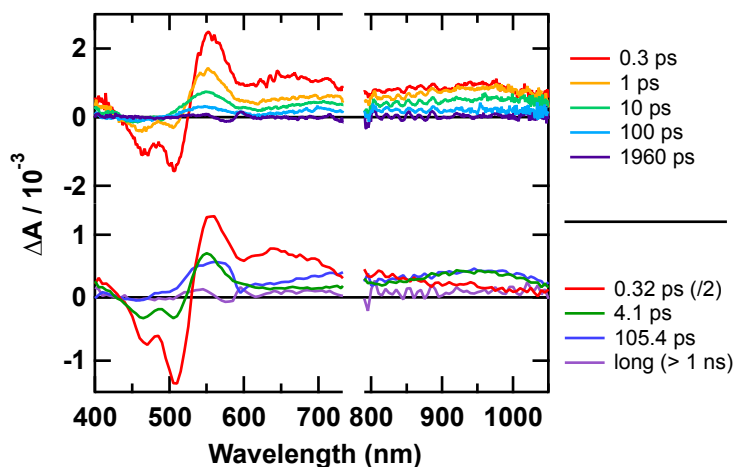

Figure 4.14 Transient absorption spectra at various probe time delays recorded after 390 nm excitation (excitation fluence: 180 µJ/cm^2) for a Cy3-P/C_{60} bilayer (45/40 nm). The bottom graph is the amplitude associated spectra resulting from the global analysis. The amplitude spectra associated with 0.32 ps time constant is divided by two for better comparison.

electric fields, which perturb the neighboring C_{60} and Cy3-P molecules; or the number of CT states is higher in the bilayer, as the energetically higher lying HOMO of Cy3-P favors interfacial HT versus CT in C_{60}. The nIR band decays with same dynamics even when Cy3-P is present. However the spectral shape peaking at 950 nm is now more indicative of the presence of C_{60} electrons. The electrons in C_{60} (or reduced C_{60}) should actually increase the absorbance further near 1030 nm. This is not obvious from Figure 4.14, but this is probably due to our detection limit. The decay of the nIR band is multiphasic, already on the first timescale of 0.32 ps as opposed to neat C_{60}. This is assigned to hole transfer from the Frenkel exciton, which occurs on a multitude of timescales and is difficult to disentangle here. We thus conclude that hole transfer originates from high lying excited states, such as the delocalized CT state, but also from the more relaxed Frenkel state.

The amplitude spectrum associated with the 105.4 ps time constant is substantially different from the 81 ps spectrum for neat C_{60} (Figure 4.14 and 4.9, respectively). Both contain the spectral signature of C_{60} Frenkel excitons and intermolecular CT. In the bilayer, however, a photoabsorption decaying with a 105.4 ps time constant is observed at 450-600 nm. This absorption feature is associated to the oxidized cyanine resulting from hole transfer. Hole recombination dynamics are not accelerated with fluence (not shown), we can
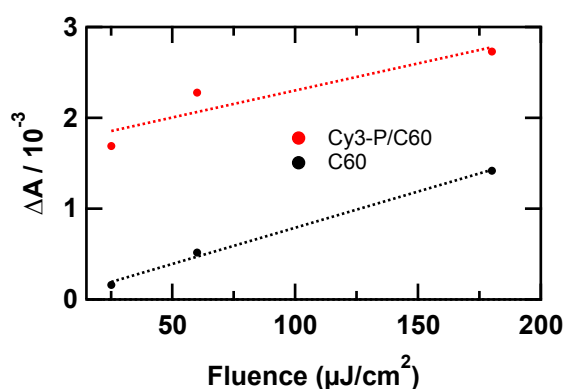

Figure 4.15 Amplitude at 545 nm probe recorded at 0.3 ps delay time after 390 nm excitation, for various fluences. Results for both neat C_{60} (40 nm) and the bilayer Cy3-P/C_{60} (45/40 nm) are shown. Dotted lines are a guide to the eye.

therefore exclude bimolecular recombination resulting from dissociated charge pairs. Rather, the interfacial charge transfer state created recombines to the ground state. On longer time delays, the ground state absorption of Cy3-P at 575 nm is restored. Minor Cy3* isomerization is observed at long time delays. The back-isomerization occurs on the ns time scale.

Multiphasic hole transfer is consistent with the bilayer morphology, where electron transfer occurs from neighboring molecules, whereas exciton/charge carrier diffusion to the interface occurs on a span of timescales depending on the exciton/charge carrier generation site. Energy transfer to Cy3-P is not excluded, however this process would drastically reduce the spectral signatures assigned to C_{60}, which is not the case here.

In order to clarify if either the distance between interfacial CT states or simply the increased number of CT states due to Cy3-P are at the origin of the increase in photoinduced Stark effect, the interface was modified by photopolymerizing C_{60} in the bilayer.

4.4.3 Photopolymerization of C_{60}

UV light exposure of fullerene C_{60} irradiated by a xenon lamp in inert atmosphere induces dimerization, oligomerization, and 3D polymerization.[45] Covalent bonds are formed through a 2+2 cycloaddition reaction between neighboring molecules. The yield of dimerization attains 70% over the six first hours, and longer exposure increases the oligomerization only slightly further. The incident photon-to-current conversion efficiency (IPCE) of Cy3-P/C_{60} devices decreases by about 25%. The exposed cross-linked film is subsequently insoluble in toluene, and the total volume of the film shrinks to about 90% of its initial volume.[45] In bilayer devices, this results in a smaller contact area at the Cy3-P/C_{60} interface due to the formation of voids. No degradation of the Cy3-P, nor that of the Ag contact has been reported.[45] In other systems, oligomerized

PCBM resulted in reduced macroscopic electron mobility and device performance losses, but increase in stability.[46,47]

The effect of 16 h C_{60} photopolymerization is striking when looking at the absorbance spectra as shown in Figure 4.16. The absorbances around 320 nm and 400 nm are increased and globally the features flatten out. The maximum shifts slightly from 345 nm to 342 nm. This is attributed to a change in the band-gap and possibly a shift of the HOMO level.[45]

The steady-state electroabsorption spectra of the devices is shown in Figure 4.17 a. The spectral shape in the visible range does not change significantly whether the C_{60} is polymerized or not, whereas the amplitude is decreased upon polymerization. This may be ascribed to the formation of pinholes upon polymerization. Nonetheless, the C_{60} EA feature at 545 nm is still dominating the spectra, even if the C_{60} is polymerized.

The transient absorption dynamics recorded at the maximum of photoinduced Stark effect are shown in Figure 4.17 b. Careful correction for the increase in absorbance at 390 nm upon photopolymerization has been done, and results in very similar amplitude and dynamics with respect to the non-polymerized sample. This result can be understood as follows: upon C_{60} photopolymerization, the interfacial distance between Cy3-P and C_{60} increases. According to Zhang et al., the root-mean square roughness of the C_{60} surface decreases from 1.6 nm to 0.3 nm after photopolymerization and is accompanied by an increase in C_{60}
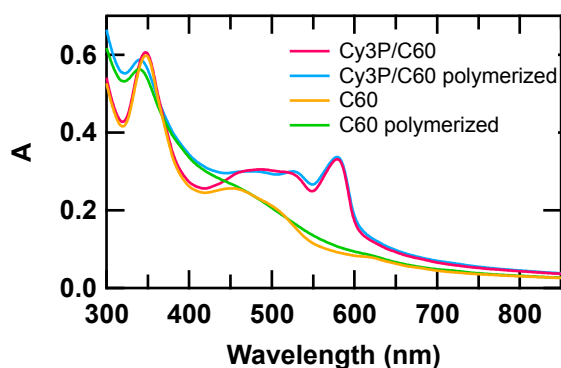

Figure 4.16 Absorbance spectra of C_{60} (40 nm), Cy3-P/C_{60} (40/40 nm), and the same samples photopolymerized under the xenon lamp (1 sun) in nitrogen atmosphere for 16h.

emission after photopolymerization, attributed to a loss of C_{60} excitons and thus poorer HT efficiency.[45] For these reasons, we may assign the similar amplitude obtained in Figure 4.17 b to the fact that the increase in interfacial CT dipole distance (by photopolymerization) impacts the electric field they generate, compensating for the poorer hole transfer efficiency. It is thus not clear yet whether the longer interfacial CT distance or the number of charges increases the C_{60} EA in the bilayer compared to neat C_{60} as discussed in the previous section, but from this experiment we can conclude that a longer distance between geminate electron-hole pairs leads to an increase in amplitude of the photoinduced Stark effect. It is however challenging to scrutinize the volume affected by the electric field generated from the interfacial CT dipole. As the recombination dynamics are not affected by polymerization (Figure 4.17 b), we can safely assume that the increase in interfacial distance of about 1 nm does not inhibit recombination owing to Coulomb attraction of the electron-hole pair.

By applying a voltage to the devices, the interfacial CT state could be dissociated and the mobility could be monitored. Although investigation of photopolymerized C_{60} has not been followed further in this work, due to shortings of the neat C_{60} polymerized devices, Cy3-P/C_{60} bilayers are discussed in the next section.
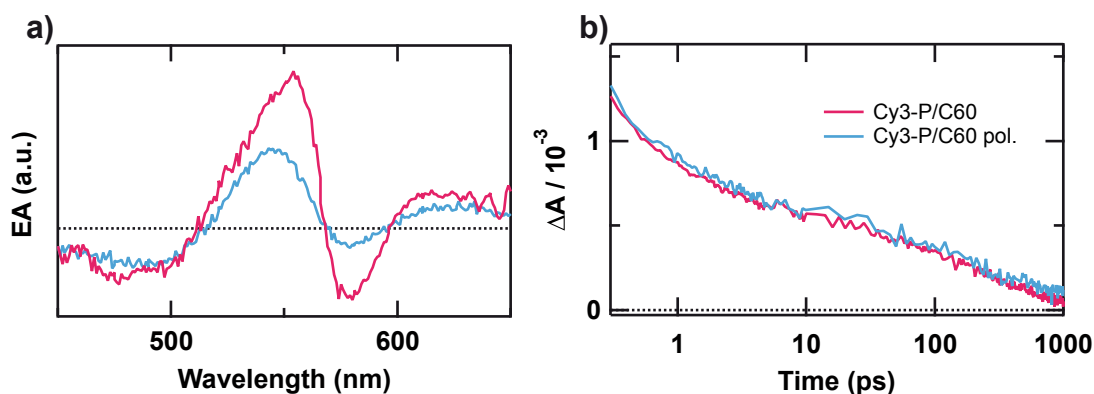

Figure 4.17 Cy3-P/C_{60} (40/40 nm) and Cy3-P/C_{60} (40/40 nm) polymerized sandwiched between ITO/MoO$_3$ and Alq$_3$/Ag electrodes. a) Steady-state EA spectra at 4V applied bias and b) transient absorption dynamics averaged over 530-560 nm probe wavelengths (and corrected for different absorption) after 390 nm excitation at 10 μJ/cm^2 in reflectance mode.

4.5 Electric field dynamics in Cy3-P/C$_{60}$ bilayers

Free charge carrier generation in organic solar cells is still under discussion, as different mechanisms yield substantially different time scales.[15] Ultrafast charge generation (< 1ps) has been suggested to originate from hot states, delocalized excited states, delocalized charges or to be due to high local mobilities.[13,48-51] Slower charge generation via the charge transfer state is suggested from other investigations.[52,53]

From transient absorption measurements on Cy3-P/C$_{60}$ bilayers, no direct evidence of free charge generation is observed after Cy3-P excitation. Nonetheless, ultrafast Cy3-P stimulated emission quenching in bilayers with C$_{60}$ indicate that part of the interfacial charge transfer states are formed within 0.13 ps. Without external electric field though, the CT state seems unable to separate even on longer time scales.

Several time resolved techniques shed light into the charge carrier formation and transport in organic materials.[39] One method built in our laboratory by Dr. Devižis is electromodulated differential absorption (EDA), based on the Stark effect. The Stark effect is described in more details in Chapter 2. In comparison to the photoinduced Stark effect that is observed in transient absorption spectroscopy, the EDA probes the dynamics of photoinduced charges shielding an externally applied electric field.[54] In short, the applied voltage pulse is modulated at half the frequency of the pump and probe pulses, and the obtained differential absorption spectra is the difference at a certain probe delay between a biased and unbiased sample.[55] The sample is thus a full solar cell, i.e. an organic bilayer sandwiched between two electrodes, such as shown in Figure 4.1. The interfacial charge transfer state will now be able to separate due to the external electric field, allowing separated charge carriers to drift toward the electrodes.

To address the EDA measurements, steady-state electroabsorption measurements of Cy3-P and C$_{60}$ are briefly summarized (Figure 4.13 a). C$_{60}$ EA

displays narrow features located at 545, 505 and 455 nm. Cy3-P shows weaker features at 450 and 590 nm. In the bilayer, EA of both materials are observed (Figure 4.13 a) and spectrally separated. We can thus observe the electric field locally in the donor or acceptor layer by observing different probe wavelengths. 590 nm is thus assigned to Cy3-P, and the major peak at 545 nm is assigned to C_{60}. Moreover, the pump excitation can be tuned so that one of the two components is excited only, which gives more insight into the charge carrier formation.

The hole mobility in Cy3-P is about 10^{-5}-10^{-7} cm^2/(V·s).[10] This mobility corresponds to hole extraction in the bilayer on timescales longer than 1 ns. The fullerene C_{60} is a disordered organic semiconductor showing a rather high electron mobility, about 0.5 cm^2/(V·s).[11] A recent investigation of PCBM thin films (fullerene derivative) by electromodulated differential absorption indicate a zero-field electron mobility of 5.10^{-2}cm^2/(V·s).[55] For these reasons, the electroabsorption in the Cy3-P layer is not expected to vary over 1 ns, whereas electrons in C_{60} are likely to drift towards the corresponding electrode and thus decrease the electric field in the C_{60} layer. This is obvious from Figure 4.18, showing the EDA spectra at various time delays. EDA spectra taken at time delays before the pump arrives are identical to steady-state electroabsorption. At positive time delays, the free charges drifting toward the electrodes decrease the total electric field imposed on the sample. Drifting electrons in the C_{60} layer lower the EA assigned to C_{60} located under 560 nm. The negative feature at 590 nm, assigned to Cy3-P EA, does not show any decaying dynamics on the probed timescale. This evidences that the hole in Cy3-P stays at the interface and drifts on longer timescales. At low fluences, such as the ones used here, no transient absorption signal were detected, and therefore the electric field dynamics integrated over 500-560 nm probe wavelengths shown in the next paragraphs are assigned to the drift of electrons in the C_{60} layer.

The electric field dynamics are reconstructed from the EDA data (see Chapter 2). The dynamics presented in the following sections were measured at reverse applied bias and were normalized to the maximum number of extracted charges obtained via the following relation:

$$\Delta E_{max} = \frac{\int I_{photo}(t)dt}{C \cdot D} \qquad (4.1)$$

where C and D are the capacitance and the thickness of the sample, respectively. D was 50 nm. The capacitance was calculated for each sample from the ratio of the displacement current in the sample under an applied bias. The detailed derivation is found in Chapter 2, section 2.3.2 of this thesis. The number of charges extracted was determined from the integrated photocurrent over the first 10 μs as $\int I_{photo}(t)dt$ after the excitation pulse.[56]

The amplitude of the electric field decay $\Delta E / \Delta E_{max}$ at any time after pump pulsed excitation (time zero) can thus directly be related to a percentage of total number of extracted electrons. The larger the negative amplitude, the more electrons extracted. The signal should eventually reach -1, indicating all electrons are extracted.

As mentioned in section 4.4.1, free charge carrier generation in neat C_{60} occurs for excitation wavelengths below 530 nm and an external applied field (see Figure 4.12).[42] This is observed in photocurrent data shown in Figure 4.19,
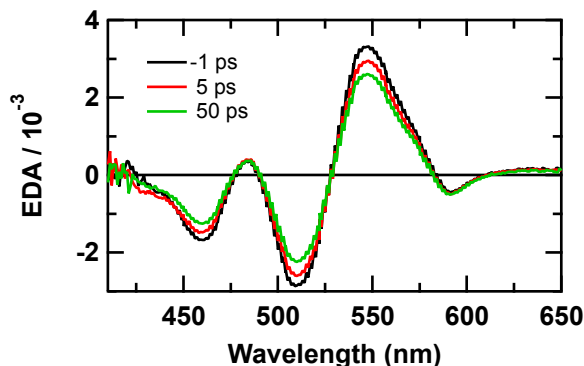

Figure 4.18 EDA spectra of a Cy3-P/C_{60} (20/30) bilayer at different time delays after 575 nm excitation (Fluence: 0.2 μJ/cm^2, for 4V applied bias).

where charge generation appears to be linear with the applied field. Cy3-P/C_{60} bilayers on the other hand, show a diode behaviour with saturation of the photocurrent for a bias voltage larger than 2 V (0.4 MV/cm) at 575 nm pump excitation. At 390 nm excitation, free charge carrier generation in the bilayer is dominating the carrier generation. The different active layer thickness used in Figure 4.19 explain the different photocurrent values obtained. To be noted, in solar cell operating conditions, field assisted charge carrier generation in neat C_{60} devices is poor due to smaller bias existing.
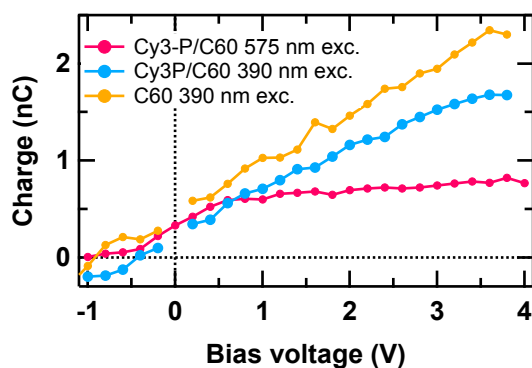
Figure 4.19 Integrated photocurrent as a function of applied bias voltage for a) C_{60} 80 nm thin film and b) Cy3-P/C_{60} (20/30) bilayer at 575 nm and 390 nm excitation. (Fluence: 0.2 and 0.7 μJ/cm^2, respectively).

390 nm excitation

The electric field dynamics following 390 nm excitation in the various devices are shown in Figure 4.20. For neat C_{60}, charge carriers are extracted from the 50 nm film within 4 ps. This is consistent with high charge carrier mobility for both electrons and holes. Bilayers show a similar ultrafast decay, assigned to free carrier generation in the bulk of C_{60} and subsequent electron drift to the electrode. The slower decay is assigned to interfacial charge separation, which expands over the C_{60} exciton diffusion lifetime of about 1.2 ns.[29] Indeed, the C_{60} excitons can diffuse over 20-40 nm during their lifetime.[57] Therefore, a thicker C_{60} layer yields a larger contribution of the slow decay.
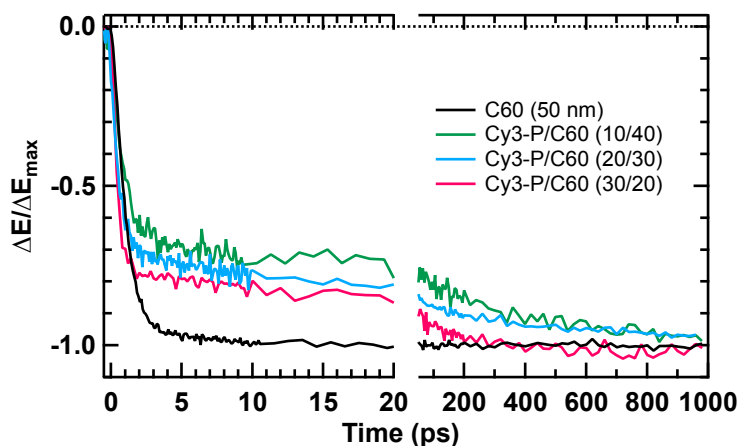
Figure 4.20 Electric field dynamics recorded after 390 nm excitation averaged over 60 nm probe wavelengths (500-560 nm), fluence = 0.7 μJ/cm^2, applied bias voltage = 2 V. The total sample thickness is kept constant (50 nm) to ensure similar and homogeneous electric field applied.

575 nm excitation

When Cy3-P is selectively excited at 575 nm, the dynamics show an even slower decay displayed in Figure 4.21. The electrons drifting in C_{60} in this case originate from dissociation of interfacial charge transfer states created from the Cy3 exciton. The slower decay may at first glance be assigned to the exciton diffusion to the interface, as no field-assisted charge generation is observed at
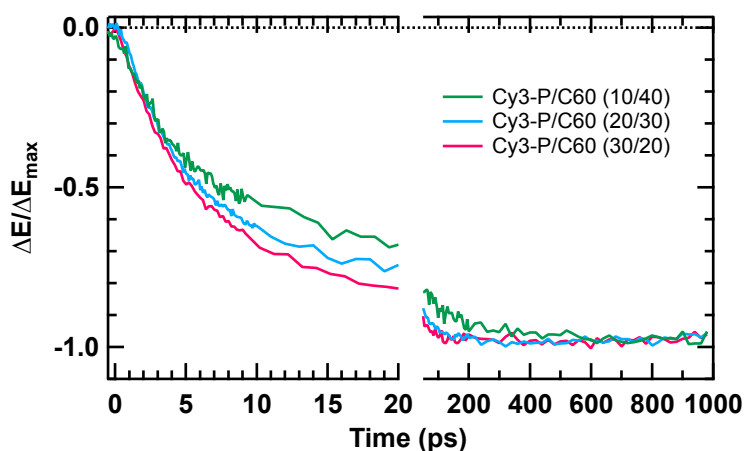

Figure 4.21 Electric field dynamics recorded after 575 nm excitation averaged over 60 nm probe wavelengths (500-560 nm), fluence = 0.7 μJ/cm^2, applied bias voltage = 2 V.
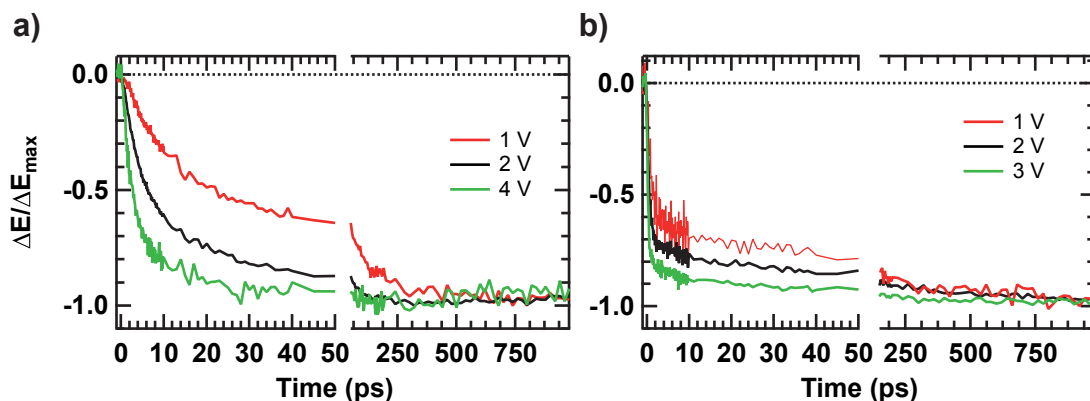
Figure 4.22 Electric field dynamics in the C_{60} layer of a Cy3-P/C60 (20/30) bilayer device at different applied bias voltages for a) 575 nm excitation (0.2 μJ/cm^2) and b) 390 nm excitation (0.7 μJ/cm^2) wavelengths.

575 nm excitation. However, the exciton lifetime in bilayers is mostly quenched on ultrashort (fs) timescales compared to the tens of picoseconds decay observed here (see section 4.3). An increase in applied bias voltage leads to a faster decay in Figure 4.22 a, which further proves that exciton diffusion is not the rate-limiting factor. Indeed, in small molecules like Cy3-P, excitons are neutral particles, that cannot be dissociated with a field. We already know that electrons in C_{60} drift through 50 nm within 4 ps under 2 V applied bias (Figure 4.20). In the bilayer, the electron drift is still fast (under 10 ps) even when the bias voltage is varied from 1 to 4 V as Figure 4.22 b shows. This indicates that the bias dependent electric field dynamics presented in Figure 4.22 a cannot be assigned to the electron drift in C_{60} neither. We can thus fully ascribe the slow decay observed in Figure 4.21 to the dissociation of a Coulombically bound interfacial CT state on tens to hundreds of ps. This bound interfacial CT state requires an applied electric field to separate into drifting free charges. As dissociation occurs on long time delays, we suggest that free charge separation occurs from relaxed interfacial CT states, even though creation of the CT state originated from hot Cy3-P excited states.

4.6 Conclusions

Ultrafast photoinduced processes in Cy3-P and C_{60} have been investigated separately, as well as in the bilayer. For neat Cy3-P films, the photophysics differ substantially from that of Cy3-B described in Chapter 3. The borate counter-anion reductively quenches the Cy3 excited state, which is not observed here in the Cy3-P ion pair. Instead, the excited state dynamics are entangled with ground state absorbance and we speculate that a low lying charge transfer state is populated on tens of picoseconds. It is very likely that the disordered structure of the film leads to dimers and H-aggregates, helping the charge transfer process. In neat C_{60} films, both the delocalized (intermolecular) charge transfer state and Frenkel exciton (intramolecular) are observed. We have shown that the delocalized CT state localizes mostly on 360 fs, to either an intramolecular CT, or the Frenkel exciton. This process is of major importance as electron delocalization fullerene has been suggested in ultrafast charge carrier generation in polymer:fullerene blends.[13]

Dipoles due to photogenerated charge transfer states, which can be delocalized over neighboring molecules, affect the surrounding molecules in a non negligible way. They cause a shift or splitting of the absorbance spectra, which then appears as a transient effect. This photoinduced Stark effect can be verified by steady-state electroabsorption, where the organic material is sandwiched between two electrodes, and undergoes an external applied electric field. Obviously, this effect overlaps with other transient absorption signals. In C_{60}, the photoinduced Stark effect shows very clear signals in TA spectra, even at low fluences. This has not been reported systematically in all time-resolved studies, therefore we suggest that steady-state electroabsorption measurements should be complementary to transient absorption investigations.

In Cy3-P/C_{60} bilayers, electron transfer occurs mostly on ultrafast timescales (<130 fs) from Cy3-P hot excited state. Minor slower electron injection is also observed on tens of ps timescale, occurring from more relaxed excited states.

Electron transfer results in a bound interfacial CT state that does not dissociate even up to the ns timescale. The interfacial CT state is evidenced by EA signatures of C_{60} upon electron transfer.

Hole transfer to Cy3-P from photoexcited C_{60} is observed on ultrashort timescales as well (<300 fs). The initial result of hole transfer is probably a bound interfacial CT, as we observe enhancement of C_{60} EA in the bilayer versus neat C_{60}. Delayed hole transfer is not excluded. Oxidized Cy3-P is observed and has a lifetime of about 105 ps before its recombination back to the ground state. We speculate that the observation of oxidized Cy3-P upon hole transfer from photoexcited C_{60} could originate from electron delocalization in C_{60}, accessed through high energy photons as observed in neat C_{60}.

Time-resolved electroabsorption measurements demonstrate that slow interfacial CT dissociation is the rate limiting process in charge separation for Cy3-P/C_{60} bilayer solar cells. This is due to a large Coulomb attraction, which might be difficult to overcome in device operating conditions. Mainly, interfacial CT dissociation occurs due to electron drift in the fullerene C_{60}. This takes place on several ps, in accordance with high mobility already reported.[11] The hole in Cy3-P however stays at the interface during the 1 ns probe delay time.

Photopolymerization of C_{60} by controlled light exposure has shown that a larger distance between donor and acceptor in the bilayer of about 1 nm increases the EA features. The recombination dynamics are not affected by the polymerization though, indicating that 1 nm distance is not sufficient to avoid the Coulomb attraction. This is consistent with a Coulomb capture radius in organic materials of about 16 nm.

4.7 Methods

Substrates

Glass microscopic slides were cut (2x1.5 cm) and cleaned thoroughly prior to material deposition. After brush cleaning with Helmanex soap, the substrates were sonicated sequentially for five minutes with acetone, ethanol and finally isopropanol. The substrates were dried under compressed air, and placed in the plasma cleaner (Harrick Plasma) for 15 minutes.

Indium tin oxide (ITO) was purchased at Ossila (20 Ω/cm^2) and patterned in-home with HCl 25%, protecting the ITO with capton tape. Further cleaning was done as described in the upper paragraph. Samples from EMPA followed the same cleaning procedure, but the ITO was patterned and purchased at Geomatec (20 Ω/cm^2).

10 nm of MoO_3 (Alfa Aesar, 99.9995%) was deposited by sublimation in a vacuum chamber at a pressure $<10^{-5}$ mbar on ITO substrates for EDA experiments.

Materials

Cyanine dyes (1-Ethyl-2-[3-(1-ethyl-1,3-dihydro-3,3-dimethyl-2H-indol-2-ylidene)-1-propen-1-yl]-3,3-dimethyl-3H-indolium hexafluorophosphate) Cy3-P and Cy3-C were purchased at FEW Chemicals or synthesized at the Laboratory of Functional Polymers, EMPA. They were dissolved in tetrafluoroproanol (TFP, Aldrich, 98%) or chlorobenzene (Sigma-Aldrich, 99.8%) in an argon or nitrogen glovebox. Spin-coating of the solutions on plasma-cleaned substrates was done on a Laurell spin coater, with different speeds and concentrations yielding various film thicknesses ranging from 20 to 55 nm. C_{60} was purchased from Bucky-USA (99.5%) or SES-Research (99.5%) and evaporated through a shadow mask at a pressure 10^{-5} mbar or lower.

For full solar cell devices, 10 nm of MoO_3 (Alfa Aesar, 99.9995%) was deposited by sublimation in a vacuum chamber at a pressure $<10^{-5}$ mbar on ITO substrates for EDA experiments. The active layers were deposited as descried above. A 2 nm thick cathode buffer layer of tris(8- hydroxyquinoline) aluminium (Alq3, Sigma-Aldrich, 99.9995%) was deposited on top at a pressure $<10^{-5}$ mbar. Finally, silver was evaporated through a shadow mask.

The thickness of Cy3-P films were performed by profilometry (Ambios XP1) on samples coated on glass.

Photopolymerization of C_{60} during 16h was performed under N_2 atmosphere in a glovebox, where light from a Xe lamp adjusted to 1 sun with a powermeter (LOT Oriel) was directed from outside.

Transient absorption spectroscopy

Transient absorption spectra were recorded via femtosecond pump-probe spectroscopy based on the 778 nm output of an amplified Ti-sapphire laser (Clark-MXR, CPA-2001) with 150 fs pulses running at 1 kHz repetition rate. The pump beam was generated via a two-stage non-collinear optical parametric amplifier (NOPA), while the probe beam was a white light continuum (350-750 and 790-1020 nm) generated by a portion of the 778 nm passing through a continuously moving CaF_2 plate. The pump wavelength was set at 540 nm from the NOPA output, or 390 nm generated by second harmonic generation of the fundamental 778 nm beam passing through a BIBO. Visible and nIR probe wavelength were recorded in two different experiments, by changing the blaze grating from 500 to 800 nm and adapting the band pass filters accordingly. The probe beam was split before the sample into a signal and reference beam in order to account for intensity fluctuations. Both beams were recorded shot by shot with a pair of 163 mm spectrographs (Princeton instruments, SpectraPro 2500i) equipped with a 512 x 58 pixels back-thinned CCD (Hamamatsu S07030-0906) and assembled by Entwicklungsbüro Stressing, Berlin.

All spectra were corrected for the white-light chirp measured by Kerr gating and background noise. Global analysis by a multiexponential fit at different wavelengths (typically every 5 nm) enabled the dissociation of the various photophysical processes occurring. The associated spectra show the amplitude of the transient signal related to each time component.

The samples were analyzed in an argon water-free environment with a home-built chamber avoiding contact with ambient air (Quartz windows, UQG Optics).

Time-resolved electroabsorption spectroscopy

The EDA and EA spectra were measured in reflectance mode on full solar cell devices with a comparable setup as described for the TA experiments, with the probe beam passing through the ITO, the active layer and then being reflected off the silver electrode. The white light probe (400-700 nm) was generated in a 3 mm sapphire disc from the 778 nm output of an amplified femtosecond laser (the same as described in the TA section). The probe beam was split before the sample into a signal beam (focused on the sample and reflected off the silver electrode into the detector) and a reference beam reaching a second detector. The signal and reference were detected with a pair of 163 mm spectrographs (Andor Technology, SR163) equipped with a 512×58 pixels back-thinned CCD (Hamamatsu S07030-0906) and assembled by Entwicklungsbüro Stresing, Berlin. The electric field was modulated with a function generator (Tektronix AFG 2021). A square voltage pulse in reverse bias (100 μs duration) was applied at half the probe frequency of 1 kHz, and the reflected probe light was measured shot-by-shot in the presence and in the absence of electric field, averaged over 3000 shots. The photocurrent was measured with an oscilloscope through a 50 Ω load.

4.8 References

(1)   Liu, Y.; Chen, C.-C.; Hong, Z.; Gao, J.; Yang, Y. M.; Zhou, H.; Dou, L.; Li, G.; Yang, Y. *Sci Rep* **2013**, *3*, 3356.

(2)   Lloyd, M.; Anthony, J. *Materials Today* **2007**, *10*, 34–41.

(3)   Green, M. A.; Emery, K.; Hishikawa, Y.; Warta, W.; Dunlop, E. D. *Prog. Photovolt: Res. Appl.* **2014**, *22*, 701–710.

(4)   Shoaee, S.; Mehraeen, S.; Labram, J. G.; Brédas, J.-L.; Bradley, D. D. C.; Coropceanu, V.; Anthopoulos, T. D.; Durrant, J. R. *J. Phys. Chem. Lett.* **2014**, *5*, 3669–3676.

(5)   Kaake, L. G.; Zhong, C.; Love, J. A.; Nagao, I.; Bazan, G. C.; Nguyen, T.-Q.; Huang, F.; Cao, Y.; Moses, D.; Heeger, A. J. *J. Phys. Chem. Lett.* **2014**, *5*, 2000–2006.

(6)   Fan, B.; Araujo De Castro, F.; Heier, J.; Hany, R.; Nüesch, F. *Organic Electronics* **2010**, *11*, 583–588.

(7)   Wicht, G.; Bücheler, S.; Dietrich, M.; Jäger, T.; Nüesch, F.; Offermans, T.; Tisserant, J.-N.; Wang, L.; Zhang, H.; Hany, R. *Solar Energy Materials and Solar Cells* **2013**, *117*, 585–591.

(8)   Malinkiewicz, O.; Grancha, T.; Molina-Ontoria, A.; Soriano, A.; Brine, H.; Bolink, H. J. *Adv. Energy Mater.* **2012**, *3*, 472–477.

(9)   Mishra, A.; Behera, R. K.; Behera, P. K.; Mishra, B. K.; Behera, G. B. *Chem. Rev.* **2000**, *100*, 1973–2012.

(10)   Jenatsch, S.; Hany, R.; Véron, A. C.; Neukom, M.; Züfle, S.; Borgschulte, A.; Ruhstaller, B.; Nüesch, F. A. *J. Phys. Chem. C* **2014**, *118*, 17036–17045.

(11)   Kobayashi, S.; Takenobu, T.; Mori, S.; Fujiwara, A.; Iwasa, Y. *Applied Physics Letters* **2003**, *82*, 4581–4583.

(12)   Guldi, D. M.; Prato, M. *Accounts of chemical research* **2000**, *33*, 695–703.

(13)   Gélinas, S.; Rao, A.; Kumar, A.; Smith, S. L.; Chin, A. W.; Clark, J.; van der Poll, T. S.; Bazan, G. C.; Friend, R. H. *Science* **2014**, *343*, 512–516.

(14)   Bernardo, B.; Cheyns, D.; Verreet, B.; Schaller, R. D.; Rand, B. P.; Giebink, N. C. *Nat Comms* **2014**, *5*, 3245.

(15)   Gao, F.; Inganäs, O. *Phys. Chem. Chem. Phys.* **2014**.

(16)   Heier, J.; Steiger, R.; Nüesch, F.; Hany, R. *Langmuir* **2010**, *26*, 3955–3961.

(17)   Fan, B. High Performance Cyanine Solar Cells, EPFL Thesis, 2010, pp. 1–181.

(18)   Castro, F. A.; Benmansour, H.; Moser, J.-E.; Graeff, C. F. O.; Nüesch, F.; Hany, R. *Phys. Chem. Chem. Phys.* **2009**, *11*, 8886–8894.

(19)   Peckus, D.; Devižis, A.; Augulis, R.; Graf, S.; Hertel, D.; Meerholz, K.; Gulbinas, V. *J. Phys. Chem. C* **2013**, *117*, 6039–6048.

(20)   Lanzani, G. *The photophysics behind photovoltaics and photonics*; Wiley-VCH, 2012.

(21)   Cappel, U. B.; Feldt, S. M.; Schöneboom, J.; Hagfeldt, A.; Boschloo, G. *J. Am. Chem. Soc* **2010**, *132*, 9096–9101.

(22)   Ardo, S.; Sun, Y.; Staniszewski, A.; Castellano, F. N.; Meyer, G. J. *J. Am. Chem. Soc* **2010**, *132*, 6696–6709.

(23)   Chekalin, S. V.; Yartsev, A. P.; Sundström, V. *Quantum Electron.* **2007**, *31*, 395–397.

(24)   Cabanillas-Gonzalez, J.; Virgili, T.; Gambetta, A.; L Lüer; Lanzani, G.; Anthopoulos, T.; de Leeuw, D. *Phys. Rev. B* **2007**, *75*, 045207.

(25)   Drori, T.; Holt, J.; Vardeny, Z. V. *Phys. Rev. B* **2010**, *82*, 075207.

(26)   Stevens, M.; Silva, C.; Russell, D.; Friend, R. *Phys. Rev. B* **2001**, *63*, 165213.

(27)   Jia, K.; Wan, Y.; Xia, A.; Li, S.; Gong, F.; Yang, G. *J. Phys. Chem. A* **2007**, *111*, 1593–1597.

(28)   Kato, T. *Laser Chem* **1994**, *14*, 155–160.

(29)   Sauve, G.; Dimitrijevic, N. M.; Kamat, P. V. *The Journal of Physical Chemistry* **1995**, *99*, 1199–1203.

(30)   Ebbesen, T. W.; Mochizuki, Y.; Tanigaki, K.; Hiura, H. *Europhys. Lett.* **1994**, *25*, 503–508.

(31)   Cook, S.; Ohkita, H.; Durrant, J. R.; Kim, Y.; Benson-Smith, J. J.; Nelson, J.; Bradley, D. D. C. *Applied Physics Letters* **2006**, *89*, 101128.

(32)   Cook, S.; Katoh, R.; Furube, A. *J. Phys. Chem. C* **2009**, *113*, 2547–2552.

(33)   Bakulin, A. A.; Hummelen, J. C.; Pshenichnikov, M. S.; van Loosdrecht, P. H. M. *Adv. Funct. Mater.* **2010**, *20*, 1653–1660.

(34)   Paraecattil, A. A.; Banerji, N. *J. Am. Chem. Soc* **2014**, *136*, 1472–1482.

(35)   Jeglinski, S.; Vardeny, Z. V.; Moses, D.; Srdanov, V. I.; Wudl, F. *Synthetic Metals* **1992**, *50*, 557–563.

(36)   Kazaoui, S.; Minami, N.; Tanabe, Y.; Byrne, H. J.; Eilmes, A.; Petelenz, P. *Phys. Rev. B* **1998**, *58*, 7689.

(37)   Sebastian, L.; Weiser, G.; Bässler, H. *Chemical Physics* **1981**, *61*, 125–135.

(38)   Chekalin, S. V.; Yartsev, A. P.; Sundström, V. *J. Exp. Theor. Phys.* **2001**, *93*, 706–716.

(39)   Cabanillas-Gonzalez, J.; Grancini, G.; Lanzani, G. *Adv. Mater.* **2011**, *23*, 5468–5485.

(40)   Drori, T.; Sheng, C.-X.; Ndobe, A.; Singh, S.; Holt, J.; Vardeny, Z. V. *Phys. Rev. Lett.* **2008**, *101*, 037401.

(41)   Dick, D.; Wei, X.; Jeglinski, S.; Benner, R.; Vardeny, Z.; Moses, D.; Srdanov, V.; Wudl, F. *Phys. Rev. Lett.* **1994**, *73*, 2760–2763.

(42)   Burkhard, G. F.; Hoke, E. T.; Beiley, Z. M.; McGehee, M. D. *J. Phys. Chem. C* **2012**, *116*, 26674–26678.

(43)   Cook, S.; Ohkita, H.; Kim, Y.; Benson-Smith, J. *Chemical Physics Letters* **2007**, *445*, 276–280.

(44)   Clements, A. F.; Haley, J. E.; Urbas, A. M.; Kost, A.; Rauh, R. D.; Bertone, J. F.; Wang, F.; Wiers, B. M.; Gao, D.; Stefanik, T. S.; Mott, A. G.; Mackie, D. M. *J. Phys. Chem. A* **2009**, *113*, 6437–6445.

(45) Zhang, H.; Borgschulte, A.; Castro, F. A.; Crockett, R.; Gerecke, A. C.; Deniz, O.; Heier, J.; Jenatsch, S.; Nüesch, F.; Sanchez-Sanchez, C. *Adv. Energy Mater.* **2014**.

(46) Li, Z.; Wong, H. C.; Huang, Z.; Zhong, H.; Tan, C. H.; Tsoi, W. C.; Kim, J.-S.; Durrant, J. R.; Cabral, J. T. *Nat Comms* **2013**, *4*, 2227.

(47) Dzwilewski, A.; Wagberg, T.; Edman, L. *Phys. Rev. B* **2007**, *75*.

(48) Grancini, G.; Maiuri, M.; Fazzi, D.; Petrozza, A.; Egelhaaf, H.-J.; Brida, D.; Cerullo, G.; Lanzani, G. *Nat Mater* **2013**, *12*, 29–33.

(49) Burke, T. M.; McGehee, M. D. *Adv. Mater. Weinheim* **2014**, *26*, 1923–1928.

(50) Provencher, F.; Bérubé, N.; Parker, A. W.; Greetham, G. M.; Towrie, M.; Hellmann, C.; Côté, M.; Stingelin, N.; Silva, C.; Hayes, S. C. *Nat Comms* **2014**, *5*, 4288.

(51) Bakulin, A. A.; Rao, A.; Pavelyev, V. G.; van Loosdrecht, P. H. M.; Pshenichnikov, M. S.; Niedzialek, D.; Cornil, J.; Beljonne, D.; Friend, R. H. *Science* **2012**, *335*, 1340–1344.

(52) Amarasinghe Vithanage, D.; Devižis, A.; Abramavičius, V.; Infahsaeng, Y.; Abramavičius, D.; MacKenzie, R. C. I.; Keivanidis, P. E.; Yartsev, A.; Hertel, D.; Nelson, J.; Sundström, V.; Gulbinas, V. *Nat Comms* **2013**, *4*, 2334.

(53) Vandewal, K.; Albrecht, S.; Hoke, E. T.; Graham, K. R.; Widmer, J.; Douglas, J. D.; Schubert, M.; Mateker, W. R.; Bloking, J. T.; Burkhard, G. F.; Sellinger, A.; Fréchet, J. M. J.; Amassian, A.; Riede, M. K.; McGehee, M. D.; Neher, D.; Salleo, A. *Nat Mater* **2014**, *13*, 63–68.

(54) Gulbinas, V.; Kananavičius, R.; Valkunas, L.; Bässler, H. *Phys. Rev. B* **2002**, *66*, 233203.

(55) Devižis, A.; Hertel, D.; Meerholz, K.; Gulbinas, V.; Moser, J. E. *Organic Electronics* **2014**, *15*, 3729–3734.

(56) Kniepert, J.; Schubert, M.; Blakesley, J. C.; Neher, D. *J. Phys. Chem. Lett.* **2011**, *2*, 700–705.

(57) Hedley, G. J.; Ward, A. J.; Alekseev, A.; Howells, C. T.; Martins, E. R.; Serrano, L. A.; Cooke, G.; Ruseckas, A.; Samuel, I. D. W. *Nat Comms* **2013**, *4*, 2867.

Chapter 5
Microstructure control for charge generation in polymer:fullerene blends
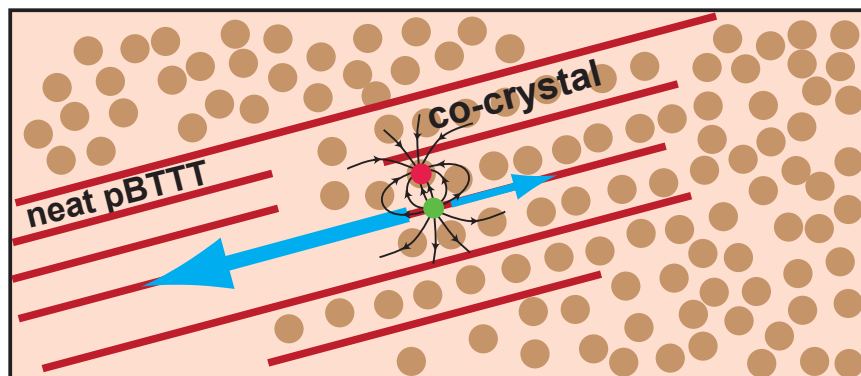
5.1. Introduction

Organic photovoltaics (OPV) have reached beyond 10 % efficiency lately, providing not only low-cost solutions but also diversified applications due to their flexibility and low-weight compared to inorganic solar cells.[1,2] Among criteria that predict a good solar to energy conversion efficiency in OPV systems, we find good solution processing properties, enhanced light absorption, high charge carrier generation and high charge carrier mobility. The latter two are not trivial, as organic semiconductors such as polymers may photogenerate bound electron-hole pairs with smaller charge carrier mobility than inorganic semiconductors. Charge carrier generation has been improved by introducing the electron donor/acceptor concept, energetically driving the electron-hole pair apart against their binding energy. Interpenetrated networks of donor and acceptor called bulk heterojunctions (BHJ) increase the interfacial area for charge carrier generation. Nonetheless, the BHJ microstructure has recently been revealed to be quite complex, and the mechanism of charge generation is still unclear.[3,4] Whether the charges are generated on ultrashort time scales by hot states, delocalized excited states, delocalized charges or due to high local mobility; [5-9] or slower via the charge transfer state[10,11] is under thorough debate. Subsequent charge transport on the nanoscale toward the electrodes is also of interest. Recent investigations have shown that polymer charge carrier mobility is time-dependent on ultrafast time scales.[12,13] It is thus of paramount interest to understand the fundamental mechanisms behind solar energy conversion by combining measurements in open circuit conditions and under an externally applied electric field.

These various statements show the need for case studies. A way to achieve this is by controlling the microstructure of the donor/acceptor heterojunction, which in turn directly govern the charge generation mechanism and transport. Multiple studies have investigated the processing methods that influence microstructure,

and enabled higher device performances.[14,15] Buchaca et al. employed fatty acid methyl ester additives to control the microstructure in polymer:fullerene blends from fully intercalated, to partially and predominantly non-intercalated systems.[16] The polymer used is poly(2,5-bis(3-alkyl-thiophene-2-yl)thieno[3,2-b]thiophene (pBTTT) and is mostly known for field effect transistors due to its high hole mobility.[17-19] When blended with the fullerene [6,6]- phenyl C_{61}-butyric acid methyl ester (PCBM) on a 1:1 weight ratio, the fullerene intercalates into the side chains of the polymer to form a co-crystal phase, as shown in Figure 5.1 a.[16] An excess of PCBM yields a PCBM rich region in addition to the co-crystalline phase (1:4 sample, Figure 5.1 b). By using Me12 or Me14 in 1:1 blends (structure shown in Figure 5.1), PCBM is successfully expelled out of the
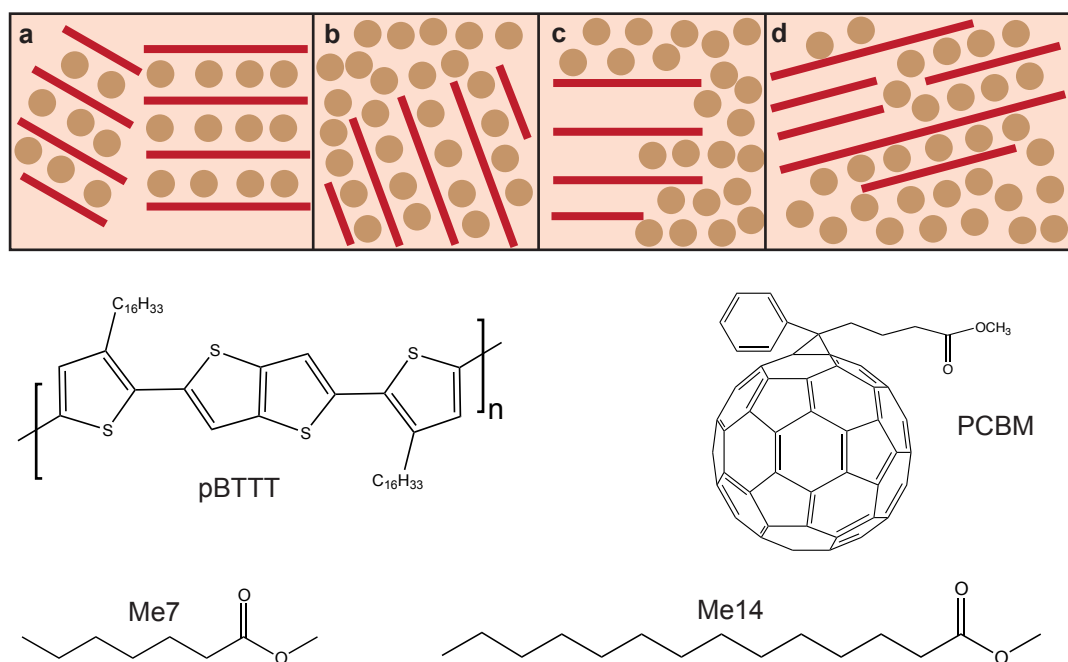
Figure 5.1 Microstructure scheme of the various pBTTT:PCBM blends: a) is a pure co-crystal phase, such as the 1:1 blend; b) is a co-crystal phase with excess PCBM, as in 1:4 blend; c) indicates de-intercalation yielding two mainly pure pBTTT and PCBM domains by the use of long additives such as Me12 and Me14 in the 1:1 blend; and finally d) is a three-phase microstructure achieved by the use of Me7 in the 1:1 blend. This picture is not to scale and serves as a basis for the understanding of photoinduced processes. More details about structural data can be found in Buchaca et al (ref 16). The molecular structures of the investigated materials are shown at the bottom of the Figure.

pBTTT side chains, leading to relatively pure phase regions as depicted in Figure 5.1 c. A shorter alkyl chain, such as the additive Me7, leads to a three phase region: the co-crystal phase, neat pBTTT and PCBM clusters (Figure 5.1 d). With these well-defined microstructures, we aim to investigate the dynamics of electron and hole transfer, and the subsequent charge transport through the active layer on ultrafast timescales. We use ultrafast transient absorption and transient Stark shift spectroscopy and part of the results presented in this Chapter are taken from a publication: "A close look at charge generation in polymer:fullerene blends with microstructure control" by M. Scarongella, J. De Jonghe-Risse, E. Buchaca-Domingo, M. Causa', Z. Fei, M. Heeney, J.-E Moser, N. Stingelin and N. Banerji, *Journal of the American Chemical Society*, 137, 2908-2918, 2015. Transient absorption measurements were carried out by M. Scarongella, and they are used here with permission to introduce the transient Stark effect data.[20] The author carried out electroabsorption and transient Stark effect spectroscopy measurements. Samples were prepared by E. Buchaca.

5.2. Microstructure

Grazing-angle incidence wide-angle X-ray scattering, among other techniques, has shed light into the intercalation of PCBM into pBTTT side chains.[16] More routinely accessible, the change in steady-state absorption spectra in Figure 5.2 actually easily reflects the various microstructures obtained with the use of additives or excess PCBM. Neat pBTTT shows a featureless absorbance with a maximum around 525 nm. Neat PCBM shows little absorbance in the visible, and increasing in the UV region. The intercalation of PCBM into pBTTT side chains in the 1:1 blend is evidenced by the vibronic progression and red-shift in absorbance compared to neat pBTTT (see structure of the co-crystal phase in Figure 5.1 a).[21,22] The excess PCBM in the 1:4 blend is indicated by an increase in the UV absorbance, assigned to the two-phase
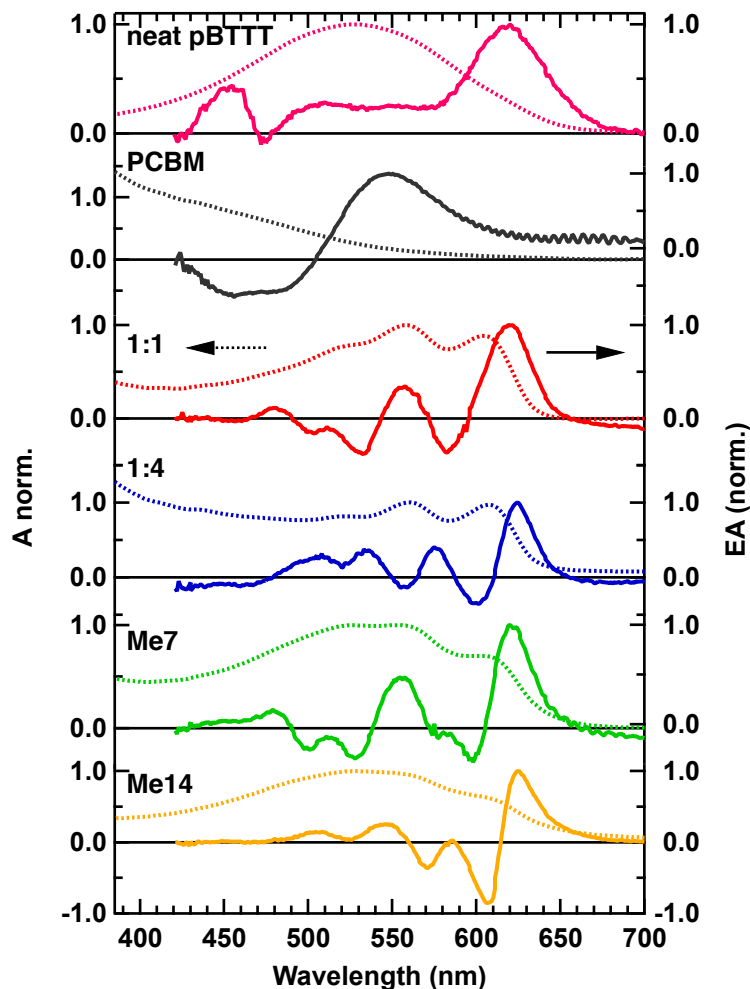
Figure 5.2 Steady-state absorption spectra for the various investigated samples (left axis) and corresponding electroabsorption spectra measured under 0.6MV/cm externally applied electric field (right axis).

system: intercalated co-crystal phase, and PCBM clusters (Figure 5.1 b).[21] The use of Me7 additive in the 1:1 blend (sample called Me7 throughout the text) leads to partial fullerene intercalation into the pBTTT side chains, as depicted in the three phase microstructure in Figure 5.1 d. The co-existence of a neat pBTTT phase and co-crystal phase leads to an intermediate absorbance spectra between neat pBTTT and 1:1 blend for the Me7 sample (Figure 5.2). The use of longer additives such as Me14 in the 1:1 blend (sample called Me14 throughout the text) fully expelled the fullerene out of the polymer side chains, evidenced by a less structureled absorbance around 540 nm due to pBTTT pure domains. Therefore, Me14 is essentially phase separated (Figure 5.1 c).

The apparent decrease in PCBM absorption for the Me14 blend is assigned to long-range ordering of neat PCBM regions.[23] These pure domains are larger than those obtained in Me7 sample, although exact values of domain sizes are not straightforward to obtain. Upon film dissolution in chlorobenzene, the fullerene absorption was recovered, excluding any fullerene loss during processing (not shown).[24]

The corresponding electroabsorption (EA) spectra for the various samples was measured at 6V externally applied bias voltage and are shown on the right axis of Figure 5.2. EA of neat PCBM (C_{60} derivative) is very similar to the spectra obtained for C_{60} shown in Chapter 4.[13] Neat pBTTT shows a rather flat EA spectra with a main peak at the absorbance edge, around 620 nm. All blends show a clear contribution of pBTTT EA between 620-630 nm, but more complex EA at wavelengths below 610 nm where both materials show EA in the pure devices.

5.3. Charge generation in pBTTT:PCBM blends

5.3.1. Excited state dynamics in pBTTT and blends with PCBM

Prior to investigating charge generation in pBTTT:PCBM blends, the transient absorption (TA) dynamics in neat pBTTT are discussed (Figure 5.3 a). The initial broad ground state bleaching (GSB) centered at 530 nm and excited state absorption (ESA) at wavelengths above 640 nm peaking toward 1000 nm are present in the 0.2 ps TA spectrum. They display multiphasic decay, attributed to the polydispersity of the polymer. Indeed, multiple polymer chain lengths induce disorder in the chromophore energy population. This is evidenced in the result of a multi-exponential global analysis (Figure 5.3 b) with a fast and a slower decay of 4.3 and 176 ps, respectively. Stimulated emission (SE) is also observed around 630 nm and causes an indent at 770 nm in the TA spectra. The

GSB already recovers with 4.3 ps time constant, indicating an ultrafast decay of pBTTT excitons. This is not due to high fluence effects ($< 8\,\mu J/cm^2$), and is corroborated by time-resolved fluorescence measurements in Figure 5.4. Here, the shorter wavelength emission dynamics (700 nm) decay faster than the red-side of the fluorescence spectrum (800 nm), indicating a red-shift in the emission on the ps timescale. This is also observed in the first (4.3 ps) amplitude spectrum in Figure 5.3 b with blue-sided SE. The 176 ps amplitude spectrum is more indicative of red-shifted SE. This emission shift is mostly assigned to energy transfer to low energy polymer chains. Long lived features in the weak amplitude spectra are assigned to charges and triplet states.[25]

The fullerene acceptor PCBM, when intermingled with pBTTT, successfully achieves to compete with this early relaxation as ultrafast emission quenching is observed on 130 fs and 110 fs for the 1:1 and 1:4 blend, respectively (inset of Figure 5.4). Me14 shows a multiphasic and slower emission quenching with respect to the 1:1 blend, but still faster than neat pBTTT (Figure 5.4). This indicates that exciton diffusion through neat domains limits the charge separation rate, and most likely delayed charge generation occurs in this sample.
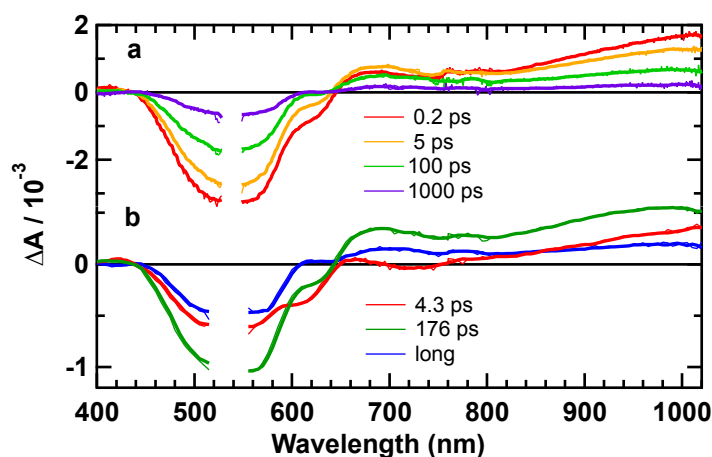

Figure 5.3 a) Transient absorption spectra at various time delays after 540 nm excitation for neat pBTTT, b) shows the amplitude spectra resulting from the best multi-exponential fit. Smoothed thicker lines are overlaid to the experimental amplitude spectra.
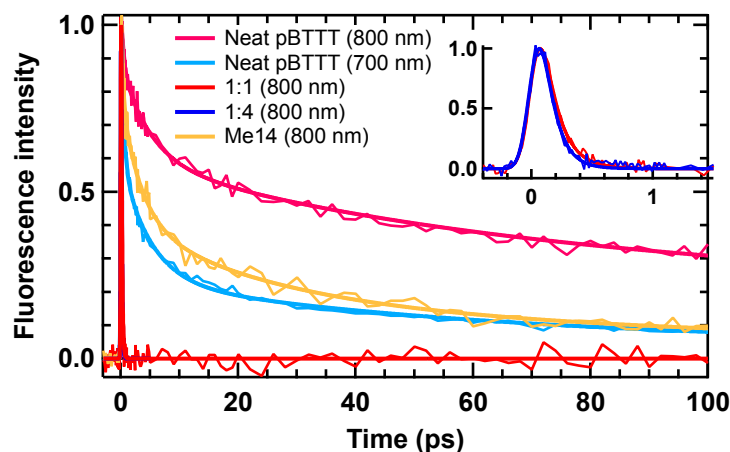
Figure 5.4 Time-resolved fluorescence dynamics recorded for 500 nm excitation for various samples, at probe wavelength as shown in the legend. Thicker lines represent the result of the best multi-exponential fit. Inset shows the early timescale dynamics for 1:1 and 1:4 blends.

5.3.2. Charge generation in intercalated pBTTT:PCBM blends

TA of 1:1 and 1:4 blends are shown in Figure 5.5 and 5.6, respectively. The complete analysis can be found in the work published by Scarongella et al., and are used with permission as they will guide our analysis of additive samples.[20] Two excitation wavelengths were used, in order to disentangle electron and hole transfer. While 540 nm excitation excites the polymer pBTTT only, 390 nm excitation is less selective but favors PCBM, as the absorption spectra indicates in Figure 5.2. Excitation fluences were adjusted to keep the number of absorbed photons constant ($<1.7\times10^{13}$photons/cm^2).

For both samples and excitation wavelengths, the structured GSB stems from excitation of the intercalated (co-crystal) phase, as already evidenced in the ground-state absorbance (Figure 5.2). The flat and broad absorbance above 640 nm is assigned to positive charges on pBTTT, created instantaneously after light excitation, that is within ≈ 100 fs (Figures 5.5 a,c and 5.6 a,c).[20,26,27] This explains the absence of ESA (absorbing toward 1000 nm) which is efficiently

quenched, as was already suggested by the time-resolved fluorescence measurements in Figure 5.4. The rise of PCBM GSB for wavelengths below 450 nm with 100 fs timescale in the amplitude spectra further corroborates the ultrafast electron injection for 540 nm excitation (Figures 5.5 b and 5.6 b). Similarly, polymer GSB rises with 100 fs time constant as well as a result from hole transfer after 390 nm excitation (Figures 5.5 d and 5.6 d).

A photoabsorption around 630 nm, associated to an oscillatory function in the 2.4 ps amplitude spectrum, is observed in the TA data of 1:1 and 1:4 blends (Figure 5.5 and 5.6). From the EA spectra shown in Figure 5.2, it is straightforward that this early oscillatory signal observed in TA measurements is associated to local electric fields in the sample leading to photoinduced electroabsorption due to the Stark effect. Local electric fields are induced by photogenerated charge carriers, delocalized excited states or even delocalized charge pairs.[28-33] We will come to the analysis of EA in TA data in more details in section 5.3.5, and we will for now focus our discussion on the charge generation dynamics.

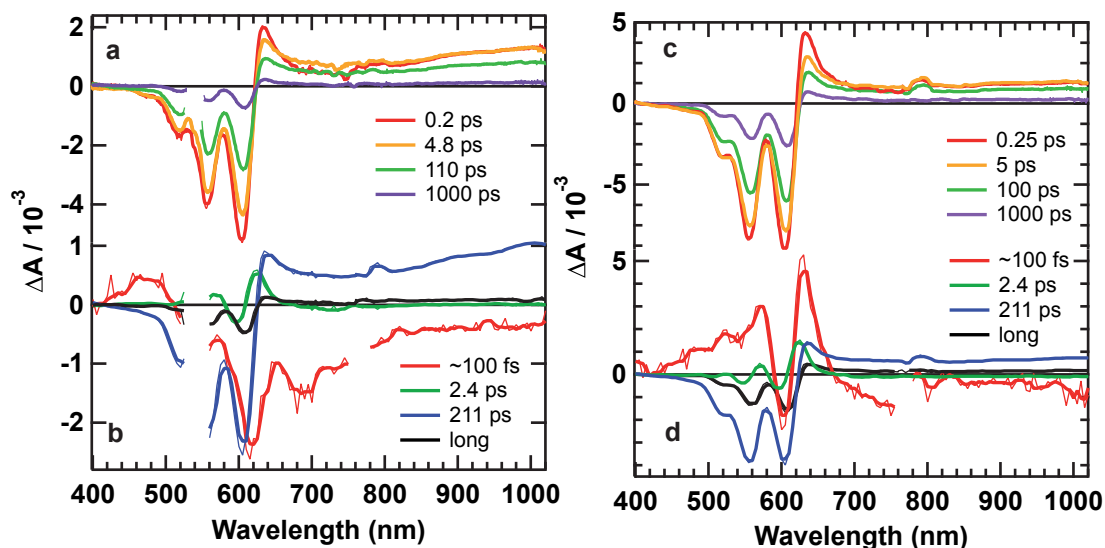In the 1:1 blend, geminate charge recombination is associated with the 211 ps

Figure 5.5 Transient absorption spectra for the 1:1 sample recorded at various time delays after a) 540 nm and c) 390 nm excitation. b) and d) are the corresponding amplitude spectra resulting from the multiexponential fit. Smoothed thicker lines are overlaid to the experimental amplitude spectra.

time constant in the amplitude spectra of Figure 5.5 b and d. Most charges generated recombine with this time scale for both excitation wavelengths. The weak signal at long time delays stems from a low fraction of free charges formed in this blend.

PCBM excess in the 1:4 blend forms clusters where the can electron escape from the co-crystal phase by energy cascade, stabilizing the electron by about 100-200 meV.[7,34] Prompt charge generation in the intercalated domains is observed for both excitation wavelengths in the 1:4 sample, as indicated by the flat absorption of charges for wavelengths above 640 nm. The electron and hole transfer rates for prompt charge generation are both ≈ 100 fs as the rise of polymer and PCBM GSB suggest in the amplitude spectra of Figure 5.6 b and 5.6 d, respectively. The amplitude associated to gCR is strongly reduced compared to the 1:1 sample due to PCBM clusters (Figure 5.5 and 5.6). Instead, long lived (free) charges are observed with delayed recombination rates (after 1 ns). Slower and multiphasic charge generation is also present for 390 nm excitation. This is associated to exciton diffusion in PCBM clusters, whose
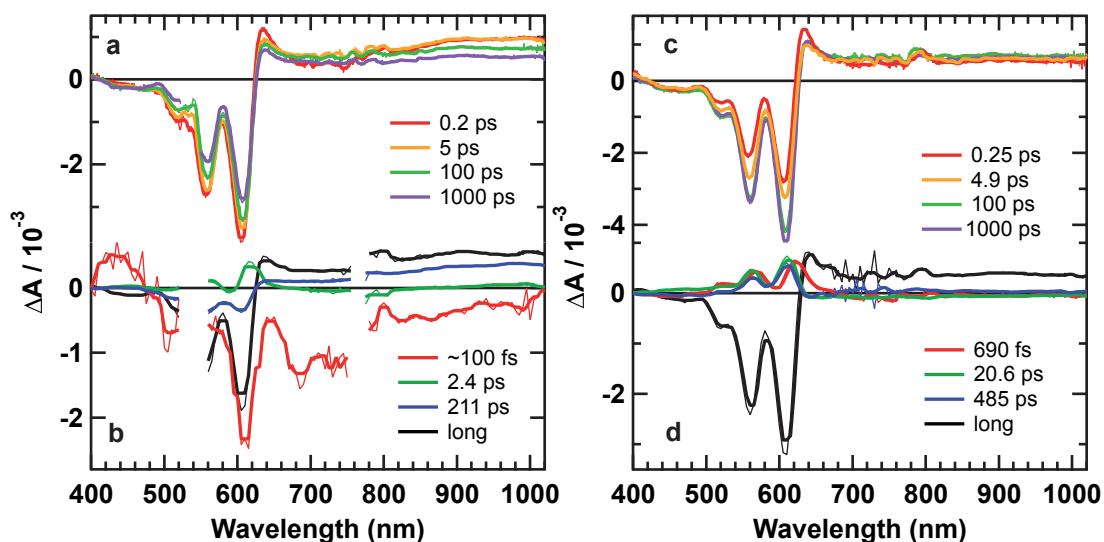

Figure 5.6 Transient absorption spectra for the 1:4 sample recorded at various time delays after a) 540 nm and c) 390 nm excitation. b) and d) are the corresponding amplitude spectra resulting from the multiexponential fit. Smoothed thicker lines are overlaid to the experimental amplitude spectra.

lifetime is about 1.2 ns.[35,36]

5.3.3. Charge generation in a partially intercalated blend with the use of Me7 (three phase system)

Processing the 1:1 blend with a fatty acid methyl ester additive such as Me7, whose structure is shown in Figure 5.1, yields a three-phase microstructure as depicted in Figure 5.1 d. While this could be observed in the steady-state absorbance spectra from Figure 5.2, this is also seen in the less structured GSB of TA data in Figure 5.7 a compared to the 1:1 blend (Figure 5.5 a). Obviously, multiphasic charge generation is expected for this sample at 540 nm excitation due to the presence of both intercalated and neat pBTTT domains. Indeed, prompt charge generation is observed as indicated by the flat absorption above 640 nm wavelength in the 0.2 ps TA spectrum, but ESA from pBTTT neat domains peaking toward 1000 nm is also present (Figure 5.7 a). Delayed charge generation takes place with 0.3 and 6.8 ps time constants as the rise in PCBM
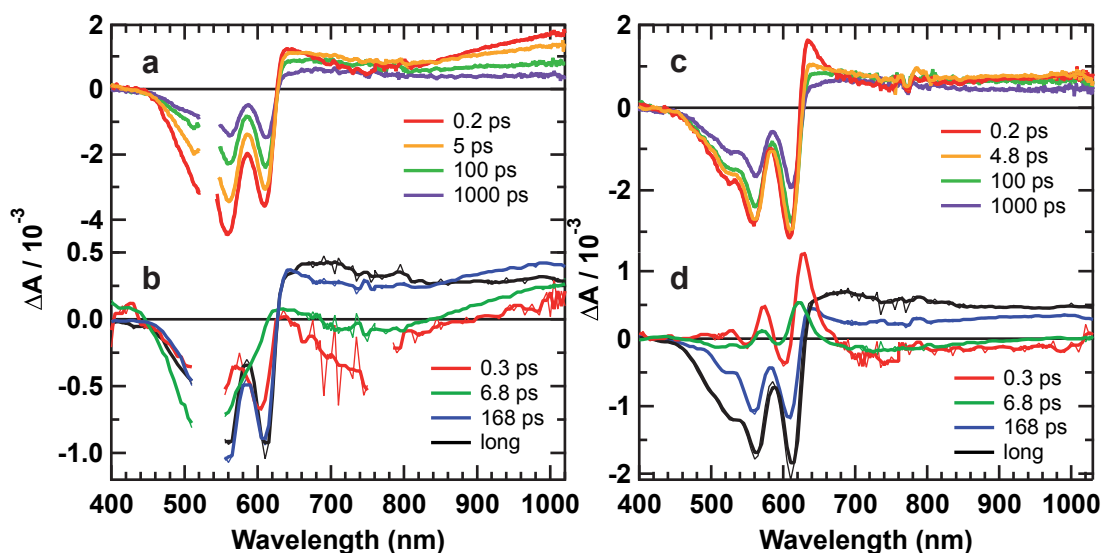

Figure 5.7 Transient absorption spectra for the Me7 sample recorded at various time delays after a) 540 nm and c) 390 nm excitation. b) and d) are the corresponding amplitude spectra resulting from the multiexponential fit. Smoothed thicker lines are overlaid to the experimental amplitude spectra.
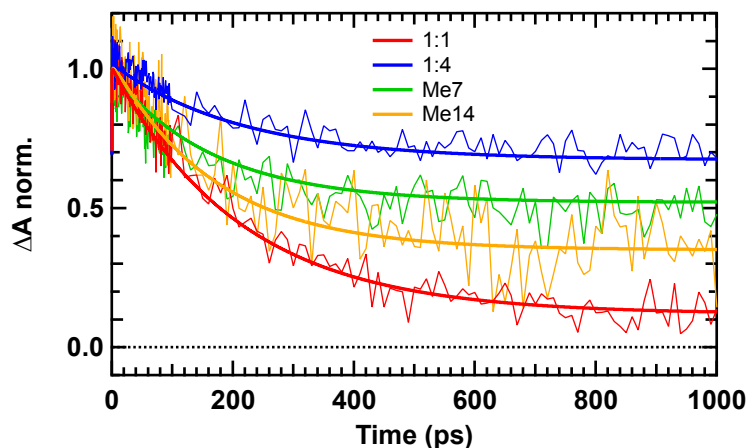
Figure 5.8 Normalized transient absorption dynamics recorded after 540 nm excitation for the various investigated samples at 850 nm probe (mainly charges). Thick solid lines are the result from the best multi-exponential fit

GSB for wavelengths below 450 nm suggests (Figure 5.7 b). Part of the pBTTT excitons are actually lost to the ground-state by recombination with 0.3 and 6.8 ps time constants, as GSB recovery and SE (around 730 nm)/ESA decay in the corresponding amplitude spectra suggest. Geminate charge recombination is not completely avoided by the presence of neat domains, associated with the 168 ps time constant due to spectral similarity with gCR in 1:1 and 1:4 blends. Nonetheless, at longer time delays, charge absorption is clearly larger than for the 1:1 blend (Figure 5.5 and 5.7), indicating that despite exciton loss and minor gCR, the charge recombination rate is slower thanks to the neat pBTTT domains. Actually, the dynamics probed at 850 nm shown in Figure 5.8 represent the charge recombination dynamics in the various samples. They clearly show that the use of Me7 reduces gCR compared to the 1:1 sample. Accordingly, a higher yield for free charge generation was observed with the use of Me7 in the 1:1 blend in another study.[16]

Similarly to 540 nm excitation, multiphasic charge generation due to exciton diffusion in PCBM is observed for 390 nm excitation in the amplitude spectra (Figure 5.7 d) with 0.3 and 6.8 ps time constants. Both pBTTT and PCBM are excited at this wavelength. Prompt charge generation is observed as the flat absorption above 640 nm implies, which recombination rate seems reduced

compared to that observed at 540 nm excitation (Figure 5.7 a and c). Most likely the decaying ESA together with multiphasic charge generation overlap at wavelengths above 640 nm, resulting in a weakly decaying transient signal. Hot charge generation due to a higher excitation energy is excluded here, as the yield of free charge carriers at long time delays is similar for both 540 and 390 nm excitations.[11,37]

5.3.4. Charge generation in a mainly phase-separated blend with the use of Me14

Additive with a longer alkyl chain such as Me14 favors fullerene expulsion from pBTTT side chains, leading to a predominantly two-phase microstructure (Figure 5.1 c). 540 nm excitation in Figure 5.9 a shows mainly the presence of pBTTT excitons from neat domains, in accordance with the less structured GSB observed. Time-resolved fluorescence revealed multiphasic exciton decay in this sample (Figure 5.4) and this is observed as well in the
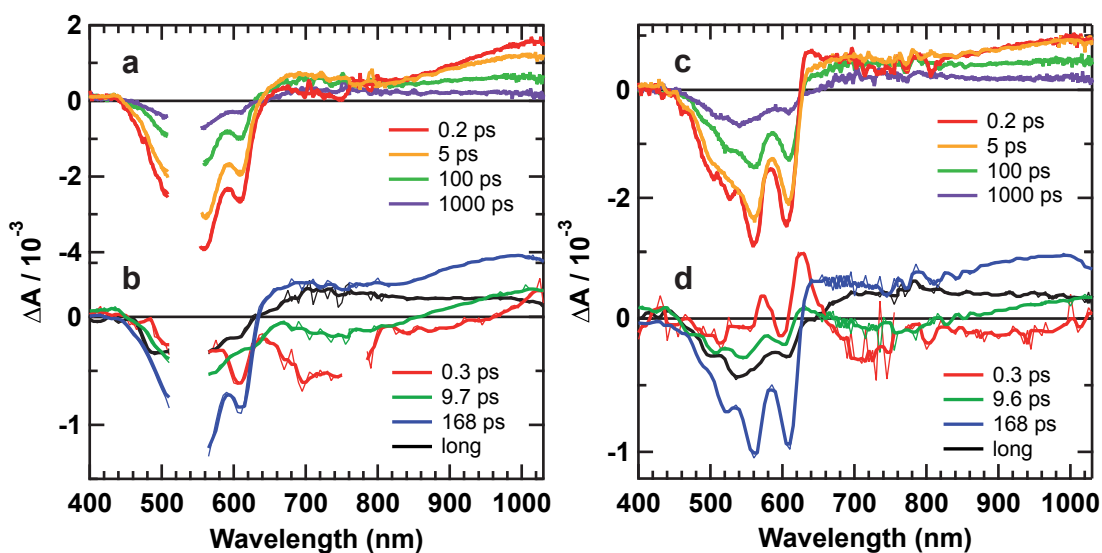

Figure 5.9 Transient absorption spectra for the Me14 sample recorded at various time delays after a) 540 nm and c) 390 nm excitation. b) and d) are the corresponding amplitude spectra resulting from the multiexponential fit. Smoothed thicker lines are overlaid to the experimental amplitude spectra.

amplitude spectra of Figure 5.9 b. Unlike the previous samples, the amplitude of charge absorption is small in Figure 5.9 a. The 168 ps amplitude spectra, usually assigned to gCR in the other blends, now indicates ESA decay peaking toward 1000 nm (Figure 5.9 b). The pBTTT domains are probably too large to avoid exciton loss.

390 nm excitation yields very similar TA features in Figure 5.9 c, as in this sample mostly the pBTTT absorbs at this wavelength (see Figure 5.2). Still, a more structured GSB points toward a more selective excitation of the co-crystal phase, even if there is little intermixed phase present in this sample. We will come back to that later.

The solar cell efficiency of Me14 sample is lower than for the Me7 sample, but still higher than the 1:1 blend. This is directly observed in the transient absorption dynamics at 850 nm (mainly charge absorption, Figure 5.8), where the 1:4 has the most long-lived charges, followed by Me7, Me14 and finally the 1:1 sample. This result highlights that the recombination dynamics at early timescales impact the solar cell efficiency of pBTTT:PCBM blends.

5.3.5. Electroabsorption (EA) dynamics

The oscillatory feature observed in the early time delay spectrum after 540 nm excitation of the 1:1 blend is due to EA of pBTTT as mentioned earlier. EA in transient absorption data has been reported several times for different systems such as dye-sensitized solar cells, polymer:fullerene blend films and neat fullerene films.[6,30,38-40] Local electric fields are induced by photogenerated charge carriers, delocalized excited states or even delocalized charge pairs.[28-33] Amongst various effects, the local electric fields induce a change in the transition dipole and/or polarizability of the surrounding molecules, which as a consequence shifts the transition energy of the investigated chromophore. This is called a Stark effect and is measured by tracking the change in absorbance upon voltage modulation. The resulting EA for the 1:1 blend is shown in Figure 5.2.

The oscillatory shape of EA is typical and can be decomposed into contributions from first and second order derivatives of the ground state absorbance (see Chapter 2 for more details). This goes beyond the scope of the work presented here, and we will concentrate on the origin of the EA in TA data for these particular pBTTT:PCBM blends. Figure 5.10 shows the striking similarity between EA, the 2.4 ps amplitude spectrum and first derivative of ground state absorbance of the 1:1 blend.

The electric fields generated around electron-hole pairs (dipole) and free charges, are schematically illustrated in Figure 5.11 for diverse microstructures such as in the neat pBTTT domain, co-crystal phase, and PCBM cluster.

In fully intercalated samples (co-crystal phase only, 1:1 sample), electron-hole pairs are generated mainly within 100 fs, and charge generation does not depend on excitation wavelength (i.e. polymer or fullerene excitation). The EA is observed in the 0.2 ps TA spectrum and decays weakly with a time constant of 2.4 ps (Figure 5.5 a and b, respectively). The EA component is still present at longer time delays in the TA spectrum. According to the crystal structure of 1:1 blends, the initial electron-hole pair is perpendicular to the polymer backbone (Figure 5.11).[41] The polymer backbones around this dipole are close enough to contribute to the EA observed. According to the electrostatic picture, the
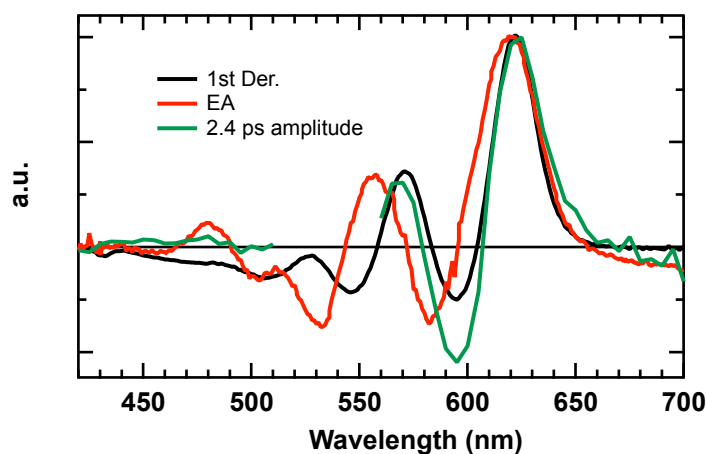

Figure 5.10 Absorption first derivative, Electroabsorption (from Figure 5.2), and 2.4 ps amplitude spectrum (from Figure 5.5 a, 540 nm excitation) for the 1:1 blend.
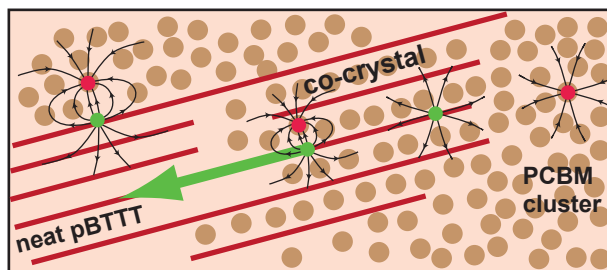
Figure 5.11 Schematic representation of the electric fields generated by charge pairs (dipoles) and free charges, depending on the microstructure: co-crystal phase, neat pBTTT and neat PCBM domains. The spacing between polymer backbones is 3 nm (lamellae). The π-stacking is above and below the plane shown here (see crystal structure in ref 41).

polymer segments above and below the dipole (along the π-stacking axis) and along the same polymer chain of the hole are affected by the electric field generated by the dipole. The lamellar stacks are separated by about 3 nm, and therefore are much less affected by the dipole electric field. If we assume a reasonable charge separation of 1 nm at early time scales, the strong EA observed already at the 0.2 ps time delay can be explained by using simple electrostatic calculations. The complete electrostatic derivation is detailed in reference 24. The weak EA decay associated with a 2.4 ps time constant is assigned to charge migration within the co-crystal phase, or charge relaxation.[24]

The initial EA signature is similar for the 1:4 blend for 540 nm excitation, as prompt charge generation occurs in the co-crystal region as in the 1:1 blend (Figure 5.6 a). But in this case, electron migration to PCBM clusters is favored due to an energy cascade toward higher electron affinity domains, and EA is still observed at long time delays (1 ns).[7,34] We have derived a similar electrostatic picture involving an electron in the PCBM cluster, and the hole remaining on the co-crystal phase. In fact, the less bound charges are no longer oriented perpendicular to the polymer backbone, but more along the polymer backbones and/or π-stacking as the electron will follow the fullerene direction parallel to the polymer π-stacking toward pure PCBM clusters (Figure 5.11). Indeed, polymer side chains and backbones hinder electron diffusion in fullerene in the other directions. This orientation change in addition to the longer separation

distance however yield very similar EA response to the initial dipole in the co-crystal region, with a minor weak decay associated with the 2.4 ps amplitude spectrum in the 1:4 blend. We can thus conclude that the EA signature observed in intercalated systems is due to either bound or free charges on the polymer chains, with minor contribution from the electron position (bound in the intercalated phase, or free in the PCBM cluster).

TA of Me7 sample at 540 nm excitation revealed prompt charge generation, but EA is less evident (Figure 5.7 a). The weak EA quickly decays and no oscillatory-like EA feature is observed in the corresponding amplitude spectrum for the first two time constants (Figure 5.7 b). As the yield of long-lived free charges is larger than for the 1:1 blend, we conclude that the charges generated at the interface of pure domains or in the co-crystal phase quickly migrate to neat pBTTT domains. Bound or free holes in neat pBTTT domains affect differently the surrounding polymer chains compared to pBTTT in the co-crystal phase. EA of pBTTT in neat domains has actually much lower amplitude than in the co-crystal phase, as suggested by Figure 5.12 b. EA demonstrates quadratic dependence on applied bias voltage in both cases, but the EA amplitude is much lower in neat pBTTT sample. We assign this to a broader and more flat absorbance in neat pBTTT compared to the co-crystal phase, as Figure 5.2 already indicates, leading to less effect of the electric field in neat pBTTT domains. Indeed, shifting a broad and unstructured absorbance gives rise to less sharp EA features compared to shifting a structured absorbance such as the co-crystal phase.

Delayed charge generation due to exciton diffusion in neat pBTTT to the interface with PCBM does not lead to a rise of EA in the TA data of Me7 sample (Figure 5.7 a and b), which corroborates that EA is fully assigned to the co-crystal nature of the polymer. Me14 does not show significant EA in TA data, in fact it mostly shows SE from neat pBTTT domains at early time delays (Figure 5.9 a). Delayed charge generation is not associated with a rise in EA as well (Figure 5.9 c). We thus assign the absence of EA to the nature of the pBTTT

domains where the hole is located: only co-crystal phase will show EA in TA data.

At 390 nm excitation for both Me7 and Me14, the excitation is more selective to co-crystal regions as observed from TA measurements. This is implied from a more structure GSB in Figure 5.7 c and 5.9 c compared to 540 nm excitation. Accordingly, the EA feature is enhanced compared to 540 nm excitation in the initial 0.2 ps spectrum and appears notably in the 0.3 ps amplitude spectra (compare Figures 5.7 b and d, Figures 5.9 b and d). The initial EA dynamics are represented by the dynamics at 630 nm probe in Figure 5.12 a. While the yield of free charge generation at long time delays does not depend on excitation wavelength (Figure 5.7 and 5.9), the fast decay upon 390 nm excitation implies that prompt charge generation is followed by hole migration to neat pBTTT domains on a timescale of about 1 ps. This is supported by the lack of charge absorption recovery (around 850 nm) on ultrafast time scales in the corresponding amplitude spectra (Figure 5.7 d and 5.9 d).

We can thus conclude that the EA observed in TA data stems from the position of the hole in the co-crystal regions, whose is more selectively excited at 390 nm. Gelinas et al. reported EA in TA data and assigned it to long-range separated charges by about 4 nm, and no EA was observed for bound charge pairs.[6] This is in contrast to our results, which show EA from bound and less bound charge
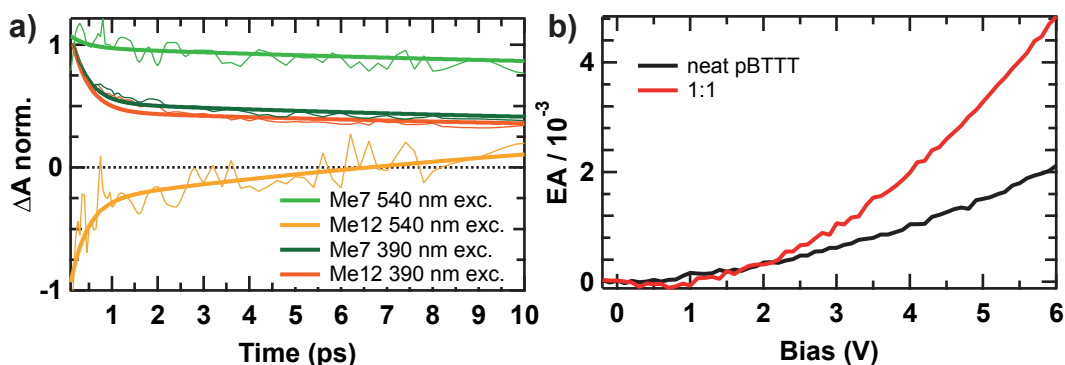

Figure 5.12 a) Transient absorption dynamics recorded for 540 and 390 nm excitation for Me7 and Me 12 (similar to Me14) blends at 630 nm probe wavelength. Thick solid lines are the result from the best multi-exponential fit. b) Quadratic dependence of the EA (at 620 nm probe) versus externally applied bias voltage. Neat pBTTT has a much weaker EA signature than the intercalated pBTTT (1:1).

pairs in the co-crystal phase only. We relate this to the more ordered structure of pBTTT:PCBM samples compared to the more amorphous samples from ref. 6.

In order to gain more insight into the charge carrier transport through the active layer on ultrafast timescales, time-resolved Stark measurements have been performed on the various samples. The results are shown in the next section.

5.4. Electric field dynamics: charge carrier generation and transport

High charge carrier generation yield followed by appropriate charge transport toward the electrodes are both crucial parameters for photovoltaic performance. Before going into the details of charge transport, we will overview the quasi steady-state charge collection efficiency. Photovoltaic devices were prepared by depositing the active layer between ITO and Al electrodes (see section 5.7 for details) and encapsulated by an epoxy resin.

5.4.1. Photon to current efficiency

The numbers of charge carriers extracted as a function of applied bias are shown in Figure 5.13 for the various investigated samples, corrected for the number of absorbed photons:

$$\text{Photon-to-Current}[\lambda_{exc}, V] = \frac{\int I_{photo}(t)dt}{e} \cdot \frac{hc}{\text{Fluence} \cdot \lambda_{exc} \cdot A_{ill} \cdot (1-T)} \qquad (5.1)$$

where e is the elementary charge, h is Planck's constant, c is the speed of light in vacuum, A_{ill} is the illuminated active area, T is the transmittance of the sample at the excitation wavelength λ_{exc} and V is the reverse applied bias. The constant
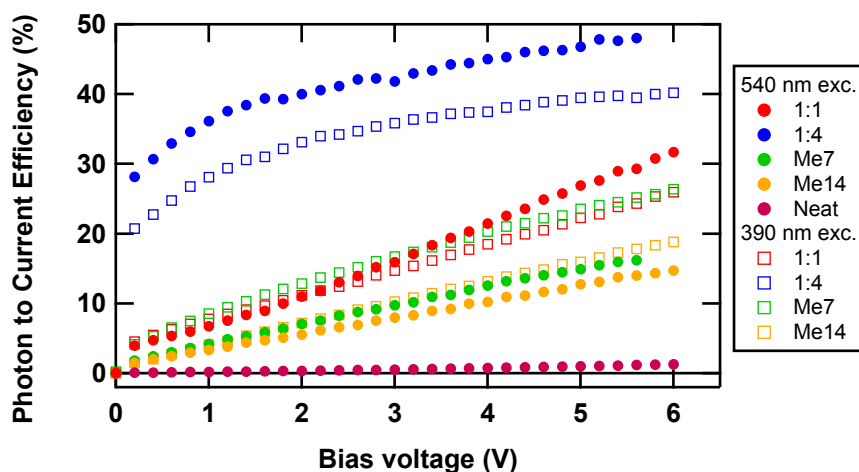
Figure 5.13 Photon to current efficiency under reverse bias voltage for different devices at two excitation wavelengths: 540 nm (mainly pBTTT) and 390 nm (pBTTT and PCBM). Neat pBTTT is shown as a comparison in pink round symbols. The excitation intensity was adjusted to have the same number of absorbed photons for both excitation wavelengths, $<3.10^{11}$ photons/cm^2.

values can be found in the list of abbreviations. The number of charges extracted was determined from the integrated photocurrent over the first 10 µs after the excitation pulse.[42,43] The number of absorbed photons was calculated from the fluence and absorbance of the sample at the excitation wavelength. The absorbance was taken from transmittance measurements and taking into account the 45° angle of the pump beam with respect to the active layer (see EA setup in Chapter 2, Figure 2.6). This is a rough estimation, but serves well the discussion here as all samples were measured in the same way. The photon to current efficiency values obtained (Figure 5.13) are in general smaller than expected, but can be explained easily due to the configuration of the setup (see Chapter 2, Figure 2.6 for a scheme of the setup). The reflection losses by the glass were not accounted for, nor the exact absorption profile within the active layer. This would easily step up the values obtained, nonetheless this would not change the trend observed here.

The 1:4 device definitely shows the highest efficiency in Figure 5.13, and this ratio is often the best for other polymer blends.[34,37,44,45] 540 nm excitation leads to quasi-saturation of charge carrier extraction after about 1 V of applied bias, with

a slower increase afterwards, reaching about 50% efficiency. This indicates that majority of the excitons are converted into extracted carriers. At 390 nm excitation, the efficiency is slightly lower over the bias scanned due to the exciton loss in the PCBM clusters.[34] Indeed, exciton diffusion can not be affected by an externally applied bias.

For the 1:1 blend, the slope is rather linear and the maximum does not reach more than about 30 %, indicating that high applied biases are needed to successfully dissociate bound charge pairs. The poor performance of the solar cell may be related to a prevailing geminate charge recombination mechanism. 390 nm excitation leads to similar results than 540 nm excitation. We assign this to the presence of the co-crystal phase, where charge generation is prompt and independent of excitation wavelength, without exciton loss. Dissociation of charge pairs in the co-crystal phase is however not favorable, but can be enhanced with the applied electric field. The decrease in efficiency after 3 V applied bias with 390 nm excitation is unclear at the moment, but experiments are carried out in the group of Prof. N. Banerji for confirmation. Nevertheless, the difference is minor and probably indicates that excess photon energy does not impact the number of charges extracted, for example via hot states.

The additive samples (Me7 and Me14) show a lower efficiency than 1:1 for 540 nm excitation assigned to exciton loss in pure pBTTT domains, according to our TA and time-resolved emission data. At 390 nm excitation however, slightly higher efficiency values are obtained for Me7 sample compared to the 1:1 blend. We relate this to selective excitation of the co-crystal domains according to our TA measurements, which efficiently generate bound charge pairs that will dissociate under high applied electric fields, and effectively avoid exciton loss due to large pure domains. Exciton loss is however not completely avoided in Me14 samples, as the low efficiency in Figure 5.13 indicates. This is due to larger pure fullerene and pBTTT domains in this sample, compared to Me7.[16,24]

As a comparison, neat pBTTT is also presented and indicates low photon to electron conversion efficiency, in good agreement with the poor photovoltaic performance of neat polymer solar cells.[46]

Bound charge pairs require electric fields to dissociate, as opposed to free charge carriers.[15] Moreover, traps encountered during charge transport through the active layer can be pulled out by electric fields. Both effects can lead to linear photon to current efficiencies. Additionally, poor conversion efficiency originating from exciton losses in pure domains lead to lower amounts of extracted charges. To get more insight into the charge carrier dynamics, time-resolved electroabsorption based on the Stark effect were performed on these samples.

5.4.2. Electric field dynamics

Charge transport dynamics on the nanoscale were monitored with time-resolved dynamic Stark shift spectroscopy. More details about the experimental setup can be found in section 5.7 and Chapter 2.3. Basically, the applied voltage pulse is modulated at half the frequency of the pump and probe pulses, and the obtained differential absorption spectra is the difference at a certain probe delay between a biased and unbiased sample.[13] The sample is thus a full solar cell device, i.e. an organic layer sandwiched between two electrodes. The photogenerated charge pairs will drift under the applied electric field toward their respective electrodes.

The steady-state electroabsorption (EA) spectra for the various investigated samples are shown in Figure 5.2. The obtained spectra for different blend ratios show mostly EA of the pBTTT polymer. The PCBM contribution is located for wavelengths below 610 nm, and therefore both PCBM and pBTTT contributions are intermixed for wavelengths below 610 nm. For this reason, the electric field dynamics calculated from time-resolved dynamic Stark shift spectroscopy shown in the next section are averaged over about 615-630 nm probe wavelengths, depending on the sample. The electric field in the device depends on the externally applied electric field at first, and the charge pairs' average distance as well as to their concentration after pump excitation.

In principle, the time of charge extraction depends on the exciton diffusion time, the rate of charge pair dissociation and the transport mode. Insight into the exciton diffusion time has been revealed by time-resolved fluorescence and transient absorption (see section 5.3). Exciton diffusion in pBTTT is not affected by the electric field, as negligible electric field decay was observed for neat pBTTT (not shown). This is in contrast with Pranculis et al., but we tentatively attribute this to the different electronic properties of pBTTT polymer compared to APFO₃.[44] The electric field dynamics presented in the following were measured at 4V reverse applied bias and were normalized to the maximum number of extracted charges obtained via the following relation:[43]

$$\Delta E_{max} = \frac{\int I_{photo}(t)\,dt}{C \cdot D} \qquad (5.2)$$

where C and D are the capacitance and the thickness of the sample, respectively. Typically, C was 3 nF and D 100 nm. The capacitance was calculated for each sample from the ratio of the displacement current in the sample under an applied bias. The detailed derivation is found in Chapter 2, section 2.3.2 of this thesis.

The amplitude of the electric field decay $\Delta E/\Delta E_{max}$ at any time after pump pulsed excitation (time zero) can thus directly be related to a percentage of total number of extracted charges. The larger the negative amplitude, the more charges extracted. The signal should eventually reach -1, indicating all charges are extracted.

The excitation intensity in the following dynamics was adjusted to have the same number of absorbed photons for both excitation wavelengths, $<3.10^{11}$ photons/cm².

Prompt charge generation

We will first address the samples where pBTTT is intercalated with PCBM to form a co-crystal phase, leading to only prompt (<100 fs) electron and hole

transfer. This is the case for the 1:1 sample at both excitation wavelengths, and 1:4 sample at 540 nm excitation, as derived from transient absorption data in section 5.3.

In the 1:1 blend, identical electric field dynamics and amplitude for both excitation wavelengths are observed in Figure 5.14. As the microstructure in this sample is one-phase, charge drift is expected to be identical for both excitation wavelengths in this sample. This result emphasizes that excitation (photon) energy yields similar mobile charges. At 1 ns time delay, only about 10 % of the charges are extracted for both excitation wavelengths. This weak decay of the electric field dynamics indicates that most of the charge extraction occurs on slower timescales than our optical time delay of 1.2 ns, which is assigned to trapped electron-hole pairs at the pBTTT:PCBM interface. The voltage dependent electric field dynamics of this 1:1 blend, shown in Figure 5.15 a, clearly demonstrate the nature of prompt charge generation in a co-crystal phase: bound charge pairs (CT states) tend to dissociate more at higher voltages.[37]

For the 1:4 device which contains both co-crystal regions and pure PCBM clusters, the dynamics at 540 nm excitation are faster than the 1:1 device, attributed to higher electron mobility in the PCBM clusters (Figure 5.14).
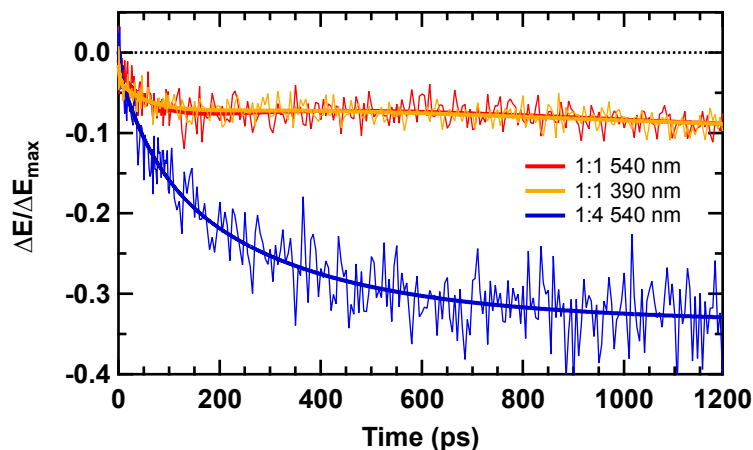

Figure 5.14 Electric field dynamics for different devices (100 nm) at 540 and 390 nm excitation wavelength. The dynamics were normalized for the maximum number of extracted charges (see equation 5.2). The externally applied electric field is 0.4MV/cm. Solid lines represent the result of the best multi-exponential fit.

Devižis et al. reported PCBM mobility up to 0.33 cm^2/V·s at similar field strength.[13] In APFO3:PCBM blends studied by Pranculis et al., the 1:4 device also showed fast electric field dynamics assigned to electron mobility in enhanced percolation pathways.[44] PCBM clusters allow for 35% charge extraction within 1.2 ns in the 1:4 device.

The electric field dynamics are less dependent on externally applied electric field in the 1:4 sample compared to the 1:1 sample (Figure 5.15). As previously mentioned, both charge pair dissociation and transport are affected by bias voltage. However, we have seen from TA measurements that geminate recombination is prevented in the 1:4 sample, and we can therefore assume that charge carriers formed in the 1:4 device are free or loosely bound. The slight voltage dependence on electric field dynamics in Figure 5.15 b is thus mostly assigned to transport, which is assigned to poor percolation of holes in pBTTT due to PCBM clusters. Although poor hole mobility could be detrimental to the
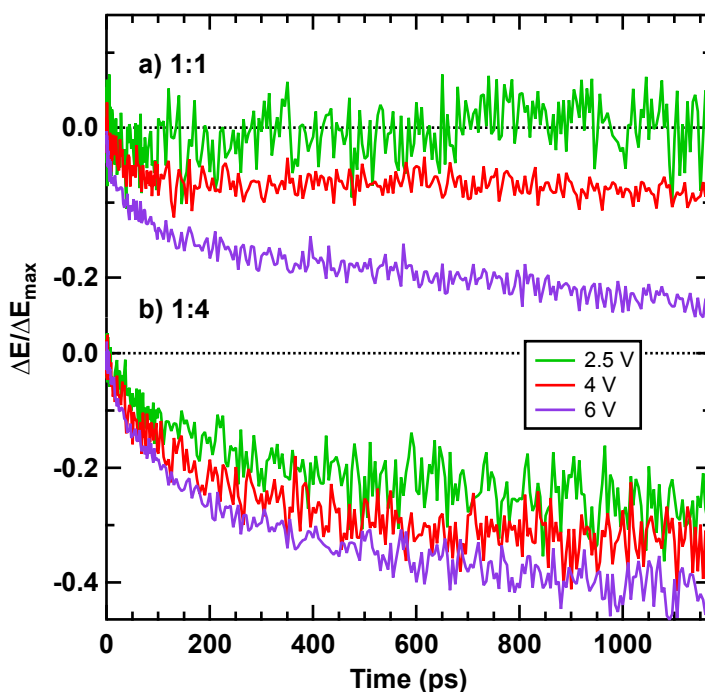

Figure 5.15 Electric field dynamics for a) 1:1 and b) 1:4, samples at 540 nm excitation wavelength. The dynamics were normalized for the maximum number of extracted charges (see equation 5.2). The externally applied electric field is varied from 0.25 to 0.6 MV/cm.

device, another work reported that high mobility of one of the two charge carriers is sufficient to efficiently dissociate charge pairs.[44] Moreover, it is now well known that fullerene domains may act as a driving force for charge separation in polymer:fullerene blends. [7,34,37]

Further insight into charge transport is derived from the average electron-hole distance l(t) calculated from the electric field dynamics. In fact, an increased distance between electron-hole pairs will decrease the externally applied electric field by the following relation:

$$l(t) = D \cdot \left(1 - \sqrt{1 - \frac{\Delta E(t)}{\Delta E_{max}}} \right) \tag{5.3}$$

where D is the sample thickness, and $\Delta E(t)/\Delta E_{max}$ is the electric field dynamics as a function of time as presented in Figure 5.14. The derivation is found in Chapter 2, section 2.3.2, as well as in references of this Chapter.[10,13,44] This equation takes charge extraction into account.

l(t) corresponds to the average distance in the direction of the field across the sample. Only prompt charge generation (thus where pBTTT is in the co-crystal
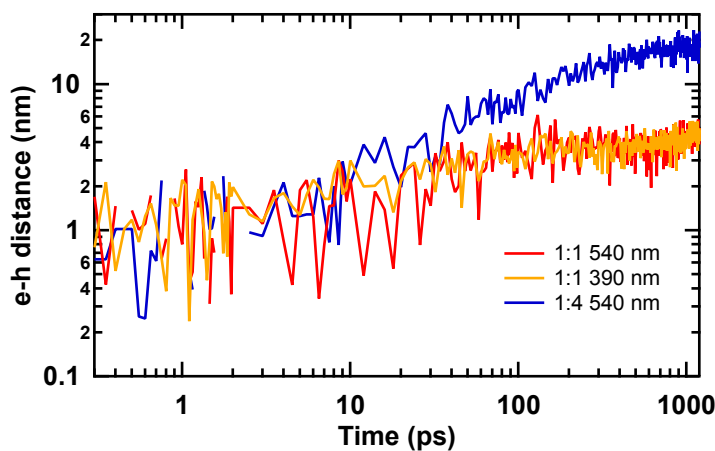

Figure 5.16 Time-dependent average electron-hole distance after prompt charge generation. The distance is an average on the applied electric field axis (0.4 MV/cm) across the device. Devices thickness are about 100 nm. The excitation wavelength is shown in the legend.

phase only) can be modeled, as delayed charge generation can not be accounted for. Therefore, only data for the 1:1 and 1:4 samples are considered, at both excitation wavelengths for the former, and only 540 nm excitation for the latter. Results are shown in Figure 5.16. The noise at early time delays is assigned to small perturbation of the electric field.[13] The small charge carrier displacement in the first ps after excitation is just above 1 nm for all samples, showing that the charge pairs in the co-crystal phase are rather close. Charge delocalization is prevented in the co-crystal phase of the 1:1 blend due to its geometry and absence of neat regions.[47] This result also rationalizes our electrostatic picture in TA data, where we assumed initial charge separation of about 1 nm. In TA, dissociation of bound charge pairs has to compete with gCR (about 211 ps for co-crystal) to effectively separate. The initial bound charge pairs are randomly distributed around the electric field axis, and we probe only the charge pairs along the axis of the electric field. The smaller electron-hole distance at 1 ns for the 1:1 blend of about 5 nm strongly corroborates that bound charge pairs are essentially formed in the pure co-crystal regions. PCBM clusters in the 1:4 sample efficiently separate the charges further to reach 15 nm at 1 ns after excitation. Results emphasize here the importance of fullerene clusters for charge separation in pBTTT:PCBM blends, in combination with prompt charge generation.

Time-dependent mobility can be obtained from the average electron-hole distance as follows:[44]

$$\mu(t) = \frac{1}{E} \cdot \frac{\partial l(t)}{\partial t} \qquad (5.4)$$

This mobility is averaged for electrons and holes, and is shown in Figure 5.17. For the 1:1 sample, the initial mobility is about 0.1 $cm^2/V \cdot s$ and decreases by about two orders of magnitude on 1 ns time delay, independent of excitation wavelengths. We can relate the decrease in initial mobility to the energetic charge relaxation due to disorder. This has been observed in other
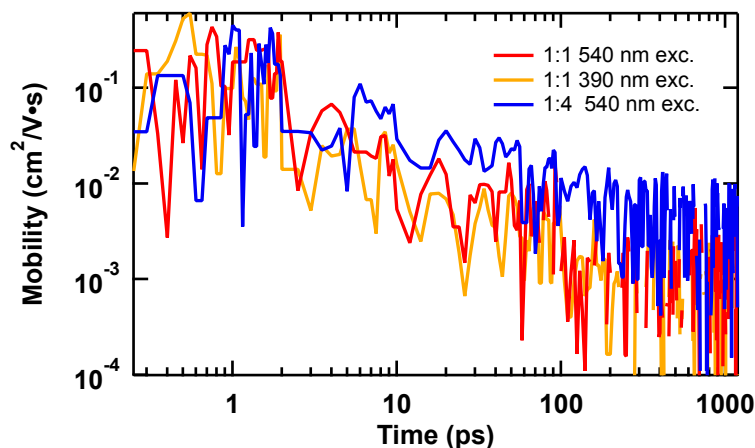
Figure 5.17 Time-dependent charge carrier mobility averaged for electrons and holes from the experimental data of Figure 5.15 at 0.4MV/cm applied electric field.

polymer:fullerene systems.[10,13] Buchaca et al. reported a hole mobility in the 1:1 blend of about 0.015 $cm^2/V \cdot s$. This is similar to the value obtained at long time delays in Figure 5.17, indicating that time-resolved EA measurements probes mobility of charges before they reach equilibrium.

The 1:4 sample has similar initial mobility to the 1:1 sample. This can be understood as follows: electron mobility in pure PCBM devices, or very large PCBM domains is rather high, up to but 0.33 $cm^2/V \cdot s$ for an applied electric field of 0.7 MV/cm.[13] In pBTTT:PCBM blends, holes also migrate toward the electrode, however the mobility is presumably lower than for electrons in PCBM, especially in the co-crystal phase. Indeed, holes in the co-crystal phase migrate along the chains, as transport along the π-stacks is prevented by fullerene intercalation. Therefore, the average carrier mobility is globally lower than for electrons in pure PCBM domains. The 1:4 device however shows less decrease in mobility than the 1:1 device. This is assigned to percolation pathways for electrons in PCBM clusters that are not found in the 1:1 blend.

Multiphasic charge generation

Additive samples excited at 540 nm display multiphasic (prompt and delayed) charge generation in TA data. Concerning the Me7 sample, the electric field
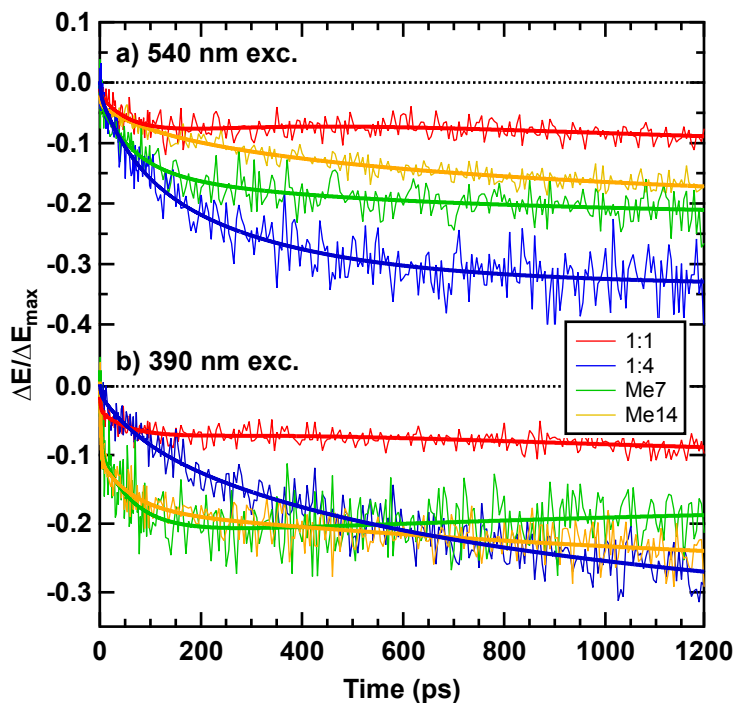
Figure 5.18 Electric field dynamics for different devices (100 nm) at 540 and 390 nm excitation wavelength. The dynamics were normalized for the maximum number of extracted charges (see equation 5.2). The externally applied electric field is 0.4MV/cm. Solid lines represent the result of the best multi-exponential fit.

dynamics at 540 nm excitation are complex, reflecting the three-phase microstructure (Figure 5.18 a). The electric field dynamics are faster than for the 1:1 sample, indicating a better transport which we can safely assign to the neat domains. Indeed, as charge carrier generation is multiphasic in this sample, faster electric field dynamics than the 1:1 sample (where charge carrier generation is prompt) suggests the charge carriers migrate faster in Me7 sample. Similarly, the Me14 sample shows multiphasic electric field decay (Figure 5.18 a). Exciton diffusion in large neat pBTTT domains such as those found in Me14 slow down the electron transfer event. Therefore charge formation is slower, and charge migration takes place on slower timescales. This yields intermediate charge drift dynamics between Me7 and 1:1 sample.

Excited at 390 nm, the electric field dynamics in the 1:4 device are slower compared to 540 nm excitation, which is attributed to the exciton diffusion in the PCBM cluster and delayed charge generation, in agreement with TA

data (Figure 5.18 b). Photoinduced charge carrier generation in PCBM at 390 nm excitation has been observed under the presence of an external field.[48] If existing, this process is difficult to highlight, as holes in PCBM still may reach the pBTTT interface and further diffuse within pBTTT.

Electric field dynamics at 390 nm excitation for additive samples (Me7 and Me14) demonstrate a major electric field decay within 2 ps in Figure 5.18 b. At this time scale, this invokes prompt charge generation combined with high hole mobility in and/or to the neat domains. 390 nm excitation is more selective for the co-crystal phase, as derived from TA data. As the ultrafast decay with 2 ps time constant is much weaker in amplitude for the 1:1 blend (about 14%) compared to the additive samples (Me14: 38% and Me7: 47%), we conclude that prompt generation in the co-crystal phase and at the interface of pure domains (no exciton diffusion necessary) are followed by ultrafast hole migration to or in the neat domain within 2 ps. This confirms our findings from TA data where we saw ultrafast hole migration from intercalated to pure pBTTT domains within 1 ps.

The dynamics in Me14 after 500 ps show a second decay time component which is not present in the dynamics of the Me7 sample (Figure 5.18 b). As fullerene domains are larger in Me14 compared to Me7, we can assign this to delayed charge generation following exciton diffusion in fullerene domains. The electric field dynamics in Me7 reach a plateau at 2 ps time delay, and no further dynamics are observed in this sample. We can relate this to the fact that Me7 contains smaller pure fullerene domains compared to Me14, and is therefore more affected by traps at grain boundaries.[16]

Charge transport in pBTTT under steady-state conditions has been studied extensively in field-effect transistors.[49,50] Findings are that the mictrostructure plays an important role, and our results point out that early timescales are crucial for efficient charge collection efficiency. This early timescale behavior is even more important as organic photovoltaic devices are much thinner than field-effect transistors. Limits in the microstructure are grain boundaries, combined

with small neat domain sizes as they act like traps.[51] Hole transport along the π-stacking (interchain) and polymer backbone (intrachain) are equally present in pBTTT.[52] Probably these two transport modes are responsible for different timescales of electric field decay, they are, however, difficult to distinguish. Domain sizes in such pBTTT solid-state films are about 20-30 nm, and disorder in the π-stacking direction is about 7 nm.[50] We therefore speculate that promptly generated holes in the co-crystal phase or at the interface of neat pBTTT domains migrate about several nm in the pure domains before reaching a grain boundary, and they do so within 2 ps. We can therefore set a lower limit of about 7 nm distance achieved within 2 ps. Over the same timescale, the charge pairs in the 1:1 sample are still tightly bound and do not separate further than 1 nm as derived from Figure 5.16. We here have a clear confirmation that charge separation is favored with the presence of neat pBTTT domains in 1:1 blends processed with additives, and this is already observed at 2 ps after photoexcitation.

5.5. Conclusions

In this chapter, we have investigated the ultrafast dynamics of pBTTT:PCBM blends. Fatty acid methyl ester additives were used to accurately control the microstructure from fully intercalated, partially intercalated to predominantly de-intercalated blends.

Results show that bound charge pairs are formed on ultrashort timescales (≈100 fs) in fully intercalated pBTTT:PCBM domains, resulting equally from electron and hole transfer. This is confirmed by field dependent charge dynamics. Dissociation of bound charge pairs in the intermixed phase involves applied electric fields and/or an energy cascade for the electron to PCBM clusters, which efficiently compete with geminate charge recombination. PCBM

clusters in the 1:4 blend are also responsible for delayed charge generation during selective PCBM excitation.

The interface of neat domains in two and three phase systems such as Me7 and Me14 samples show prompt as well as delayed charge generation, depending on the exciton generation site. The short pBTTT exciton lifetime ($\approx$150 ps) limits electron injection efficiency due to large neat pBTTT domain sizes. Geminate charge recombination is nevertheless reduced in these blends containing neat pBTTT domains (Me7 and Me14), increasing the charge yield of these samples compared to the 1:1 blend at 1 ns timedelay.

Pure fullerene and polymer domains are responsible for faster charge migration than in the co-crystal phase. In the 1:4 sample, the electrons in PCBM clusters are likely responsible for the faster electric field decay. Pure polymer domains actually attract holes from the co-crystal phase, without help of externally applied electric field. This is most likely due to an energy cascade driving the hole from the co-crystal to the neat domains. This is confirmed by ultrafast electric field dynamics, and we estimate that electron-hole pairs are separated by about 7 nm within 2 ps thanks to neat pBTTT domains. Results emphasize the need for interconnected pure pBTTT domains for hole transport, or larger neat domains. On the same timescale in the 1:1 blend, the average electron-hole distance is about 1 nm, indicating poor percolation pathways for both electrons and holes.

The use of additives enables to increase the amount of polymer in pBTTT:PCBM blends. This is of paramount interest, as 1:4 devices typically present better photovoltaic performance than lower containing fullerene blends. By using additives during film processing, the polymer to fullerene ratio could be increased and directly increase light harvesting. Indeed, fullerenes, despite their excellent electron mobility, are still poor light harvesters compared to conjugated polymers. Highly efficient blends have thus to be designed for the light absorption too, which implies either fullerene derivatives like C_{70} or newly developing polymers.[53]

Results presented in this chapter also demonstrate that transient absorption and Stark shift spectroscopies are valuable tools to shed light into the charge generation and transport mechanism of polymer:fullerene blends. They are both complementary and relate directly to the microstructure found in pBTTT:PCBM blends.

5.6. Methods

Sample preparation

The pBTTT polymer (Mn = 34 kDa; Mw = 66 kDa) was synthesized as previously reported, while PCBM was purchased from Solenne and used without further purification.[19] Solutions were prepared by mixing pBTTT and PCBM (blends by mass) in 1,2-ortho- dichlorobenzene (1,2-oDCB, Aldrich) for a concentration of 20mg/mL. The additives (Me7, Me12 and Me14) were purchased from Aldrich and Fluka and added in 1 and 10 molar equivalents of the respective additive per monomer unit of the pBTTT polymer. All solutions were stirred for more than 4 hours at 100 °C to fully dissolve the active material. The hot (85-90°C) blend solutions were then deposited on glass (for TA and fluorescence up-converison) or patterned ITO (for transient Stark shift measurements) by wire-bar coating. The substrates were kept at 35°C for the formation of the co-crystal. The film thickness was about 100 nm. Aluminium counter-electrodes were evaporated on top of the active layer on ITO substrates. Oxygen was carefully removed by pumping the samples in vacuum for 24h. TA measurements were done in an argon home-made chamber. Otherwise, the samples were sealed with an epoxy resin (glovebox) for transient Stark shift and fluorescence up-conversion measurements.

Fluorescence Up-Conversion Spectroscopy

The setup for fluorescence up-conversion spectroscopy from Group Vauthey is described elsewhere.[54] Briefly, it is based on a modified FOG100 system (CDP

Lasers & Scanning Systems), except that a Mai Tai HP (Spectra-Physics) mode-locked Ti:sapphire laser system was used to have a tunable excitation wavelength. The 1000 nm output (100 fs pulse duration, 80 MHz repetition rate) was frequency doubled for sample excitation at 500 nm. The pump intensity per pulse was about 4 mW, yielding a fluence of 3 $\mu J/cm^2$ (with a spot diameter of 50 μm). No significant intensity effects were observed, nor degradation. The sample was rotated during the measurement to avoid degradation, and three time scans were averaged. The fluorescence was enhanced by sum-frequency generation with a delayed gate pulse in a non-linear BBO crystal. The up-converted signal was then dispersed in a monochromator and its intensity measured with a photomultiplier tube operating in the photon counting mode. The polarization of the pump beam was at magic angle relative to that of the gate pulses. The dynamics were reproduced with a Gaussian instrument response function (about 100 fs) with a sum of exponential terms.

Transient absorption spectroscopy

Transient absorption spectra were recorded via femtosecond pump-probe spectroscopy based on the 778 nm output of an amplified Ti-sapphire laser (Clark-MXR, CPA-2001) with 150 fs pulses running at 1 kHz repetition rate. The pump beam was generated via a two-stage non-collinear optical parametric amplifier (NOPA), while the probe beam was a white light continuum (350-750 and 790-1020 nm) generated by a portion of the 778 nm passing through a continuously moving CaF_2 plate. The pump wavelength was set at 540 nm from the NOPA output, or 390 nm generated by SHG of the fundamental 778 nm beam passing through a BIBO. Visible and nIR probe wavelengths were recorded in two different experiments, by changing the blaze grating from 500 to 800 nm and adapting the band pass filters accordingly. The probe beam was split before the sample into a signal and reference beam in order to account for intensity fluctuations. Both beams were recorded shot by shot with a pair of 163 mm spectrographs (Princeton instruments, SpectraPro 2500i) equipped with a

512 x 58 pixels back-thinned CCD (Hamamatsu S07030-0906) and assembled by Entwicklungsbüro Stresing, Berlin. Excitation fluence was adapted to have the same number of photons for both excitation wavelengths, typically $<1.7\times10^{13}$ photons/cm^2.

All spectra were corrected for the white-light chirp measured by Kerr gating and background noise. Global analysis by a multiexponential fit at different wavelengths (typically every 5 nm) enabled the dissociation of the various photophysical processes occurring. The associated spectra show the amplitude of the transient signal related to each time component.

Time-resolved electroabsorption spectroscopy

The EDA and EA spectra were measured in reflectance mode on full solar cell devices with a comparable setup as described for the TA experiments, with the probe beam passing through the ITO, the active layer and then being reflected off the aluminium electrode. The white light probe (400-700 nm) was generated in a 3 mm sapphire disc from the 778 nm output of an amplified femtosecond laser (the same as described in the TA section). The probe beam was split before the sample into a signal beam (focused on the sample and reflected off the silver electrode into the detector) and a reference beam reaching a second detector. The signal and reference were detected with a pair of 163 mm spectrographs (Andor Technology, SR163) equipped with a 512×58 pixels back-thinned CCD (Hamamatsu S07030-0906) and assembled by Entwicklungsbüro Stresing, Berlin. The pump excitation intensities at 390 and 540 nm were adjusted to have the same number of absorbed photons for both excitation wavelengths, $<3.10^{11}$ photons/cm^2.

The electric field was modulated with a function generator (Tektronix AFG 2021). A square voltage pulse in reverse bias voltage (100 μs duration) was applied at half the probe frequency of 1 kHz, and the reflected probe light was measured shot-by-shot in the presence and in the absence of electric field,

averaged over 3000 shots. At least three time scans were averaged. The photocurrent was measured with an oscilloscope through a 50 Ω load.

5.7. References

(1) Green, M. A.; Emery, K.; Hishikawa, Y.; Warta, W.; Dunlop, E. D. *Prog. Photovolt: Res. Appl.* **2014**, *22*, 701–710.

(2) Mazzio, K. A.; Luscombe, C. K. *Chem Soc Rev* **2015**, *44*, 78–90.

(3) Gao, F.; Inganäs, O. *Phys. Chem. Chem. Phys.* **2014**, *16*.

(4) Huang, Y.; Kramer, E. J.; Heeger, A. J.; Bazan, G. C. *Chem. Rev.* **2014**, *114*, 7006–7043.

(5) Grancini, G.; Maiuri, M.; Fazzi, D.; Petrozza, A.; Egelhaaf, H.-J.; Brida, D.; Cerullo, G.; Lanzani, G. *Nat Mater* **2013**, *12*, 29–33.

(6) Gélinas, S.; Rao, A.; Kumar, A.; Smith, S. L.; Chin, A. W.; Clark, J.; van der Poll, T. S.; Bazan, G. C.; Friend, R. H. *Science* **2014**, *343*, 512–516.

(7) Burke, T. M.; McGehee, M. D. *Adv. Mater. Weinheim* **2014**, *26*, 1923–1928.

(8) Provencher, F.; Bérubé, N.; Parker, A. W.; Greetham, G. M.; Towrie, M.; Hellmann, C.; Côté, M.; Stingelin, N.; Silva, C.; Hayes, S. C. *Nat Comms* **2014**, *5*, 4288.

(9) Bakulin, A. A.; Rao, A.; Pavelyev, V. G.; van Loosdrecht, P. H. M.; Pshenichnikov, M. S.; Niedzialek, D.; Cornil, J.; Beljonne, D.; Friend, R. H. *Science* **2012**, *335*, 1340–1344.

(10) Amarasinghe Vithanage, D.; Devižis, A.; Abramavičius, V.; Infahsaeng, Y.; Abramavičius, D.; MacKenzie, R. C. I.; Keivanidis, P. E.; Yartsev, A.; Hertel, D.; Nelson, J.; Sundström, V.; Gulbinas, V. *Nat Comms* **2013**, *4*, 2334.

(11) Vandewal, K.; Albrecht, S.; Hoke, E. T.; Graham, K. R.; Widmer, J.; Douglas, J. D.; Schubert, M.; Mateker, W. R.; Bloking, J. T.; Burkhard, G. F.; Sellinger, A.; Fréchet, J. M. J.; Amassian, A.; Riede, M. K.; McGehee, M. D.; Neher, D.; Salleo, A. *Nat Mater* **2014**, *13*, 63–68.

(12) Devižis, A.; Serbenta, A.; Meerholz, K.; Hertel, D.; Gulbinas, V. *Phys. Rev. Lett.* **2009**, *103*, 027404.

(13) Devižis, A.; Hertel, D.; Meerholz, K.; Gulbinas, V.; Moser, J. E. *Organic Electronics* **2014**, *15*, 3729–3734.

(14) Hoppe, H.; Sariciftci, N. S. *J. Mater. Chem.* **2006**, *16*, 45–61.

(15) Zusan, A.; Gieseking, B.; Zerson, M.; Dyakonov, V. *Sci Rep* **2015**.

(16) Buchaca-Domingo, E.; Ferguson, A. J.; Jamieson, F. C.; McCarthy-Ward, T.; Shoaee, S.; Tumbleston, J. R.; Reid, O. G.; Yu, L.; Madec,

M. B.; Pfannmöller, M.; Hermerschmidt, F.; Schröder, R. R.; Watkins, S. E.; Kopidakis, N.; Portale, G.; Amassian, A.; Heeney, M.; Ade, H.; Rumbles, G.; Durrant, J. R.; Stingelin, N. *Materials Horizons* **2014**, *1*, 270–279.

(17)   Baklar, M.; Wöbkenberg, P. H.; Sparrowe, D.; Gonçalves, M.; McCulloch, I.; Heeney, M.; Anthopoulos, T.; Stingelin, N. *J. Mater. Chem.* **2010**, *20*, 1927.

(18)   Hamadani, B. H.; Gundlach, D. J.; McCulloch, I.; Heeney, M. *Applied Physics Letters* **2007**, *91*, 243512.

(19)   McCulloch, I.; Heeney, M.; Bailey, C.; Genevicius, K.; MacDonald, I.; Shkunov, M.; Sparrowe, D.; Tierney, S.; Wagner, R.; Zhang, W.; Chabinyc, M. L.; Kline, R. J.; McGehee, M. D.; Toney, M. F. *Nat Mater* **2006**, *5*, 328–333.

(20)   Scarongella, M.; Paraecattil, A. A.; Buchaca-Domingo, E.; Douglas, J. D.; Beaupré, S.; McCarthy-Ward, T.; Heeney, M.; Moser, J. E.; Leclerc, M.; Fréchet, J. M. J.; Stingelin, N.; Banerji, N. **2014**, *2*, 6218.

(21)   Mayer, A. C.; Toney, M. F.; Scully, S. R.; Rivnay, J.; Brabec, C. J.; Scharber, M.; Koppe, M.; Heeney, M.; McCulloch, I.; McGehee, M. D. *Adv. Funct. Mater.* **2009**, *19*, 1173–1179.

(22)   Miller, N. C.; Sweetnam, S.; Hoke, E. T.; Gysel, R.; Miller, C. E.; Bartelt, J. A.; Xie, X.; Toney, M. F.; McGehee, M. D. *Nano Lett.* **2012**, *12*, 1566–1570.

(23)   Guilbert, A. A. Y.; Schmidt, M.; Bruno, A.; Yao, J.; King, S.; Tuladhar, S. M.; Kirchartz, T.; Alonso, M. I.; Goñi, A. R.; Stingelin, N.; Haque, S. A.; Campoy-Quiles, M.; Nelson, J. *Adv. Funct. Mater.* **2014**, *24*, 6972–6980.

(24)   Scarongella, M.; De Jonghe-Risse, J.; Buchaca-Domingo, E.; Causa, M.; Fei, Z.; Heeney, M.; Moser, J.-E.; Stingelin, N.; Banerji, N. *J. Am. Chem. Soc* **2015**, *137*, 2908–2918.

(25)   Reid, O. G.; Pensack, R. D.; Song, Y.; Scholes, G. D.; Rumbles, G. *Chem. Mater.* **2014**, *26*, 561–575.

(26)   Lee, M. J.; Chen, Z.; Pietro, R. D.; Heeney, M.; Sirringhaus, H. *Chem. Mater.* **2013**, *25*, 2075–2082.

(27)   Dou, F.; Buchaca-Domingo, E.; Sakowicz, M.; Zhang, X.; Stingelin, N.; Silva, C. Banerji, N.; Silva, C., Eds.; SPIE, 2013; Vol. 8811, p. 88111J.

(28)   Sebastian, L.; Weiser, G.; Bässler, H. *Chemical Physics* **1981**, *61*, 125–135.

(29)   Chekalin, S. V.; Yartsev, A. P.; Sundström, V. *J. Exp. Theor. Phys.* **2001**, *93*, 706–716.

(30)   Chekalin, S. V.; Yartsev, A. P.; Sundström, V. *Quantum Electron.* **2007**, *31*, 395–397.

(31)   Cabanillas-Gonzalez, J.; Grancini, G.; Lanzani, G. *Adv. Mater.* **2011**, *23*, 5468–5485.

(32)   Drori, T.; Sheng, C.-X.; Ndobe, A.; Singh, S.; Holt, J.; Vardeny, Z. V. *Phys. Rev. Lett.* **2008**, *101*, 037401.

(33) Dick, D.; Wei, X.; Jeglinski, S.; Benner, R.; Vardeny, Z.; Moses, D.; Srdanov, V.; Wudl, F. *Phys. Rev. Lett.* **1994**, *73*, 2760–2763.

(34) Jamieson, F. C.; Domingo, E. B.; McCarthy-Ward, T.; Heeney, M.; Stingelin, N.; Durrant, J. R. *Chem. Sci.* **2012**, *3*, 485–492.

(35) Sauve, G.; Dimitrijevic, N. M.; Kamat, P. V. *The Journal of Physical Chemistry* **1995**, *99*, 1199–1203.

(36) Hedley, G. J.; Ward, A. J.; Alekseev, A.; Howells, C. T.; Martins, E. R.; Serrano, L. A.; Cooke, G.; Ruseckas, A.; Samuel, I. D. W. *Nat Comms* **2013**, *4*, 2867.

(37) Zusan, A.; Vandewal, K.; Allendorf, B.; Hansen, N. H.; Pflaum, J.; Salleo, A.; Dyakonov, V.; Deibel, C. *Adv. Energy Mater.* **2014**, *4*.

(38) Cabanillas-Gonzalez, J.; Virgili, T.; Gambetta, A.; L Lüer; Lanzani, G.; Anthopoulos, T.; de Leeuw, D. *Phys. Rev. B* **2007**, *75*, 045207.

(39) Cappel, U. B.; Feldt, S. M.; Schöneboom, J.; Hagfeldt, A.; Boschloo, G. *J. Am. Chem. Soc* **2010**, *132*, 9096–9101.

(40) Ardo, S.; Sun, Y.; Staniszewski, A.; Castellano, F. N.; Meyer, G. J. *J. Am. Chem. Soc* **2010**, *132*, 6696–6709.

(41) Miller, N. C.; Cho, E.; Junk, M. J. N.; Gysel, R.; Risko, C.; Kim, D.; Sweetnam, S.; Miller, C. E.; Richter, L. J.; Kline, R. J.; Heeney, M.; McCulloch, I.; Amassian, A.; Acevedo-Feliz, D.; Knox, C.; Hansen, M. R.; Dudenko, D.; Chmelka, B. F.; Toney, M. F.; Brédas, J.-L.; McGehee, M. D. *Adv. Mater.* **2012**, *24*, 6071–6079.

(42) Kniepert, J.; Schubert, M.; Blakesley, J. C.; Neher, D. *J. Phys. Chem. Lett.* **2011**, *2*, 700–705.

(43) Devižis, A.; Meerholz, K.; Hertel, D.; Gulbinas, V. *Phys. Rev. B* **2010**, *82*, 155204.

(44) Pranculis, V.; Infahsaeng, Y.; Tang, Z.; Devižis, A.; Vithanage, D. A.; Ponseca, C. S.; Inganäs, O.; Yartsev, A. P.; Gulbinas, V.; Sundström, V. *J. Am. Chem. Soc* **2014**, *136*, 11331–11338.

(45) Cates, N. C.; Gysel, R.; Beiley, Z.; Miller, C. E.; Toney, M. F.; Heeney, M.; McCulloch, I.; McGehee, M. D. *Nano Lett.* **2009**, *9*, 4153–4157.

(46) Scheblykin, I. G.; Yartsev, A.; Pullerits, T.; Gulbinas, V.; Sundström, V. *J Phys Chem B* **2007**, *111*, 6303–6321.

(47) Dou, F.; Buchaca-Domingo, E.; Sakowicz, M. *Journal of Materials Chemistry C* **2015**.

(48) Burkhard, G. F.; Hoke, E. T.; Beiley, Z. M.; McGehee, M. D. *J. Phys. Chem. C* **2012**, *116*, 26674–26678.

(49) Poelking, C.; Cho, E.; Malafeev, A.; Ivanov, V.; Kremer, K.; Risko, C.; Brédas, J.-L.; Andrienko, D. *J. Phys. Chem. C* **2013**, *117*, 1633–1640.

(50) Gasperini, A.; Sivula, K. *Macromolecules* **2013**, *46*, 9349–9358.

(51) Noriega, R.; Rivnay, J.; Vandewal, K.; Koch, F. P. V.; Stingelin, N.; Smith, P.; Toney, M. F.; Salleo, A. *Nat Mater* **2013**, *12*, 1038–1044.

(52) Gasperini, A.; Bivaud, S.; Sivula, K. *Chem. Sci.* **2014**, *5*, 4922–4927.

(53) Shivanna, R.; Shoaee, S.; Dimitrov, S.; Kandappa, S. K.; Rajaram, S.;

Durrant, J. R.; Narayan, K. S. *Energy Environ. Sci.* **2013**, *7*, 435.

(54)   Morandeira, A.; Engeli, L.; Vauthey, E. *J. Phys. Chem. A* **2002**, *106*, 4833–4837.

Chapter 6

Concluding remarks and outlook

"The struggle for existence is the struggle for available energy."

Ludwig Boltzmann

In this work, we used time-resolved pump-probe techniques to shed light into the charge formation, separation and transport on the nanoscale of organic photovoltaic (OPV) systems. Donor-acceptor mixtures investigated are based on cyanine small molecule or polymer pBTTT as donors combined with fullerene acceptor (C_{60} or PCBM). By studying the neat materials and different model systems, from small-molecule bilayers to polymer:fullerene blends, we can derive a picture of the various photoinduced processes leading to charge collection at the electrodes. Transient absorption spectroscopy gave valuable insight into rate and yield of charge injection after photoexcitation of the donor and/or acceptor material. Time-resolved electroabsorption spectroscopy revealed charge carrier drift dynamics. In all investigated systems, ultrafast electron transfer into fullerene acceptor following donor excitation is completed in less than 100 fs. Results in this work nevertheless emphasize that a driving force is needed for separation of the resulting charge pairs to compete with geminate recombination:

- An externally applied electric field can act as this driving force. This is evidenced in cyanine (Cy3-P)/C_{60} planar heterojunctions (bilayers), where interfacial charge transfer (CT) states are created from Cy3-P electron transfer via hot excited states. The CT states dissociate only in the presence of an applied electric field and this takes place on timescales of tens to hundreds of picoseconds. We suggest that relaxed CT states are precursors for free charge carriers, even if electron transfer originates from the hot Cy3-P excited state. Subsequent electron drift in C_{60} takes place on several ps, whereas holes in Cy3-P do not drift on the nanosecond timescale. Without the application of an electric field, the interfacial charge transfer state does not dissociate and therefore recombines.

- The presence of PCBM clusters is another possible driving force, which efficiently drives the electron away from the interface via an energy cascade stabilizing the electron. This is more evident in polymer pBTTT:PCBM (1:4) blends than for cyanine Cy3-B:PCBM blends, as for

the latter charge recombination is still fast (ps) while the former shows delayed charge recombination (> 1 ns). We attribute this to the special case of Cy3-B where the borate counter-anion can reduce the oxidized Cy3. Electron delocalization in C_{60} solid-state films was observed by monitoring photoinduced Stark shifts within transient absorption spectroscopy data. The result of the photoexcitation of C_{60} is an instantaneous (<300 fs) delocalized, i.e. intermolecular, charge transfer state, which localizes back on one molecule within 360 fs. These timescales are in accordance with electron delocalization found in PCBM clusters driving charge separation within 40 fs in polymer:fullerene blends.[1]

- Finally, we have shown that neat pBTTT domains in pBTTT:PCBM blends attract holes from the co-crystal (fully intermixed) phase, and time-resolved electroabsorption measurements revealed hole migration of about 7 nm in 2 ps. Without external field, the holes migrate from the co-crystal phase to the neat domains within 1 ps. Therefore, we suggest that the driving force for dissociation of charge pairs in partially de-intercalated pBTTT:PCBM blends is an energy cascade for holes from fully intermixed to neat domains. Neat pBTTT domains size however has to be controlled to avoid exciton loss due to its short lifetime.

We have gained much insight of the charge separation processes, however we lack understanding on a few aspects in these model systems. Therefore, we suggest several experiments that one could carry out:

- Time-resolved emission measurements such as broadband fluorescence up-conversion would provide insight into ultrafast electron transfer processes. With this method, we could scrutinize excited state relaxation and losses prior to electron transfer. In Cy3-P/C_{60} bilayers, about 70% of Cy3-P excited states are quenched within 130 fs after excitation due to interfacial contact with C_{60}. Knowing that typical Cy3-P layer thickness

of 45 nm is larger than the expected exciton diffusion length of about 10 nm, this gives rise to a fundamental question: how fast is exciton diffusion?

- To gain more insight in the charge dissociation when the charge pair is bound at the interface, such as in Cy3-P/C_{60} bilayers, one could perform pump-push-probe experiments.[2] Bakulin et al. demonstrated that hot excitations either create delocalized charge transfer states that efficiently dissociate into free charge carriers within hundreds of fs; or they relax to the lowest interfacial charge transfer state. An IR push pulse with controlled time-delay re-excites the relaxed CT states to energetically higher states, giving a second opportunity for charge delocalization and thus, separation. Although this process has minor impact in efficient OPVs, poor photovoltaic systems where excess energy is lost to a relaxed charge transfer state showed an increase in photocurrent. The all-optical pump-push-probe was also performed and indicated a short lifetime of hot CT states. Probing in the THz range would allow for optical and therefore contactless observation of mobile charge carriers.

- Bias-dependent charge separation is observed when interfacial charge transfer states are populated, instead of dissociation into free charge carriers. Measuring transient absorption with a constant applied bias would provide insight into device operating conditions of photovoltaic devices.

- One should systematically study both planar and bulk heterojunction blends of the same materials to understand the photoinduced reactions, if material intermixing is possible. Planar heterojunctions as well as controlled microstructure obtained in pBTTT:PCBM blends processed with additives are both model systems that allow for investigating photoinduced charge separation processes. Also, varying the donor:acceptor ratio such as done in Cy3-B:PCBM blends has proven beneficial for studying kinetic competition between intra ion-pair (Cy3-B)

reductive quenching and Cy3 oxidation in the presence of PCBM. Last, investigating in more details hole transfer from fullerene to the donor material would allow for a complete picture of charge generation in OPV systems.

- This work highlights that high temporal resolution is a key parameter for investigating donor-acceptor charge formation and separation in organic systems. Amongst that, the addition of spatial resolution in time-resolved measurements would be beneficial in complex systems such as bulk heterojunctions, where the degree of disorder is large due to morphology and molecular structure of donor and acceptor. Similarly to what has been done on InAs nanowires,[3] we propose to scan across a device with an AFM probe with nanometer resolution, and perform local pump-probe experiments using tip-enhanced signals on femtosecond timescales. This would take time-resolved experiments in OPV systems to a whole new level.

We finally suggest that ideal photovoltaic blend devices should be made by a gradient of donor:acceptor (D:A) ratio. A finely intermixed D:A phase should be sandwiched between pure donor and acceptor layers. Such a structure would be feasible by vapor deposition, allowing for precise control of small molecules and oligomers mixing and deposition. The gradient would prevent trapping of charge carriers at grain boundaries, and concomitantly increase the light harvesting. Indeed, most efficient OPV devices rely on intermixing with high amounts of fullerene, typically a ratio of 1:4. We believe a gradient solar cell could reduce the cost of photon absorption losses within the device and improve the overall efficiency.

References

(1)   Gélinas, S.; Rao, A.; Kumar, A.; Smith, S. L.; Chin, A. W.; Clark, J.; van der Poll, T. S.; Bazan, G. C.; Friend, R. H. *Science* **2014**, *343*, 512–516.

(2)   Bakulin, A. A.; Rao, A.; Pavelyev, V. G.; van Loosdrecht, P. H. M.; Pshenichnikov, M. S.; Niedzialek, D.; Cornil, J.; Beljonne, D.; Friend, R. H. *Science* **2012**, *335*, 1340–1344.

(3)   Eisele, M.; Cocker, T. L.; Huber, M. A.; Plankl, M.; Viti, L.; Ercolani, D.; Sorba, L.; Vitiello, M. S.; Huber, R. *Nature Photon* **2014**, *8*, 841–845.

List of Abbreviations and constants

A	Absorbance
Ag	Silver
Al	Aluminium
c	Speed of light in vacuum (2.99×10^{-8} m/s)
C	Capacitance
Cy3	1,1'-diethyl-3,3,3',3'-tetramethylcarbocyanine
Cy3-B	Cyanine Cy3 with tetraphenylborate counter anion BPh_4^-
Cy3-C	Cyanine Cy3 with perchlorate counter-anion ClO_4^-
Cy3-P	Cyanine Cy3 with hexafluorophosphate counter-anion PF_6^-
CB	Chlorobenzene
C$_{60}$	Buckminsterfullerene (or bucky-ball), also called fullerene
CT	Charge transfer
D	Sample thickness
ΔA	Change in absorbance
e	Elementary charge ($1.602176565 \times 10^{-19}$ C)
E	Electric field
EA	Electroabsorption
EDA	Electromodulated differential absorption
ESA	Excited state absorption
GSB	Ground state bleaching
h	Planck constant ($6.62606957 \times 10^{-34}$ J·s)
IC	Internal Conversion
I$_{photo}$	Photocurrent
ISC	Intersystem Crossing
ITO	Indium tin oxide
IQE	Internal Quantum Efficiency

MeX	Fatty acid methyl ester additive with X carbon atoms, X between [7-14]
MoO$_3$	Molybdenum oxide
pBTTT	poly(2,5-bis(3-alkyl-thiophene-2-yl)thieno[3,2-b]thiophene, polymer
PCBM	[6,6]- phenyl C$_{61}$-butyric acid methyl ester, fullerene derivative
SE	Stimulated emission
T	Transmission
TA(S)	Transient absorption (spectroscopy)
V	Voltage bias
VR	Vibrational Relaxation
λ	Wavelength (nm)

Acknowledgments

This is my opportunity to acknowledge all the people who have helped me to achieve this work.

I shall start by thanking Prof. Jacques-E. Moser for giving me the opportunity to fulfill my PhD under his supervision. I dealt with multidisciplinary tasks, and he has let me manage my projects my own way. He looks for good science and clear results, and this has learnt me a lot. I felt he was confident, and I thank him for that.

I am deeply grateful to Andrius Devižis for his knowledge, his scientific spirit, and his kindness. Thanks to him, the electroabsorption setup was built in our laboratories and enabled new discoveries on cyanine bilayers.

I want to thank Prof. Natalie Banerji, who always was a great help for white light optimization and data analysis. Working with her also enabled me to tackle polymer-based photovoltaics, for which I am indebted.

A special thanks to Arianna Marchioro, best office mate, with whom it was always a pleasure to drink a cup of tea and share difficult as well as good times. Quotes such as her: "Quand je regardes mes fits, je me dis que c'est quand même un nuage de points"; and me: "Mes données, c'est comme des sables mouvants"; are among the long list of shared experiences. She is a very good mentor and cheer up.

Angela Punzi, for her patience during laser alignment training and perseverance: "you can do better" was her motto.

Jan Brauer, for his infinite time he could spend on discussing results, and helping out for laser alignment.

Joël Teuscher, for his optimism and knowledge which were of great value (and unfortunately late in my PhD time).

Jelissa DE JONGHE - RISSE

05.11.1987   French and Dutch (Native)

Belgian   English (Fluent)

Education

PhD candidate in Photonics   10.2010 – 04.2015

Group of Photochemical Dynamics, EPFL, Lausanne, Switzerland

Title: Ultrafast dynamics of photoinduced charge separation in cyanine- and polymer-based organic photovoltaic systems

Director: Prof. J.-E. Moser

Master of Science in Molecular & Biological Chemistry   2008 - 2010

EPFL, Lausanne, Switzerland

Bachelor of Science in Chemistry & Chemical Engineering   2005 - 2008

EPFL, Lausanne, Switzerland

Research Projects

Supervisor for 3 Master Projects   2011 - 2014

EPFL, Lausanne, Switzerland

Teaching assistant   2010 - 2014

EPFL, Lausanne, Switzerland

1st and 3rd year Bachelor students

Internship, Laboratory of Ultrafast Spectroscopy   2010 (6m)

Université de Montréal, Québec, Canada

Organic semiconductor processing and spectral characterization

Advisor: Prof. Carlos Silva

Master Project in Chemical Engineering, Erasmus scholarship   2009 - 2010

Delft University of Technology, The Netherlands

Bismuth vanadate for hydrogen production

Advisors: Prof. Michael Grätzel, EPFL and Prof. Roel van de Krol,

TUDelft

List of Publications

Ultrafast charge transfer in solid-state cyanine borate and blends with PCBM
J. De Jonghe-Risse, J. Heier, F. Nüesch, J.-E. Moser
Journal of Materials Chemistry A, 3, 10935-10941, 2015
DOI: 10.1039/c5ta00784d

A close look at charge generation in polymer:fullerene blends with microstructure control
M. Scarongella, J. De Jonghe-Risse, E. Buchaca-Domingo, Martina Causa', Z. Fei, M. Heeney, J.-E. Moser, N. Stingelin, N. Banerji
Journal of the American Chemical Society, 137, 2908−2918, 2015
DOI: 10.1021/ja510032x

Dissociation of charge transfer states and carriers separation in bilayer organic solar cells – A time-resolved electroabsorption spectroscopy study
A. Devižis, J. De Jonghe-Risse, R. Hany, F. Nüesch, S. Jenatsch, V. Gulbinas, J.-E. Moser
Submitted to Journal of the American Chemical Society, 2015

Photoconductivity and doping of PCBM in thin films by organoborates of cyanine dyes
J. De Jonghe, A. Sienkiewicz, F. Nüesch, J.-E. Moser, J. Heier
Manuscript in preparation

Transparent Organic Photodetector using a Near-Infrared Absorbing Cyanine Dye
H. Zhang, S. Jenatsch, J. De Jonghe, F. Nüesch, R. Steim, A.-C. Véron, R. Hany
Scientific Reports, 5, 9439, 2015
DOI: 10.1038/srep09439

Chaotropic agents boosting the performance of photo-ionic cells
R. Bourdon, P. Peljo, M. Méndez, A. Olaya, J. De Jonghe-Risse, H. Vrubel, H. Girault
Journal of Physical Chemistry C, 119, 4728−4735, 2015
DOI: 10.1021/acs.jpcc.5b00334

Dynamics and mechanisms of interfacial photoinduced electron transfer processes of third generation photovoltaics and photocatalysis
C. Bauer, J. Teuscher, J. C. Brauer, A. Punzi, A. Marchioro, E. Ghadiri, J. de Jonghe, M. Wielopolski, N. Banerji, J.-E. Moser
Chimia, 65, 9, 704-709, 2011
DOI: 10.2533/chimia.2011.704

Photoinduced interfacial electron transfer and lateral charge transport in molecular donor–acceptor photovoltaic systems
A. Punzi, J. C. Brauer, A. Marchioro, E. Ghadiri and J. De Jonghe, J.-E. Moser
Chimia, 65, 5, 353-355, 2011
DOI: 10.2533/chimia.2011.353

Persistent polarization memory in sexithiophene nanostructures
B. Gosselin, V. Cardin, A. Favron, J. De Jonghe, L.-I. Dion-Bertrand, C. Silva, R. Leonelli
Physical Review B, 83, 041201, 2011
DOI: 10.1103/PhysRevB.83.041201

Conferences and workshops

Oral presentations
- Swiss Chemical Society, Zürich, Switzerland, September 2014
  Charge-transfer dissociation at organic donor-acceptor interfaces probed with time-resolved electroabsorption
- Centre Suisse d'Electronique et de Microtechnique (CSEM), Neuchâtel, Switzerland, April 2013
  Photophysics of cyanine based organic solar cells

Poster presentations
- HOPV NanoGE, Spain 2011, Sweden 2012
- Swiss Chemical Society annual meetings, Switzerland, 2010-2014
- Swiss Physical Society, Switzerland, 2012
- EPFL Photonics day, Switzerland, 2010-2014
- NCCR MUST annual meetings, Switzerland, 2011-2013

Summerschool
- Organic and Dye Based Photovoltaics, Jyvaskyla, Finland, 2011

Member of the Swiss Chemical Society